PREPARATION AND CHARACTERIZATION OF BARIUM HEXAFERRITE ($BaFe_{12}O_{19}$) THICK FILMS FOR MICRO/ MILLIMETER WAVE DEVICE APPLICATION

A THESIS

Submitted to

THAPAR UNIVERSITY, PATIALA

For the award of

DOCTOR OF PHILOSOPHY

Submitted by

SAMIKSHA KUMARI

Under the supervision of

Dr. Puneet Sharma
Associate Professor

Dr. O. P. Pandey
Senior Professor & Dean (R&SP)

School of Physics and Materials Science
Thapar University, Patiala-147004
PUNJAB, INDIA

JULY 2015

DEDICATION

This thesis is dedicated to my entire loving and supportive family

My parents whose constant encouragement has helped me to reach all goals

My husband whose guidance keeps me moving forward in a positive direction

&

My little daughter for her sweet smile at every moment

CERTIFICATE

This is to certify that thesis entitled **"Preparation and Characterization of Barium Hexaferrite ($BaFe_{12}O_{19}$) Thick Films for micro/Millimeter Wave Devices Application "** which is being submitted by **Samiksha Kumari** for the award of the degree of Doctor of Philosophy in the School of Physics and Materials Science, Thapar University, Patiala (Punjab), is an authentic record of candidate's own research work under our supervision and guidance.

To the best of my knowledge, the matter presented inside the thesis in part or in full has not been submitted to any other university or institute for the award of any degree.

Puneet

Dr. Puneet Sharma
Associate Professor
School of Physics and Materials Science
Thapar University
Patiala – 147004 (INDIA)

Dr. O. P. Pandey
Senior Professor &
Dean, Research and sponsored projects
School of Physics and Materials Science
Thapar University
Patiala – 147004 (INDIA)

Dated: 20th July 2015
Place: Patiala, India

ACKNOWLEDGEMENT

Faith in the God and hard work are the greatest tools for success. Many hands involve and co-operate when you are moving on the path of success. I also came across with many people, who enlightened me with their knowledge and experiences during my Ph.D work. I would like to thank all the people who helped me to complete my thesis and leave an unforgettable picture of some beautiful moments in my mind.

First and foremost, I would like to express my deep sense of gratitude to my supervisor, **Dr. Puneet Sharma**, Associate Professor, Thapar University Patiala for his valuable guidance, encouragement and his paternally behavior throughout the work. His intuition and persistency are the key reasons that I could successfully finish each of research objectives. I doubt if I could have ever completed this work without his co-operation and consummate commend. I am glad to be his student; a millions thanks for making my dream come true.

I am also extremely indebted to my other supervisor, Professor **O. P. Pandey**, Dean Research and sponsored projects, for providing the possible research facilities here at Thapar University campus. He has specially contributed a lot to my thesis. Despite of his busy schedule he reviewed my thesis and gives his valuable suggestions. His steady courage and conviction will always inspire me.

I offer my special thanks to **Dr. Manoj Sharma**, Head, School of Physics and Materials Science, Thapar University Patiala, for providing all the necessary facilities in the department. I also wish to express thankfulness to **Dr. D.P. Singh** for his valuable guidance and all the faculty and staff of School of Physics and Materials Science for their support. I am thankful to my doctoral committee members; **Dr. B. N. Chudasama, Dr. S. D. Tiwari** and **Dr. Bonamoli Pal,** for their useful suggestions.

I can never forget to acknowledge the funding agencies for providing me financial assistance, the Council of Scientific and Industrial Research (CSIR) in the form of Senior

Research Fellow which buttress me to perform my work comfortably. With great appreciation I would like to acknowledge all my labmates, Mintu Tyagi, Shiwani Sharma, Chhavi, Anoop and all others research scholars at Thapar University Patiala. My special appreciation goes to my close friends Chandni Khurana, Samita and Suninder jeet Kaur for all their help and support throughout this study. I would like to thank SAI lab, Thapar university for XRD and SEM facilities and Dr. Andrea Paesano Jr., Departamento de Fisica, Universidade Estadual de Maringa′, Av. Colombo, Maringa′, Brazil for Mössbauer measurements.

I can never forget my parents whose boundless love, constant inspiration, emotional support and blessings has provided me encouragement at every step of life. My parents everlasting shower of blessing kept me moving easily with all hazards vanishing miraculously. My word power fails to express my feeling of gratitude to my loving brother and sister Kapil and Sakshi for encouragement and moral support during my work. I am really gratified to my sweet daughter Akshaya, whose smile inspired me in a special way when I got upset. Last but not least, I am also greatly indebted to my husband Mr. Yogender Verma, for his close companionship, sacrifices, constant inspiration and encouragement.

Samiksha Kumari

LIST OF PUBLICATIONS

1. **Samiksha Verma**, S.K. Dhawan, Andrea Paesano Jr, O.P. Pandey and Puneet Sharma, "Structural, magnetic and microwave properties of barium hexaferrite thick films with different Fe/Ba mole ratio", Journal of Magnetism and Magnetic Materials. 396 (2015) 308–312.

2. **Samiksha Verma**, O.P. Pandey, Andrea Paesano Jr. and Puneet Sharma, "Comparison of structural and magnetic properties of La^{3+} substituted $BaFe_{12}O_{19}$ prepared by different substitution methods", Physica B. 448 (2014) 57–59.

3. **Samiksha Verma**, Puneet Sharma , O.P. Pandey and Andrea Paesano Jr., An-Cheng Sun, "Structure and magnetic properties of $Ba_{1-x}La_xFe_{12}O_{19}$ prepared by $Ba_{1-x}La_xFe_2O_4$", IEEE Transactions on Magnetics. 50(1) (2014) 2101004-1 - 2101004-3.

4. **Samiksha Verma**, O.P. Pandey and Puneet Sharma, "Comparison between structure and magnetic properties of $BaFe_{12}O_{19}$ prepared by two different techniques", AIP Conf. Proc. 1536 (2013) 993-994.

5. **Samiksha Verma**, O.P. Pandey, Andrea Paesano Jr., Puneet Sharma, "Structural and magnetic properties of Co-Ti substituted barium hexaferrite thick films", Journal of alloys and compounds. (Revision submitted)

CONFERENCE PRESENTATIONS

1. **Samiksha Verma**, O.P. Pandey, Andrea Paesano Jr., An-Cheng Sun and Puneet Sharma, "Structural and magnetic properties of La^{3+} substituted barium monoferrite, $Ba_{1-x}La_xFe_2O_4$", International Conference on Magnetic Materials and Applications (ICMAGMA), Pondicherry University, Pondicherry, India, Sep. 15-17 (2014).

2. **Samiksha Verma**, O.P. Pandey, Andrea Paesano Jr. and Puneet Sharma, "Comparison of structural and magnetic properties of La^{3+} substituted $BaFe_{12}O_{19}$ prepared by different substitution methods", International Conference on Magnetic Materials and Applications (MAGMA), IIT Guwahati, Assam, India, Dec. 5 -7 (2013).

3. **Samiksha Verma**, O.P. Pandey and Puneet Sharma, "Comparison between structure and magnetic properties of $BaFe_{12}O_{19}$ prepared by two different techniques", International Conference on Recent Trends in Applied Physics & Material Science (RAM-2013), Govt. College of Engineering & Technology, Bikaner, Rajasthan, India, Feb 1-2 (2013).

4. **Samiksha Verma**, Baltej Singh Gill, O.P. Pandey, Puneet Sharma, "Effect of particle size on the magnetic properties of barium hexaferrite bonded magnets", Swami Vivekanand Institute of Engineering & Technology, Rajpura, India, Oct 20-21 (2012).

5. **Samiksha Verma**, Pooja Chauhan, O.P. Pandey and Puneet Sharma, "Preparation and characterization of barium hexaferrite prepared from barium monoferrite", 23rd Annual General Meeting of Materials Research Society of India (AGM: MRSI), Thapar University, Patiala, India, Feb 13-15 (2012).

TABLE OF CONTENTS

LIST OF FIGURES

LIST OF TABLES

SYMBOLS USED

M_s	Saturation magnetization
H_a	Magnetocrystalline anisotropy
H_c	Coercivity
M_r	Remanent magnetization
ω_o	Natural precessional frequency
H_{eff}	Internal magnetic field
K_1	Anisotropy constant
γ	Gyromagnetic ratio
ΔH	FMR linewidth
ω_r	FMR frequency
T_N	Neel temperature
T_c	Curie temperature
Y^{obs}	Observed profile
Y^{cal}	Calculated profile
R_p	Profile residual factor
R_{wp}	Weight profile residual factor
R_{exp}	Expected profile residual factor
χ^2	Chi square
C.S.	Crystallite size
β	Full width half maxima
B_{hf}	Hyperfine field
QS	Quadrupole splitting
IS (δ)	Isomer shift
Γ	Line width

ABBREVIATIONS USED

BaM	*M*-type hexaferrite, $BaFe_{12}O_{19}$
HF	High frequency
FMR	Ferromagnetic resonance
EM	Electromagnetic
XRD	X-ray diffraction
SEM	Scanning electron microscopy
VSM	Vibrating sample magnetometer
VNA	Vector network analyzer
FWHM	Full width half maxima
Hz	Hertz
MHz	Megahertz
GHz	Gigahertz
K_u-band	12-18 GHz
M-H	Magnetic hysteresis loop

ABSTRACT

M-type barium hexaferrite (BaM) thick films have gained considerable attention for high frequency device applications such as circulators, isolators, phase shifters and microwave absorbers. The characteristic features of BaM such as high magnetocrystalline anisotropy (H_a), high saturation magnetization (M), moderate coercivity (H_c) and high ferromagnetic resonance (FMR) frequency. FMR frequency can be tuned by varying intrinsic parameters such as H_a and M. Henceforth, the main objective of the present work is realization of screen printed BaM thick films with minimal porosity, tunable H_a and M_s. The screen printing technique is capable to produce films of few 100 µm thick, which overcomes the limitation to grow thick films by other deposition techniques such as RF sputtering and pulsed laser deposition (PLD) technique. To prepare BaM thick films, a paste of BaM powder and binder were screen printed on alumina substrate. Firstly, BaM powders were prepared by solid-state reaction and the effect of processing parameters such as powder size and sintering temperature on the structural properties is studied. To tune the M_s and H_a, variation of Fe/Ba mole ratio and suitable substitution for Ba and Fe ions are adopted. Further, BaM thick films with variable M_s and H_a are developed for their potential use in tunable high frequency applications. Various techniques were used to examine the structural, microstructural, magnetic properties and high-frequency characteristics of BaM powders and screen printed thick films. The magnetic properties of non-substituted and substituted BaM thick films suggest a possible candidate for microwave applications.

Chapter 1

INTRODUCTION

Overview

This chapter lists the characteristic features of M-Type barium ferrite as a high frequency magnetic material. The important properties required for high frequency applications are outlined. Comparative study of microwave ferrites and their properties are described. Finally, the motivation, objectives and outline of the present thesis is given.

1.1. Introduction

Recently, the research in the field of microwave devices operable upto 100 GHz frequency has gained considerable attention. As the operating frequency of microwave devices are shifting towards higher frequency bands, the requirement of low loss insulating magnetic material has increased. Ideal magnetic material must posses high magnetization with high magnetocrystalline anisotropy and ferromagnetic resonance (FMR) at high frequencies. Magnetic materials which satisfy the mentioned criteria are M-, Y- and Z-type hexaferrites. In comparison to other hexaferrites, M-type hexaferrites are more important due to large uniaxial magnetocrystalline anisotropy, high saturation magnetization and easy processing. These ferrites are extensively used for variety of micro- and millimeter wave device applications, such as millimetre wave filters, phase shifters and non-reciprocal devices.

The performance and behavior of microwave device mainly depends on the structural, magnetic and microwave properties of magnetic materials. The important properties required for high frequency applications are defined below:

Structural properties: For microwave and millimeter wave devices, magnetic materials in the form of thick films (> 50 μm) are required. The film thickness greatly affects the grain size; larger the thickness bigger is the grain size. For a good microwave device, film should have low porosity, high density and large particle size or grain size [1].

Magnetic properties: For high frequency (HF) applications, material must have high saturation magnetization (M_s), high remanent magnetization (M_r), high magnetocrystalline anisotropy (H_a), adjustable coercivity (H_c) and self biased [2]. M_s and M_r are intrinsic magnetic properties which depend on net magnetic moment originated by unpaired Fe^{3+} spins and H_c is extrinsic magnetic property that depends on particle size, grain shape and size.

Ferromagnetic Resonance (FMR): FMR is absorption of electromagnetic field by a ferromagnet material at a particular frequency that coincides with the natural precessional frequency (ω_0) of the electron in an internal effective magnetic field H_{eff}. The FMR frequency for a film is governed by the formulae;

$$\omega_{\mathrm{r}} = \gamma(H_{\mathrm{o}} + H_{\mathrm{a}} \pm 4\pi M_{\mathrm{s}}), \tag{1.1}$$

where H_{o} is applied magnetic field, H_{a} is magnetocrystalline anisotropy (H_{a} depends on K_1 and M_{s} according to relation $H_{\mathrm{a}} = 2K/M_{\mathrm{s}}$), γ is gyromagnetic ratio $= g\frac{e}{2m_{\mathrm{e}}} = 2.8$ MHz/Oe, g is splitting factor (2 for electron spin) and m_{e} is the electron mass. Eq. 1.1 depicts the strong dependence of FMR frequency on the intrinsic magnetic properties and further can be tuned by external applied magnetic field.

For OFF resonance devices such as circulators, isolators and phase shifters, magnetic material must have low loss, narrow FMR linewidth, and self-biased [3- 4]. While the ON resonance devices include microwave absorbers, required high losses at resonance frequency and broad band width that readily allow for the absorption of electromagnetic signal [5-6].

The FMR linewidth of spectrum is related to the relaxation times of magnetization presence of defects and inhomogeneities in the material. FMR linewidth (ΔH) can be defined as

$$\Delta H = \Delta H_i + \Delta H_a + \Delta H\,, \tag{1.2}$$

where ΔH_{i} is the intrinsic linewidth, ΔH_{a} is the broadening due to the random anisotropy axes of different grains and ΔH_{p} is broadening due to porosity [7].

1.2. Microwave ferrites

The important ferrites which can be used for microwave frequencies are spinels, garnets and hexagonal ferrites [8]. Spinel ferrites and garnets are the cubic ferrites. H_a for spinel ferrite is very small, of the order of 10s Oe. The zero field FMR frequency for spinel ferrites falls near or below 1 GHz [9]. Thus spinel ferrite can be operated only for *C* to S-bands. $Y_3Fe_5O_{12}$ (YIG) is one of the most important garnets for microwave applications due to its smallest FMR linewidth ΔH = 0.6 Oe [10-11]. As a result, YIG is commonly used in microwave devices operating below 1–2 GHz. However, the resonance frequency is even lower than that of spinel ferrite. To achieve FMR conditions with spinel and garnet in micro and millimeter wave range, large external biased field of 20 kG is required. Thus, spinel and garnet ferrites can widely be used only in lower end of millimeter band [12-14], seems to fall short on new demands. Therefore, both spinel and garnet ferrites are not suitable for high frequency application.

The hexagonal ferrites, which include M, U, W, X, Y and Z-type ferrite can be used for high frequency application due to their high magnetocrystalline anisotropy [9]. Among the hexagonal ferrites, *M*-type barium ferrite (BaM) is the compound of greatest technological interest due to its highest uniaxial H_a along *c* axis i.e. having the perpendicular anisotropy and moreover easy processing makes it suitable for micro/millimeter wave devices. W-, X- and Z- type compounds are not so economical because of their relatively difficult processing. The high magnetocrystalline anisotropy (H_a ~17kOe), self-biasing nature, and high ferromagnetic resonance frequency makes BaM as possible material for microwave and millimeter wave devices.

In contrast to spinel and garnet, the BaM have large H_a due to their hexagonal crystal symmetry. H_a of BaM is approximately 1000 times greater than that of spinel ferrites. The zero field FMR frequency of BaM is about 36 GHz, could be operated at K-band without any external magnetic field [9]. Further the self bias nature of BaM requires minimum external biasing field, which greatly reduces the size of the device. BaM also generates very low residual losses at high frequencies than soft ferrites. **Table 1.1** shows the comparative properties of different type of ferrites commonly used at microwave frequency [15-38].

Table 1.1. Magnetic and microwave properties of ferrites.

		Material	**$4\pi M_s$ (G)**	**H_a (Oe)**	**H_c (Oe)**	**T_N(°C)**	**f_r**	**ΔH (Oe)**
Spinel		$MgFe_2O_4$	2150 [15]	173 [16]	1.8	320	< 1 MHz	648
		$MnFe_2O_4$	4000 [17]	5400 [17]	196 [18]	340 [18]	< 300 MHz	600
		$CoFe_2O_4$	5370 [19]	6800 [19]	1566[20]	520		
Garnet		$Y_3Fe_5O_{12}$	1750 [21]	82 [21]		280 [22]	< 1 MHz	25
		$Y_3Fe_{5-x}Ga_xO_{12}$	400			167		50
Hexaferrite	M	$BaFe_{12}O_{19}$	4000 [23]	17460 [24]	3187 [8]	450 [25]	36GHz	
	M	$SrFe_{12}O_{19}$	4320 [26-28]	20000 [8]	3593 [8]	455 [27]	50GHz	
	U	$Ba_4Zn_2Fe_{36}O_{60}$	4223 [29]	10038 [29]	258 [30]	400	30GHz	
	X	$Ba_2Co_2Fe_{28}O_{46}$	3400 [31,32]	9500 [31]	50 [31]	467[31]	3GHz	
	Y	$Ba_4MnZnFe_{12}O_{22}$	2300 [33]	9500 [33]	60 [33]	100[34]		
	W	$BaCo_2Fe_{16}O_{27}$	4800 [35]	21000 [35]	80 [35]	430 [36]	3GHz	
	Z	$Ba_3Co_2Fe_{24}O_{41}$	3300 [37]	12000 [37]	23 [37]	400[38]	1.3 GHz	

Comparative study of ferrites shows that BaM hexaferrite is suitable material for high frequency applications.

1.3. Motivation and Objectives

BaM hexaferrite thick films have attracted considerable attention due to their significant application in high frequency applications. For high frequency device application, the films should have thickness of nearly few 100 microns. The screen printing technique is capable to produce films of few 100 µm thickness, which overcomes the limitation to grow thick films by other deposition techniques such as RF sputtering and pulsed laser deposition (PLD) technique. The properties of thick films for high frequency application primarily depend upon the structural and intrinsic parameters. For low losses, high density films with low porosity are required. On the other hand, properties such as FMR depend upon intrinsic parameters i.e. H_a and M. Therefore, realization of screen printed BaM thick films with minimal porosity and tunable H_a and M_s is the main objective of this thesis. Firstly, the effect of processing parameters such as powder size and sintering temperature on the structural properties is studied. Secondly, BaM thick films with variable M_s and H_a is developed for their potential use in tunable high frequency applications. The primary approaches adopted to vary the M_s and H_a is by varying Fe/Ba mole ratio and suitable substitution for Ba and Fe ions. Adopting the said approaches for the present thesis, the work is wanted to achieve the following objectives:

1. To investigate the effect of process parameters on the structural and magnetic properties of BaM thick films.

2. To investigate the effect of Fe ion vacancy on the magnetic properties of BaM thick films. The Fe ion vacancy is created by varying Fe/Ba mole ratio.

3. To study the effect of La^{3+} substitution for Ba^{2+} and Co^{2+}-Ti^{4+} ion substitution for Fe^{3+} on the structural and magnetic properties of BaM thick films.

On the basis of said objective, the present thesis is organized into following chapters:

Preceding **Chapter 1** gives brief introduction about the structural, magnetic and microwave properties of magnetic materials required for microwave application. A comparative study among common microwave ferrites is presented. Finally the motivation and objectives of the present work are mentioned.

Chapter 2 deals with extensive literature review on M-type hexaferrite. The classification of hexagonal ferrites on the basis of its composition is explained. Emphasis has been given on M-type hexaferrite, in particular on barium hexaferrite (BaM). Important research work related to processing of BaM and effect of substitution for Ba and Fe is reviewed. Further, important studies on hexaferrite films deposited by different techniques are discussed.

Chapter 3 gives the detail description of processing method adopted for the preparation of BaM powder and films. Various techniques used for the structural, magnetic and microwave characterization are explained briefly.

Chapter 4 investigates the effect of various process parameters such as calcinations temperature, ball milling time and sintering temperature on the phase formation, film morphology and magnetic properties. Further, effect of Fe^{3+} ion vacancy in BaM has been investigated. The Fe^{3+} ion vacancy is created by varying Fe/Ba mole ratio. Preferential site occupation of Fe^{3+} ion at five different crystallographic sites with mole ratio is analyzed by Mössbauer measurements. Structural and magnetic properties of BaM thick films (~ 60 μm) prepared by different mole ratio powder are discussed.

This chapter also deals with the substitution of rare earth metal La^{3+} in BaM. The effect of La substitution on structural and magnetic properties of $Ba_{1-x}La_xFe_{12}O_{19}$ ($x = 0.0 - 0.2$) prepared by two different methods is studied. In first method, La^{3+} substituted BaM is directly prepared by solid state synthesis from Fe_2O_3 and $BaCO_3$ with Fe/Ba molar ratio of 6:1. In the second method, solid state synthesis of Fe_2O_3 and $Ba_{1-x}La_xFe_2O_4$ in molar composition of 5:1 has been adopted. The variation of structural properties and magnetic properties with different substitution methods are compared. Further, screen printed BaM films with the substituted powder is prepared and their structural and magnetic properties are measured.

In subsequent part of the chapter, Co-Ti substituted BaM powder with $BaFe_{12-x}Co_xO_{19}$ $BaFe_{12-x}Ti_xO_{19}$ ($x = 0.0 - 2.0$) and $BaFe_{12-2x}Co_xTi_xO_{19}$ ($x = 0.0 - 1.0$) are studied. Individual substitution of Co and Ti is not favorable for single phase hexaferrite at higher substitution. The preferential site occupation of Co^{2+}-Ti^{4+} ion for Fe^{3+} ion is measured by Mössbauer spectroscopy. Consequently, Co-Ti substituted BaM thick films are studied. The variation in magnetic properties with substitution is correlated with site occupation. Lastly, an attempt has also been made to measure the microwave property i.e. reflection losses (R_L) in the frequency range of 12-18 GHz for BaM powder with different mole ratios.

Chapter 5 summarizes the results of various experiments obtained from the study. In the end, future work in the area is outlined.

Chapter 2

LITERATURE REVIEW

Overview

In this chapter an effort has been made to provide a detailed review of historical development of ferrites. Classification of hexagonal ferrites on the basis of its composition is given. The crystal structure and magnetic structure of barium hexaferrite are outlined. The magnetic properties of M-type ferrite are tabulated. Research work undertaken by various researchers for the preparation of barium hexaferrite powders/thick films and the effect of substitution on the magnetic and microwave properties are discussed.

2.1. History of ferrites

Ferrites have been investigated after the II world war at the Phillips Laboratories by Snoek and his co-workers [39-40]. In 1948, Neel described the term ferrimagnetism and also offered a theoretical interpretation to the magnetic properties of ferrites [41]. Anderson has given the theory of super exchange interaction, which helped to study the ferrites [42]. M-type hexagonal ferrite was discovered by Went [43] and in 1957 complete ferroxplanna hexagonal ferrites were discovered by Jonker *et al.* [44]. The first microwave device was realized by Hogan [45] in 1952.

2.2. Hexagonal ferrites

Hexagonal ferrites are magnetic iron oxide that grows in hexagonal crystal structure. Based on chemical composition hexagonal ferrites are classified into M-, U-, W-, X-, Y- and Z-types. The chemical composition of various hexagonal compounds, as a part of ternary compositional diagram is shown in **Fig. 2.1** [46]. **Table 2.1** shows the different type of hexagonal ferrite with their respective formulae.

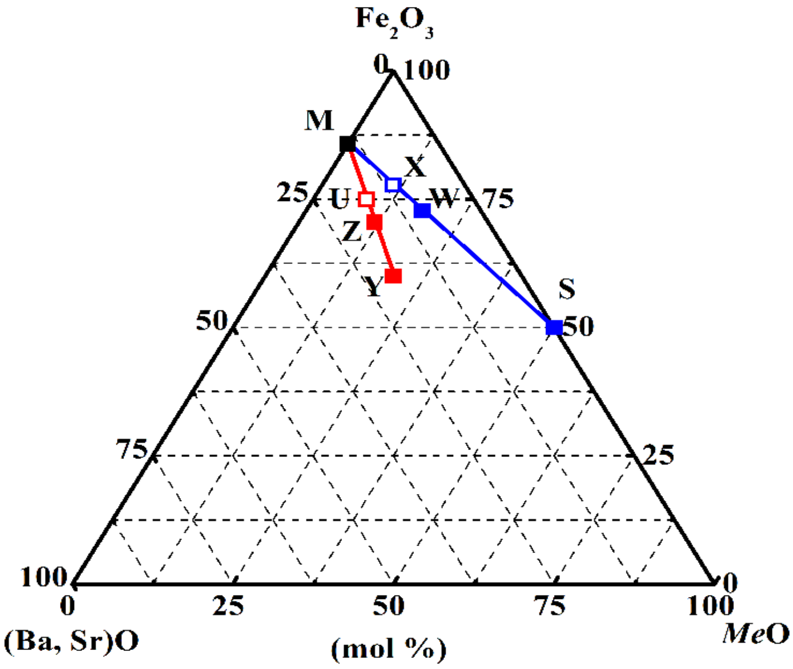

Fig. 2.1. Compositional diagram of hexagonal ferrites.

Table 2.1. Classification of hexagonal ferrites.

Type of hexaferrite	Chemical formula	Abbreviation	No. of molecules per unit cell
M	$BaFe_{12}O_{19}$	BaM	2
U	$Ba_4Me_2Fe_{36}O_{60}$	BaU or Me_2U	1
W	$BaMe_2Fe_{16}O_{27}$	BaW or Me_2W	2
X	$Ba_2Me_2Fe_{28}O_{46}$	BaX or Me_2X	3
Y	$Ba_2Me_2Fe_{12}O_{22}$	BaY or Me_2Y	3
Z	$Ba_3Me_2Fe_{24}O_{41}$	BaZ or Me_2Z	2

2.3. M-Type Hexaferrite

M-type hexaferrite includes $PbO.6Fe_2O_3$ (PbM), $SrO.6Fe_2O_3$ (SrM) and $BaO.6Fe_2O_3$ (BaM). M-type hexaferrites are isomorphous with the mineral magnetoplumbite. M-type hexaferrite was originally examined in the late 1930s by Adelskold [47] and further studied by Gorter and Braun at Philips in the 1950s [48-49]. **Table 2.2** shows the comparison between magnetic properties of M-type hexaferrite. Among these ferrites, BaM is of great interest for scientists, due to its unique properties associated with its crystalline structures and H_a [50-51]. Its characteristic features are moderate M_s, relatively low H_c, high H_a along c-axis, and high ferromagnetic resonance (FMR) frequency, with relatively narrow FMR linewidth (ΔH). Owing to these properties, BaM has a wide range of applications in high performance permanent magnetic material, magnetic recording media, and high frequency applications.

Table 2.2. Comparison among magnetic properties of M-type hexaferrites [8].

Hexaferrite	M_s(emu/g)	H_c(Oe)	H_a (Oe)	Nature
$BaFe_{12}O_{19}$	70	3187	17000	Non-toxic
$SrFe_{12}O_{19}$	70	3593	20000	Non-toxic
$PbFe_{12}O_{19}$	54	5001	13500	Toxic

2.4. Crystal structure of BaM

In 1938, Adelskold reported that the crystal structure of BaM is isostructural with naturally occurring magnetoplumbite having space group of $P6_3/mmc$[47]. One unit cell of BaM contains two formula units. The 24 Fe^{3+} ions are distributed among five different crystallographic sites: three octahedral (12*k*, $4f_2$ and 2*a*), one tetrahedral ($4f_1$) and one bipyramidal site (2*b*), as illustrated in **Fig. 2.2**. Later, Braun [49] described the crystal structure of BaM as a sequence of two structural units RSR*S*, where S $(Fe_8O_8)^{2+}$ is the spinel blocks, and R $(BaFe_6O_{11})^{2-}$ is the hexagonal block. S*and R* blocks are similar to S and R, but have a rotation of 180° around the c-axis. Magnetic structure of BaM first time was explained by Neel in 1948 and Anderson in 1950 [41-42]. According to them, the magnetization of BaM comes from Fe^{3+} ions, carrying a magnetic moment of 5 μ_B. Fe^{3+} ions are aligned either parallel or anti parallel ferromagnetic interaction through oxygen ions produced superexchange interaction. The exchange scheme of BaM is illustrated in **Table 2.3**. In one unit cell 16 Fe^{3+} ions are present at 12*k*, 2*a* and 2*b* sites with up spin and 8 Fe^{3+} ions at $4f_2$ and $4f_1$ sites with downspin. Total magnetic moment per unit cell is $(M_s) = 5\ \mu_B \times (12 - 4 + 2 - 4 + 2) = 40\ \mu_B$.

Table 2.3. Wycoff positions and direction of magnetic moment of Fe^{3+}in one formula unit of BaM.

Coordination	**No. of positions**	**Wycoff's notation**	**Direction of magnetic moment per formula unit**
Octahedral	12	*k*	↑↑↑↑↑↑
	4	f_2	↓↓
	2	*a*	↑
Tetrahedral	4	f_1	↓↓
Trigonal bipyramidal	2	*b*	↑

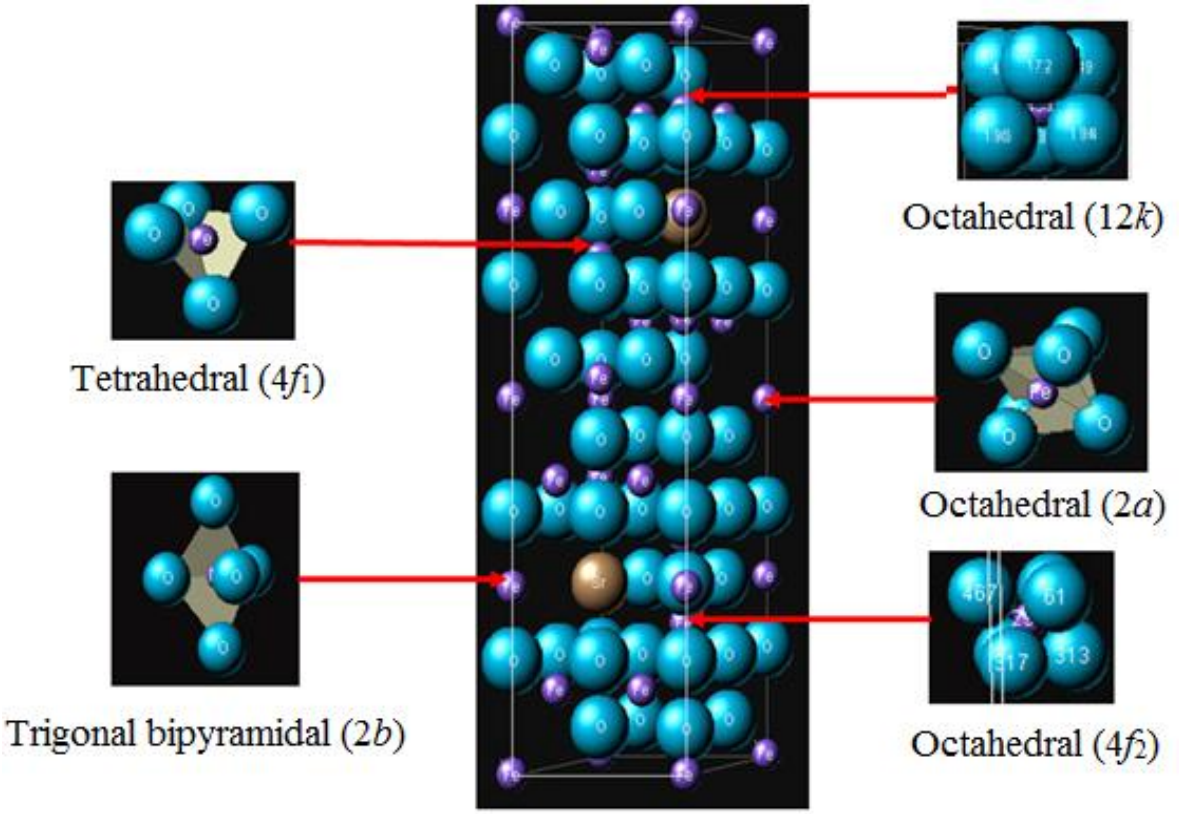

Fig. 2.2. Unit cell of $BaFe_{12}O_{19}$

2.5. Previous investigation on BaM powders

The following section reviews the important work done on M-type hexaferrite especially on barium hexaferrite. First, the work related to the processing of BaM, followed by effect of various ion substitutions is discussed. In the last, the research works carried out on BaM films are reviewed.

2.5.1. Single phase BaM

Extensive work for the development of single phase BaM was carried out by different research groups. The processing of BaM through different processing methods is well reported. The most common processing techniques adopted are conventional solid state reaction [52-53], co-precipitation [54-55], sol-gel [56-57], hydrothermal [58-59], glass crystallization [60] and combustion method [61] etc. Solid state synthesis method is simplest, cheapest and well acceptable for preparation of BaM powders. It is found that preparation methods are responsible for different magnetic as well as microwave properties. Further properties of ferrites can be tuned by varying density, grain size, chemical composition and grain alignment.

Fe/Ba molar ratio play important role in the formation of single phase BaM. Wang *et al*. [62] prepared BaM from $BaCO_3$ and Fe_2O_3 by varying Fe/Ba ratio from 2 -12 followed by heat treatment at 450 -1000 °C. Single phase BaM was obtained only for Fe/Ba ratios of 11 and 11.5, consistent with work reported by Janasi *et al*. [63]. For molar ratios below 11, secondary phases of $BaFe_2O_4$ and Fe_2O_3 coexist with BaM [62].The optimum Fe/Ba ratio is also greatly dependent on synthesis method. It was reported that 11 is the optimum Fe/Ba ratio for sol–gel combustion method [64], and 11.4 for sol–gel method [65]. Jean *et al*. [66] claimed that the optimal Fe/Ba ratio for hydrothermal method is 8, being single phase at 1000 °C. They observed the formation of secondary phases; Fe_2O_3 and $BaFe_2O_4$, for Fe/Ba molar ratio above and below 8.

2.5.2. Substituted BaM

Extensive work has been done to tailor the magnetic and microwave properties of BaM by various substitutions at Ba^{2+} and Fe^{3+} sites. The substitution by magnetic and non-magnetic ions results a wide range of saturation magnetization that helps to cover the wide range of microwave spectrum. A brief description of work carried out in past few years is as follows:

2.5.2.1. Substitution at Ba^{2+} site

In order to improve the magnetic properties of BaM hexaferrite, various rare earth substitution on Ba^{2+} site (RE = La^{3+}, Pr^{3+}, Sm^{3+}, Nd^{3+} etc.) were reported [67-68]. Replacement of divalent Ba^{2+} or Sr^{2+} by trivalent RE^{3+} is associated with a valance change of Fe^{3+} to Fe^{2+}, which further changes the magnetic properties of compound. In

1974, Lotgering *et al*. [69] and Kupferling *et al.* [70] found H_a increased with increase in La^{3+} concentration and was maximum for $LaFe_{12}O_{19}$.

The influence of La^{3+} substitution on structure and magnetic properties of SrM hexaferrite, prepared by ceramic and sol-gel methods has been studied by Liu *et al* [71-72]. They found that with La^{3+} substitution, M_s and H_c increases first and then decrease gradually. Mössbauer spectra demonstrate that the substitution of Ba^{2+} or Sr^{2+} by La^{3+} was associated with a valance change of Fe^{3+} to Fe^{2+} at $2a$ and $4f_2$ sites. Curie temperature was found to decrease with increase with La^{3+} substitution. The single phase of SrM hexaferrite was found for lower La^{3+} substituted hexaferrite. However for higher La^{3+} substitution, the secondary phases of α-Fe_2O_3 and $LaFeO_3$ were detected [73]. An important magneto-optical activity of 3 eV was also observed in La^{3+} substituted SrM [74]. Novak *et al.* [75] investigate the electronic structure of La^{3+} substituted SrM hexaferrite using density functional theory and generalization gradient approximation (GGA). Their results also agreed with experimental results, that magnetic moment decreases linearly with increasing La^{3+} content.

Ounnunkad *et al.* [76-77] prepared La^{3+} substituted BaM hexaferrite by citrate combustion method and found that with increase in La^{3+} substitution M_s increased first and then decreased, whereas H_c remarkably increased. Similar trend were also found by Nga *et al.* [78]. The enhancement of H_c was due to increase in H_a and reduction of grain growth. Recently, Sozeri *et al*. [79] made an effort to improve magnetic properties of La^{3+} substituted BaM hexaferrite with unusually low Fe/Ba molar ratio.

Charge distribution was investigated by Pieper *et al*. [80] and magnetic properties were studied by Lechevallier *et al.* [81-82] and Grossinger *et al.* [68] in rare-earth doped hexaferrites (R = La^{3+}, Nd^{3+}, Sm^{3+}). Nd^{3+} and Sm^{3+} substitution increased the intrinsic H_c without any significant change in M, whereas La^{3+} substitution show a very small effect in H_c of SrM. The addition of rare earth metal causes grain reduction, which increased the H_c. Mössbauer spectra showed that the higher substitution of RE^{3+} ions did not enter into the M-phase completely, but lead to an another extra phase. Jalli *et al.* [83] studied the effect of Sm^{3+} substitution to control uniaxial H_a. They found that as the percentage of Sm^{3+} increases from 0.79 mol % to 1.17 mol %, the uniaxial H_a increased from 19.5 to 25 kOe, respectively. The room temperature FMR measurement showed FMR linewidth ΔH of 85 Oe at 53 GHz. The large H_a and the narrow ΔH of crystal, enhanced the FMR frequency operation at relatively low external bias fields for microwave devices. Lixi *et al*. [84] prepared Sm^{3+} doped barium hexaferrite by ball milling and successfully achieved single phase BaM, by calcining the powder at 1250 °C. Substitution of Sm^{3+} ions convert Fe^{3+} to Fe^{2+} ion that results in the enhancement of magnetic loss properties and microwave absorbing performance.

Litsardakis *et al*. [85-88] published the series of results for Ba and Sr hexaferrites by doping Gd^{3+}, Dy^{3+} and Gd^{3+}-Co^{2+} ions. Doped hexaferrites showed a small increase in M_s and M_r upto $x = 0.1$. While, H_c gave a remarkably high values at $x = 0.2$ for Gd doped BaM (293 kA/m) and Dy doped SrM (305 kA/m). Enhancement in H_c was explained by inhibition mechanism of grain due to presence of Gd. In 2010, Stergiou *et al.* [89] studied the dielectric and magnetic properties of Gd^{3+} and Dy^{3+} substituted BaM in 2-18 GHz frequency range and investigated the difference between Gd- and Dy-doped hexaferrites.

2.5.2.2. Substitution at Fe^{3+} site

Various ions such as, Al^{3+} [90], Mn^{3+} [91], Mn^{3+}-Ti^{4+} [92], Co^{2+}-Ti^{4+} [93] etc, can be substituted for Fe^{3+} site in BaM. Magnetic properties and FMR frequencies of substituted ferrites were investigated on the fact that, their structure is closely related to the chemical composition and arrangement of ions in the crystal unit cell.

Researchers also substituted Al^{3+} by self-propagating combustion method [94], hydrothermal precipitation [95], chemical coprecipitation method [96], sol-sel [56], solid state reaction [52] and microwave combustion [97] methods. Al^{3+} was completely soluble in hexaferrite upto $x > 1.0$ [98]. Since the ionic size of aluminum is small as compared to Fe ions, hence crystallite size (*C.S.*) found to decrease with increasing the Al substitution [52]. The presence of non magnetic Al^{3+} ion for Fe^{3+} site, lead to the decrease in both M_r

and M_s. The H_c value initially increased and reached to maximum value of 617 (at 298K) and 547kA/m (at 77 K) for $x = 2.0$, and then decreased with the increase in Al content. Increase in H_c was associated with the decreased of *C.S.* due to the substitution of Fe^{3+} by Al^{3+} [99]. Al^{3+} substitution showed a great effect on H_a and ω_r [95]. H_a and ω_r increased with increasing substitution amount. Electromagnetic studies showed that the real part of complex permittivity increased and imaginary part of the complex permeability shifted towards high frequency range for Al^{3+} substituted hexaferrite [94].

In 1995, Wartewig *et al*. [100] first investigated Cr^{3+} distribution in Cr-doped BaM ferrites by solid state synthesis. Both lattice parameters '*a*' and '*c*' systematically decreased with increasing Cr content, due to relatively small ionic radius of Cr^{3+} compared to Fe^{3+}. Ounnunkad *et al*. [101] found a systematic decrease in M_s and an increase in H_c with Cr^{3+} concentration ($x = 0.0 - 0.8$). The decrease in M with Cr^{3+} substitution was related with the replacement of less magnetic moment of Cr^{3+} (3 μ_B) as compared to Fe^{3+} (5 μ_B). The declined grain growth with Cr^{3+} substitution was responsible for higher value of H_c. Contradictory results were published by Dhage *et al*. [89] by preparing Cr^{3+} doped hexaferrite with sol-gel auto-combustion technique. They found H_c also decreased with increase in Cr^{3+} content.

Decrease in M_s and increase in H_c was also observed in Mn^{3+} substituted hexaferrite [91]. The lower value of M was attributed due to the reduction of average magnetic moment of the lattice and a high value of H_c was obtained due to the reduction in *C.S.* respectively. For Mn doped hexaferrite, Bukhtiyarova *et al.* [102] found that hexaferrite phase formed after calcination temperature at 800 °C.

An unusual study based on La^{3+} substitution for Fe^{3+} site is also reported [103]. However, the substitution of La^{3+} for Fe^{3+} is virtually not possible because of large ionic radii difference. The reported results are as follows. M_s increased and H_c decreased with increase in temperature from 700 °C to 1000 °C, while M_s and H_c increased first with La^{3+} substitution $x = 1.0$ and then decreased for higher substitution [104]. Increased H_a was observed in La^{3+} substituted samples. Crystallographic distortion was also observed in La-doped samples due to lattice expansion, as the radius of La^{3+} ion is very larger than those of Fe^{3+}. A similar increase in H_c was also observed for Ho-doped hexaferrite [105]. Ankush *et al.* [106] found resistivity of the order of 10^9 Ωcm for La^{3+} substituted hexaferrite.

Substitution of Fe^{3+} with various combinations, such as Co^{2+}-Ti^{4+} [93], Co^{2+}-Sn^{4+} [107] Mn-Co [108], Zr-Mn [109], Ni-Zn [110] were also investigated. The purpose of simultaneous substitution of di-valent and tetra-valent ions was to develop the charge compensation in the system. Despite many studies on simultaneous substitutions, the most extensive studies were based on Co-Ti ions. Such hexaferrite ($MCo_xTi_xFe_{12-2x}O_{19}$) reportedly gives excellent magnetic and microwave properties [111]. In 1960, Smit *et al.* [112] was first who studied magnetic properties of prepared Co^{2+} doped hexaferrite and found relatively small H_c without any loss in M_s. Commercially, Toshiba in 1980s developed Co-Ti doped hexaferrite with H_c of 159 kA/m [113]. Various techniques have been explored to prepare single phase Co-Ti doped hexaferrite [114-117]. Low temperature Co-Ti substituted BaM has been prepared by Chen *et al.* [118] for low temperature co-fired ceramic (LTCC) multilayer devices. Co-Ti substituted samples showed enormous drop in H_a due to its changing behavior from axial to planer [119]. Guan *et al.* [120] found that M increased and reached to maximum value at $x = 0.5$. The increase in magnetization can be attributed to the partial substitution of Fe^{3+} ions by low spin Co^{2+} (3 μ_B) on antiparallel $4f_2$ site and replacing of Ti^{4+} ions on $2b$ site. Curie temperature T_c shifted to lower temperature (491 K) for $x = 2.5$. Drop in H_a was observed, due to Ti^{4+} ions that occupy $2b$ site and Co^{2+} occupies $4f_2$ site, which leads to major contribution for H_a. Magnetization decreases slightly, while H_c drops dramatically for higher substitution. Such kinds of properties are suitable for perpendicular magnetic recording and microwave device applications [116].

The effect of dc magnetic field on magnetic loss tangent and antenna radiation performances was investigated by Lee *et al.* [121]. Magnetic loss tangent decreased dramatically from 11.8% to less than 1% at 200 MHz with increasing dc magnetic field from 0 to 400 Oe. A small dc magnetic field increased antenna radiation efficiency from -

22.9 to -9.2 dB, hence high efficiency antennas can be realized with a small dc magnetic field. Microwave absorption properties of $BaCo_xTi_xFe_{12-2x}O_{19}$ in K_a band were studied by Kim *et al.* [122] and Dong *et al.* [123]. A wide bandwidth of microwave absorption was predicted in substituted samples compared to un-substituted samples. Therefore, $BaCo_xTi_xFe_{12-2x}O_{19}$ can be a good candidate for electromagnetic materials with low reflectivity in K_a band.

2.6. Hexaferrite Film

Research based on the development of BaM films is well reported. The techniques that have been adopted for the development of the films are given below:

1. *Physical vapor deposition*: includes RF sputtering, magnetron sputtering, ion beam sputtering, molecular beam epitaxy and pulsed laser deposition.
2. *Chemical solution deposition*: includes sol-gel and metal organic decomposition.
3. *Chemical vapor deposition*: includes metalorganic chemical vapor deposition and atomic layer deposition.

In the following section, various growth processes related to BaM and Strontium hexaferrite (SrM) thin or thick films are discussed. Emphasis is laid on the magnetic and microwave properties.

2.6.1. Pulsed Laser Deposition (PLD)

PLD technique is used to grow high quality films of garnet, spinel, hexaferrite materials and various ferroelectric oxide materials. In PLD, a laser pulsed beam is focused onto target such that the beam ablates the target material. The interaction of beam with target produces a molecular flux or plume of material towards the heated substrate.

The first BaM film grown on sapphire by PLD was reported by Dorsey and his co-workers in 1992 [124]. They reported that post annealing of films reduce H_c and ΔH. Later, researchers also deposited BaM films by PLD method. In 2000, Sc-doped barium hexaferrite films (2.2 - 5 μm) were deposited by Shi *et al.* [125] onto a sapphire substrate, with the crystallographic *c*-axis aligned normal to the film plane. At frequency 34 GHz, ΔH and H_c increased from 310 to 2000 Oe and 281 to 517 Oe with increase in thickness of film. While, Yoon *et al.* [126] subsequently reported in-plane uniaxial anisotropy and in-plane *c*-axis oriented Sc-doped barium hexaferrite films (2 - 3 μm) on sapphire substrate. Substitution of Sc cation for iron reduced H_a from 17 to 10 kOe. It was also reported that the film thickness above 2-3 μm promotes crack formation. The self resonant frequency of 32.8 GHz with ΔH of 1.3 kOe for Sc-doped films was reported.

Highly oriented BaM films deposited onto MgO (111) substrate were obtained in contrast to BaM film on Al_2O_3 substrate [127]. Yoon *et al.* [128] deposited film on MgO substrate with no cracks up to 28 μm. ΔH of 700 Oe at frequency 54 GHz was observed, which was considerably larger than previous reported value of ΔH = 66 Oe at 58 GHz for BaM films deposited on Al_2O_3 substrate. Etching of MgO substrate and annealing of film was employed to reduce magnetic loss. ΔH for thick films decreased from 66 Oe to 45 Oe upon removal of 75% of substrate. Further reduction in ΔH of 20 Oe was obtained after two hour annealing.

Majority of research has been focused on hexaferrite thick film deposition on (0001) Al_2O_3 and (111) MgO substrate, due to their excellent magnetic properties and microwave properties without any crack in films [129]. However, these films do not have dual functionality for truly self-biased microwave devices. To overcome this, BaM thick films (1 - 14 μm) was deposited onto a-plane (1120) sapphire substrate. Such films have (1010) orientation and exhibits dual functionally as gyrotropic media and permanent magnets.

To improve magnetic properties, Chen *et al.* [130] deposited BaM film on 6H-SiC (0001) substrate and obtained H_a greater than 15 kOe, but unable to obtained FMR peak to peak derivate ΔH less than 1000 Oe. In 2009, to improve the lattice mismatch and interdiffusion between film and substrate, BaM film was deposited by introducing 10 nm MgO (111) layer on 6H-SiC substrate. These films showed perpendicular H_a field of 16.9

kOe and a FMR peak-to-peak derivate of 96 Oe at 53 GHz [131]. Further the magnetic properties especially magnetic loss was decreased with etching [132].

A magnetic ferroelectric hetrostructure film with a large electric field tuning of FMR mode was also fabricated [133]. Beside BaM, SrM and PbM hexaferrite films were also deposited by PLD [134]. Co-Ti co-doped BaM and Al-doped SrM were deposited to optimize the magneto-optical properties [135-136]. Researchers have also investigated the effect of substrate temperature on structural, optical and magnetic properties of BaM films [137]. Also the effect of oxygen pressure during the growth of films has been investigated [138].

Masoudpanah *et al.* [139] studied the microstructural and magnetic properties of La-Co co-doped SrM films deposited on commercial Si(100)/SiO_2/Ti/Pt(111) substrate by PLD. In another work, they reported the effect of post annealing on SrM films deposited on Pt(400nm)/(Ti(400 nm)/SiO_2/Si substrate [140]. In most of the reports hexaferrite films were grown onto Al_2O_3 (0001) substrate, but the restriction of using this substrate is its cost. Films deposited on SrM/Pt(111) films have same microstructural and magnetic properties as SrM/Al_2O_3 (0001), thus replacement of Al_2O_3 (0001) substrate by the Si(100)/Pt(111) substrate is suggested [141].

PLD is also very effective technique for the growth of epitaxial *M*-type hexaferrite films. Hexagonal crystal structure can be grown at an atomic scale from multiple targets possessing technique referred as alternating target laser ablation deposition (ATLAD). This technique allows for the growth of complex magnetic structures and to tailor the specific requirements of M and H_a. In 1995, Karim and Vittoria [142] were the first who introduce the hexaferrite films by ATLAD to control ionic distribution in hexagonal unit cell, and later refined by Geiler *et al.* [143-144] and Mohebbi *et al.* [145]. Geiler *et al.* [144] prepared the PbM films by utilizing PbO and Fe_2O_3 on MgO substrate. These films were highly useful for lower microwave frequency applications due to low value of H_a (12 kOe). However, these deposited films also showed secondary phase, low saturation magnetization and broad FMR linewidth. To overcome these limitations, BaM films were deposited on Al_2O_3 substrate by alternatively ablating orthorhombic $BaFe_2O_4$ and hematite α-Fe_2O_3 targets. High quality of BaM was obtained with H_a of 16.5 kOe with narrowest ΔH of 42 Oe at frequency 52 GHz. Mohebbi *et al.* [145] change the $BaFe_2O_4$ target by $BaFe_4O_7$ and found a noticeable improvement in resistivity ($4.3 \times 10^2 - 7.2 \times 10^2$ Ω).

2.6.2. RF magnetron sputtering

Magnetron sputtering is widely used for fabrication of metals, ceramic and granular ferrite thin films. In sputtering, substrate is bombarded by energetic ions and the target atoms. The sputter ions travel through plasma and undergo many collisions with gas ions before deposition on substrate, which usually occurred at high temperature. Some time magnetic field is applied by using magnetron to increase the sputtering yield. Magnetic field increases electron residence time in the plasma, which leads to higher ion collision and hence higher discharge current.

Well defined *c*-axis oriented SrM ferrite films (2-3 μm) were synthesized by RF sputtering onto polycrystalline Al_2O_3 substrate at temperature 500 - 650 °C. At deposition temperature 600 °C to 650 °C, the film grains have random three dimensions *c*-axis orientations with M_r/M_s of 0.62. The H_c of film was found to increase by post-deposition annealing in O_2 [146]. Gee *et al.* [147] prepared multilayered BaM film (0.63 μm) on Si substrate and found that stacking of BaM layers, with *ex situ* annealing between each layer. Annealing after each layer deposition improves the *c*-axis orientation and H_a (17 kOe) as compared to H_a (14.5 kOe) of a single layered film with the same thickness.

Capraro *et al.* [148] studied the stress and transmission coefficient of *c*-axis oriented BaM thick films (1-10 μm) deposited on alumina and silicon substrates. The residual stress in the films was found to be compressive after deposition and a tensile upon annealing. However, the stress was much lower for films deposited on alumina than on silicon substrate. Transmission coefficient (S_{12} and S_{21}) of isolator show a non-reciprocal effect that reached to 3.3 dB/cm at frequency 50 GHz [149]. Magnetic properties were found to very close to the bulk BaM.

Dehlinger *et al.* [150] investigated morphological and magnetic properties of BaM thick film (10-15 μm) with high deposition rates by varying sputtering gas pressure from 3 to 20 Pa. Stoichiometry was obtained only for film deposited at pressure 3 Pa, however, excess of Ba was found for other films. The film density was also highest (5.0 g cm^{-3}) for film deposited at P = 3 Pa. Recently Mallick *et al*. [151] reported film density of 4.45 g/cc for Co doped BaM films.

Xu *et al.* [152] deposited BaM film onto sapphire substrate by altering pressures. With increase in pressure the thickness of film decreased and atomic ratios of Fe to Ba increased from 9.3 to 15.0. Surface morphology changed from platelet-like to needle-like crystalline because of more bombardment on the film under high pressure. The H_c was found to decrease monotonically with sputtering pressure.

The effects of processing parameters such as oxygen partial pressure, chamber pressure, and substrate bias on magnetic properties of BaM films were investigated by Zhuang *et al.* [153]. Morisako *et al.* [154-155] studied the influence of oxygen partial pressure and total discharge gas pressure on BaM films. They reported that the microstructure and magnetic properties of BaM films strongly depend on the processing parameters and on film thickness. The film thickness also greatly affects the nucleation sites and strain in films, which were responsible for different textures and *c*-axis orientations of BaM films.

Xu *et al.* [156] reported that the crystallographic, morphological and magnetic properties of BaM thin films strongly dependent on thickness. Thin films of 150 nm showed excellent perpendicular *c*-axis orientation. Randomly orientation increased as thickness increased to 500 nm, due to increases of random nucleation sites. M_s and H_a also decreased with increase in thickness.

Substrate effect on orientation of BaM films have been studied by depositing films with target facing sputtering (TFS) on SiO_2, ZnO, GGG and Al_2O_3 substrates [157]. High H_c (2200 Oe), *c*-axis oriented Co-Ti doped BaM films have been achieved by rf sputtering and post annealing. Co-Ti reduces the grain size with improved *c*-axis in plane orientation. Film H_c was controlled over a wide range through the diffusion process [158]. Magneto optical properties of Pr-Ni [159] and CoTi [160] substituted BaM on GGG substrate were studied. Gomi *et al.*[159] reported that Ni substitution induced a large negative faraday rotation, while no contribution of Pr^{3+} ion was observed.

Crystallographic and magnetic properties of SrM and BaM thin films can be improved by using appropriate substrate or underlayer. Various under-layer materials such as Pt [161], Au [162] and Al_2O_3 [163] were studied. These films exhibit strong perpendicular *c*-axis orientation. The maximum H_c and M_r/M_s of 5.7 kOe and 0.86 for Au under layer and 4.9 kOe and 0.61 for Al_2O_3 under layer was observed.

Hajndle *et al.* [164] and S. Srinath *et al.* [165] first time reported the growth conditions and properties of co-sputtered BSTO/BAM film (2 μm) and multilayers films of BSTO/BAM. They found that the presence of BSTO in the BaM films affected the H_a and shape anisotropy. Reduction in M_s and H_c were observed in multilayered samples, compared to pure BaM film. Narrowest ΔH was required for microwave devices, for which thicker poly crystalline film was needed.

The main advantages of rf sputtering is possibility to sputter on large area substrate, good adhesion of the film and ability to get stoichiometric and conformal films. However, the deposition of the films with limited thickness (10-200 nm) makes it impractical for most of microwave and millimeter wave applications, where thick films are required.

2.6.3. Floating zone method

Srinivasan *et al.* studied millimeter wave magnetoelectric interactions of high quality single crystal and film [166]. Ustinov *et al.* [167] developed Al^{3+} substituted single crystal and investigate magnetic and dielectric excitations for 100 μm thick films in sub-terahertz frequency range [168]. Al^{3+} substitution dramatically increased H_a from 17.88 kOe to 33.68 kOe and decreased M_s from 4.4 to 1.85 kG with maintaining ΔH. The use of single crystal Al^{3+} substituted BaM, reduce external magnetic field and consequently reduce weight and size of micro/millimeter wave devices. Particular $BaAl_2Fe_{10}O_{19}$ at 90 GHz would require a remarkably small applied field of 2.8 kOe. Pavlova *et al.* [169] also developed single crystal of Al^{3+} substituted BaM by floating zone method with optical heating and found that higher Al^{3+} content was not good for the crystal.

2.6.4. Liquid phase epitaxy (LPE)

LPE was first employed to deposit high quality YIG film by Linares in 1968 [170]. Hexagonal ferrite films prepared by LPE gained much attention in 20th century. The smallest ΔH of 27 Oe at 60 GHz was obtained for 45-50 μm BaM thick film, grown on both side of (111) MgO substrate [171]. To improve the thickness of films to 50 μm to 200 μm, Al_2O_3 substrate was used. The films grown on Al_2O_3 substrate required less hours of deposition time (30 μm/h) w.r.t. films grown film grown onto MgO substrate (0.05 μm/h). 200 μm thick film of BaM grown on double sided Al_2O_3 with *c*-axis aligned along the in-plane direction has ΔH of 70 Oe at 60 GHz [172]. Significant increase in growth rate of 20 μm/h was obtained for high quality BaM films deposited on single and double-sided (111) $Gd_3Ga_5O_{19}$ (GGG) substrate. This growth rate was five times greater than films grown on (111) MgO substrate [173]. Relatively narrow ΔH was measured to be 40 Oe for single sided and 67 Oe for double sided film deposited on GGG at 58 GHz. The *c*-axis found to aligned perpendicular for films deposited onto (111) GGG substrate, whereas in plane alignment was found for film deposited onto Al_2O_3 substrate [174]. Multi layers of BSTO/BAM films were also grown by liquid phase epitaxy using well textured BaM sputtered films as a seeding layer [175]. Symmetric FMR peaks as narrow as 41 Oe at 60 GHz were obtained.

2.6.5. Electron Beam Evaporation

Magnetic properties of in-plane oriented BaM films deposited on Si (100) substrate were studied [176]. To increase adhesion and reduce cracks, Wane [177] first deposited the film on the thin (1 μm) metallic underlayer of either Gold (Au), Copper (Cu) or Gold on Titanium (Au/Ti). Obtained deposition rate (≥ 40 μm/h) for electron beam deposition was quit high compared to PLD (1 - 30 μm/h). Magnetic properties were acceptable for realization of integrated circulator working at 77 GHz, but failed to obtain crystallographic orientation perpendicular to the film plane.

2.6.6. Spin Coating

In spin coating nitrates compounds was dissolved in a solvent to make sols. Finally, the achieved homogeneous solution was spin-coated onto substrate. The process was performed again and again to achieve the desired film thickness. Films deposited by spin coating are suitable candidate for high density recording media, but fail to meet the thickness needed for microwave and millimeter wave devices applications. Now a days, lots of work were reported on synthesis and magnetic properties of thin films prepared by spin coating [178-180]. Effect of citric acid [181] and effect of pH value [182] were also studied on the magnetic properties of hexaferrite films. Ghasemi *et al.* [183] investigated the magnetic properties of of Dy-Gd substituted SrM hexaferrite thin film and found that M and H_c increased with substitution amount.

2.6.7. Other methods

Magneto-optical characteristics of Co-Ti substituted BaM film (1 - 1.8 μm) deposited on SiO_2 substrate by dip coating method has been studied [184]. Ruikar *et al.* [185] prepared SrM films on Al_2O_3 substrate by chemical bath deposition and investigated the effect of pH value on the microwave properties of thin films. Thin film synthesis at pH 10 showed highly dense surface morphology and hence, high microwave transmittance of 65% in 8-12 GHz frequencies. These films also showed very high dielectric constant, permeability and very low losses. Molecular beam epitaxial growth technique was applied to grow

BaM hexaferrite film onto Mg(001)/SiC(0001) substrate [186]. Recently BaM film was also deposited onto SiC (0001) substrate. The selected area diffraction (SAD) patterns revealed crystallography relation in BaM(0001)||SiC(0001) and BaM(1010)||SiC(1010) [187]. MBE has great utility to study the properties of ferrite, but not suitable for microwave devices applications because of limited thickness of the film (10 - 200 nm).Various researchers also deposited hexaferrite films by atmospheric plasma spraying [188] and chemical solution deposition [189] methods, to study the orientation and magnetic properties of films.

2.6.8. Screen printing

Screen printing technique is capable to deposit thick films with thickness ranging from (50-500 μm). In screen printing, a paste of BaM powder and binder was printed onto the substrate followed by heat treatment. A group at the Northeastern University, Boston (USA) is actively involved in the development of the screen printed thick films. Important work carried out on screen printed BaM thick films are discussed below.

Yuan *et al.* [190] prepared SrM film (8 to 15 μm) by screen printing on alumina substrate and studied the effect of sintering temperature on magnetic properties. Highest H_a of SrM films was obtained at a temperature between 1200 °C and 1300 °C. These films were not fully dense and failed to meet the requirement of self biased microwave devices.

Chen *et al.* [7] prepared *c*-axis self-biased BaM thick films (100 - 400 μm) on alumina substrate, oriented under magnetic field of 8 kOe. At 40 GHz these polycrystalline thick films have H_a of 16.7 kOe, H_c of 2.4 kOe (in easy axis), a high M_r/M_s of 0.93 and line width ΔH of 1.2 kOe was obtained. Further high quality thick films (200-500 μm) with dense microstructure were developed by hot pressing [23,191]. Structure, magnetic and microwave measurement confirmed that these films were suitable for self-biased microwave devices with large remanance (3800 G) and low microwave loss. A minimum peak to peak ΔH, 320 Oe was observed at U band.

BaM thick films (50 -100 μm) were fabricated on silicon (100) substrate, with buffer layer of SiO_2 or Al_2O_3, to prevent the excessive diffusion [192-193]. These films have linewidth of 1.1 kOe at 28 GHz. Substituted Ba ferrite film were deposited on Al_2O_3 substrate by Chinnasamy *et al.* [194] to obtain in-plane aligned grains with moderate H_c and high M_r. A minimum ΔH of 860 Oe was achieved for In-doped BaM thick films.

The screen printing technique is capable to produce films of few 100 μm thick, which overcomes the limitation to grow thick films by other deposition techniques such as RF sputtering and PLD technique etc. However, these screen printed thick films have high FMR linewidth of the order of ~ 2 kOe which was too large for microwave devices. It was reported that this large ΔH is attribute to porosity in the films. Clearly, if the screen printing technique can be refined to produce thick films with dense microstructure without any porosity, it will offer unique potential to develop cost effective and scalable process microwave devices. Also FMR frequency can be tuned by various ion substitutions, therefore main focus of the study to develop BaM thick films with dense microstructure and tunable magnetic properties.

Chapter 3

EXPERIMENTAL PROCEDURE
&
TECHNIQUES

Overview

This chapter gives the detail description of processing methods adopted for the preparation of BaM powder and films. The basic principles of various techniques used for the structural, magnetic and microwave characterization are explained briefly.

3.1. Sample preparation

3.1.1 Preparation of powders

In the present thesis, Barium hexaferrite (BaM) powders were prepared by solid state reaction method. The basic chemical equation used for the formation is give below:

$$BaCO_3 + 6.Fe_2O_3 \longrightarrow BaFe_{12}O_{19} + CO_2 \qquad (3.1)$$

Following series of BaM powders were prepared:

i) Pure BaM Powder
ii) BaM powder with different mole ratio
iii) $Ba_{1-x}La_xFe_{12}O_{19}$ ($x = 0.0 - 0.2$)
iv) $BaFe_{12-x}Co_xTi_xO_{12}$ ($x = 0.0 - 1.0$)

High purity (99.0% Sigma-Aldrich grade) $BaCO_3$, Fe_2O_3, La_2O_3, Co_2O_3 and TiO_2 powders were used for the preparation of above mentioned series. Powders were weighed in desired composition and wet mixed in acetone media using a planetary ball mill. The ball-to-charge ratio was 2:1 and mixing time was 3 hours for all the experiments. The mixed powder was dried and pressed in the form of pellets and calcined in the muffle furnace. The calcination temperature and time were fixed to 1200 °C and 3 hours respectively. The heating and cooling rates were fixed to 5 °C/min. Calcined pellets were pulverized in vibrating micro mill using tungsten carbide grinding media. The pulverized powder was further milled in planetary ball mill in tungsten carbide media. The milling time was kept 1 hour for all the powders. The ball-to-charge ratio was fixed to 10:1. **Fig. 3.1** shows the flow chart for the preparation of BaM powders.

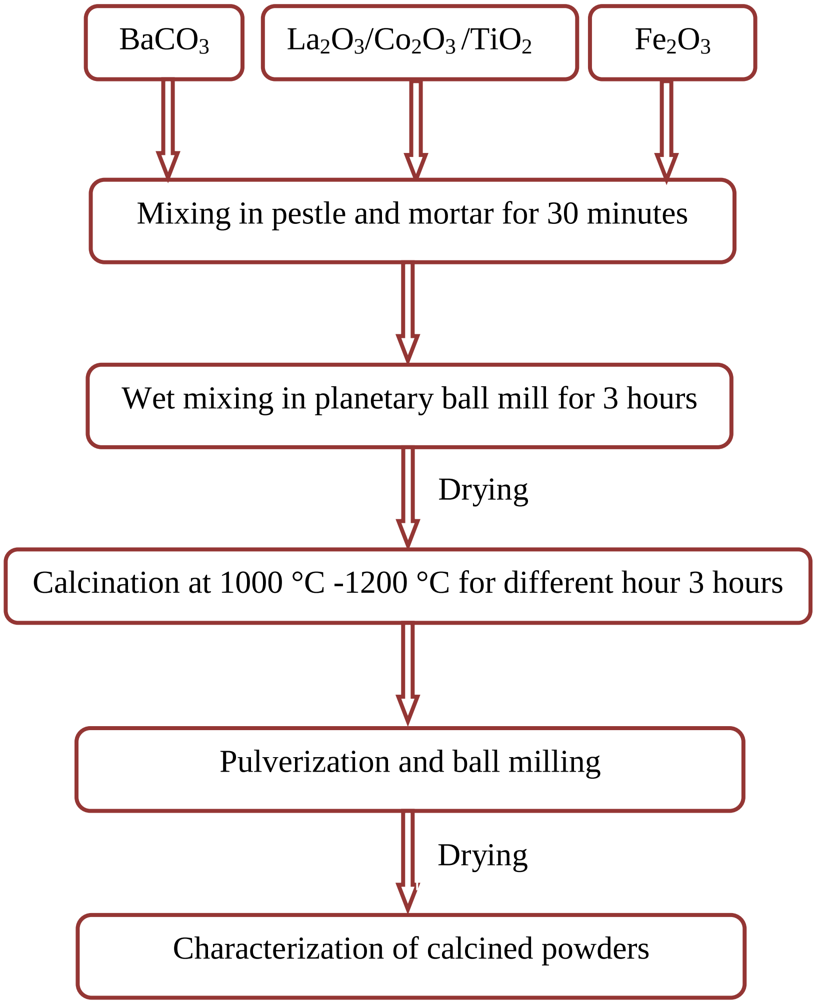

Fig. 3.1. Flow chart to prepare BaM powders.

3.1.2. Preparation of hexaferrite thick films

BaM thick films were prepared by screen printing method on alumina substrate (Al_2O_3). A paste of 85 wt % BaM powder, 5 wt % Bi_2O_3 and 10 wt % polyvinyl butyral (PVB) binder were prepared by mixing them thoroughly. Al_2O_3 substrate was ultrasonically cleaned for 1 hour. Stencil of thickness 50 - 100 μm was used to print rectangular disks of the BaM material on the substrate having dimensions 0.5 mm × 0.5 mm × 1.0 mm. The appropriate amount of paste was screen printed on Al_2O_3 substrate. Metallic blade or squeegee was employed to spread the paste on the substrate and to maintained uniform thickness of the film. Proper care has been taken while deposition to maintain uniform thickness. The printed films were dried in oven at 60 °C for 1 hour. The dried thick films were sintered in a muffle furnace at 1200 °C – 1300 °C for 2 hours. The heating and cooling rate was kept constant to 5 °C/min. **Fig. 3.2** shows the systematic diagram of screen printing method. **Fig. 3.3** shows the respective BaM film prepared by screen printing on Al_2O_3 substrate. **Fig. 3.4** shows the steps involved in the preparation of BaM thick films.

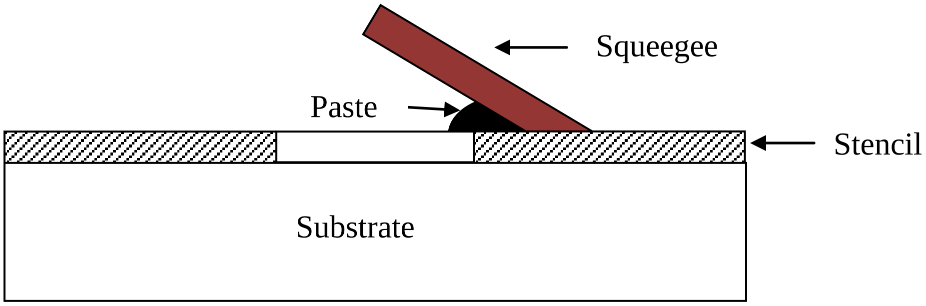

Fig. 3.2. Screen printing process to deposit BaM thick films.

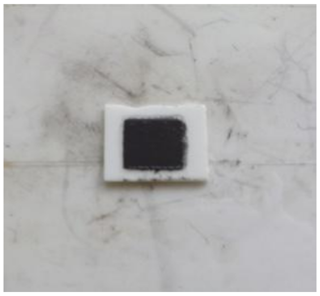

Fig. 3.3. BaM screen printed thick film deposited on Al_2O_3 substrate.

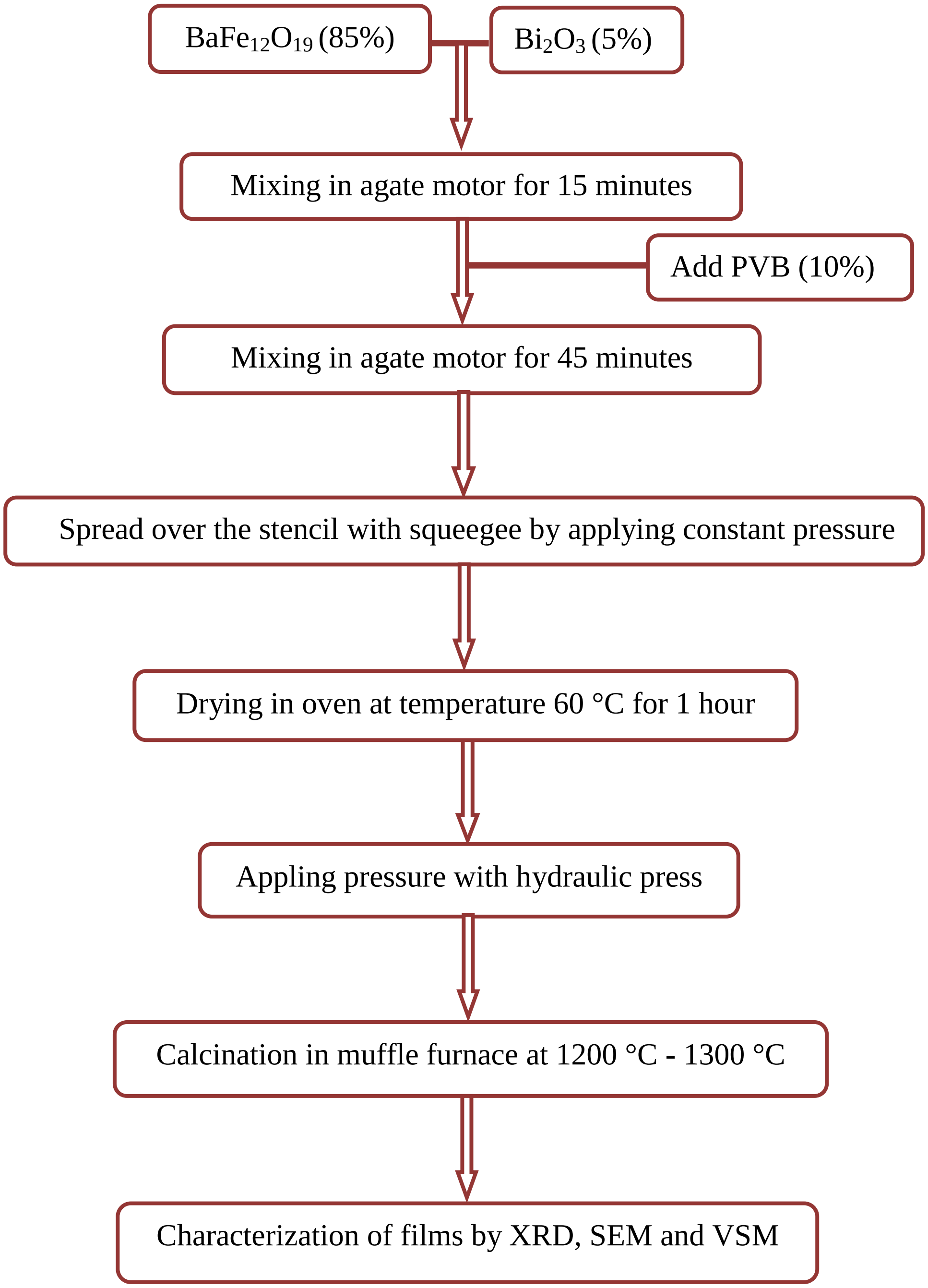

Fig. 3.4. Flow chart for the preparation of BaM thick film.

3.2. Characterization Techniques

Various characterization techniques were used to measure the properties of BaM powders and films. The characteristic tools involved were X-Ray Diffraction (XRD), Scanning Electron Microscope (SEM), Mössbauer Spectroscopy, Vibrating Sample Magnetometer (VSM) and Vector Network Analyzer (VNA). The techniques used for this work are discussed below:

3.2.1. X-Ray Diffraction (XRD)

The phase analysis of the calcined powders was carried out by X-ray diffraction (XRD), model X'PERT Pro-Panalytical using Cu-K_α radiation (λ = 1.5405 Å). The patterns were recorded in the 2θ range from 15° to 70° with a step size of 0.02°. All diffraction patterns were refined by Rietveld method using Fullprof suite software.

3.2.1.1. Rietveld Refinement

The refinement is a technique developed by Hugo M. Rietveld for the use of the characterization of crystalline materials [195-196]. Method of refining diffraction data helps to find the unknown crystal structure, percentage of different phases present in the sample, lattice parameters and crystallite size. The Rietveld refinement is an automatic procedure and uses a least squares approach to refine a theoretical line profile until it matches the measured profile. The minimized function (Φ) is given as:

$$\Phi = \sum_{i=1}^{n} W_i \left(Y_i^{obs} - Y_i^{calc}\right)^2 , \tag{3.2}$$

where W_i is the weight assigned to the i^{th} data points.

The principle of refinement is to minimize the difference of observed profile (Y_i^{obs}) and calculated profile(Y_i^{cal}). For good fitting both the patterns should overlap to each other i.e. $Y_i^{obs} - Y_i^{cal} = 0$. In refinement the profile residual factor (R_p), the weight profile residual (R_{wp}), the expected profile residual (R_{exp}) and chi square (χ^2) are obtained. Formulas for these factors are

$$R_p = \frac{\sum_{i=1}^{n} \left| Y_i^{obs} - Y_i^{calc} \right|}{\sum_{i=1}^{n} Y_i^{obs}} \times 100\% \;, \tag{3.3}$$

$$R_{wp} = \left[\frac{\sum_{i=1}^{n} W_i \left(Y_i^{obs} - Y_i^{calc} \right)^2}{\sum_{i=1}^{n} W_i \left(Y_i^{calc} \right)^2} \right]^{1/2} \times 100\% \;, \tag{3.4}$$

$$R_{exp} = \left[\frac{n-p}{\sum_{i=1}^{n} W_i \left(Y_i^{calc} \right)^2} \right]^{2} \times 100\% \;, \tag{3.5}$$

$$\chi^2 = \frac{\sum_{i=1}^{n} W_i \left(Y_i^{obs} - Y_i^{calc} \right)^2}{n-p} = \left[\frac{R_{wp}}{R_{exp}} \right]^2 , \tag{3.6}$$

For best fitted data χ^2should be near to one.

3.2.1.2. Determination of Crystallite Size (*C.S.*)

The average crystallite size of the samples can be determined from Scherrer's formula [197]. According to Scherrer's formula

$$C.S. = \frac{k\lambda}{\beta \cos\theta} \;, \tag{3.7}$$

where k is constant dependent on crystallite shape (0.89), λ is x-ray wavelength, β is FWHM (full width at half max) calculated from Caglioti equation $(u \tan^2\theta + v \tan\theta + w)^{1/2}$, function *u* ,*v* and *w* are the shape parameters obtained from refinement and θ = Bragg angle.

3.2.2. Scanning Electron Microscopy (SEM)

Scanning electron microscopy (SEM) is a powerful tool to examining the surface morphology i.e. the shape, size and arrangement of particles [198-199]. SEM provides greater magnification factors and depth of field compared to optical microscopes. The SEM microscope operates by emitting electrons from the gun which travel along the microscope column being focused by condenser and objective lenses until the final spot size is a few nanometers in diameter. This focused beam interacts with the sample causing excitation of electrons in the surface layers. Secondary and backscattered electrons are detected by detector which provides information about the surface of the sample.

In the present study, JEOL model 6510 was used for the microstructural examination of powders and films. A thin film of Au was sputtered onto the film surface to avoid any charging during SEM analysis. The thickness of the films was measured by observing cross sectional view of the films.

3.2.3. Vibrating Sample Magnetometer (VSM)

VSM is most common technique employed to measure and characterized magnetic materials at room temperature. The principle of VSM is based on Faraday's law of induction i.e. changing magnetic field produced electric filed.

$$\mathrm{E} = \frac{\mathrm{d\Phi}}{\mathrm{dt}} \ , \qquad (3.8)$$

where E is the magnitude of the induced voltage, Φ is the magnetic flux and $\frac{\mathrm{d\Phi}}{\mathrm{dt}}$ is rate of change of magnetic flux through the coils.

In VSM, a sample is subjected to vibrations nearby a set of pick–up coils under an external magnetic field. The magnetic flux change due to the vibration of a magnetic sample causes an induction voltage across the pickup coil that is proportional to magnetization of the sample. The greater the induced current, greater will be the magnetization of the sample. In other words, the intensity of an induced voltage in the sample is a measure of the magnetization of the sample.

In this study, LakeShore model 7404 vibrating sample magnetometer was used to measure hysteresis loop of all samples. The maximum applied field was kept 1.0 Tesla. From the hysteresis plots the M_s, M_r, H_c and H_a were determined.

3.2.4. Mössbauer Spectroscopy

Mössbauer spectroscopy is a spectroscopic technique based on the Mössbauer effect [200]. Mössbauer spectroscopy gives very precise information about the chemical, structure, magnetic and time dependent properties of a material. In this spectroscopy, a solid sample is exposed to a beam of gamma radiation, and a detector measures the intensity of the beam that is transmitted through the sample and amount of gamma rays are absorbed by the sample. The atoms in the source emitting the gamma rays are the same as the atoms in the sample absorbing them. The nucleus most favorite and amenable to Mössbauer spectroscopy is ^{57}Fe and hence iron containing compounds are widely investigated. The gamma-ray energy can be varied by accelerating the gamma-ray source through a range of velocities with a linear motor. The relative motion between the source and sample results in an energy shift due to the Doppler effect.

In resulting spectra gamma-ray intensity is plotted as a function of the source velocity. At velocities corresponding to the resonant energy levels of the sample, some of the gamma-rays are absorbed, resulting in a drop in the measured intensity and a corresponding dip in the spectrum. The number, positions, and intensities of the dips provide information about the chemical environment of the absorbing nuclei and can be used to characterize the sample. The recorded spectrum is characterized by line shapes, positions, intensities and widths. The most important Mössbauer spectral parameters are the isomer shift, electric quadrupole splitting, hyperfine field and magnetic dipole splitting.

Mössbauer characterizations were performed in the transmission geometry, using a conventional spectrometer in a constant acceleration mode, with the gamma rays provided by a ^{57}Co(Rh) source. The Mössbauer spectrum was analyzed with a non-linear least-square routine, with Lorentzian line shape.

3.2.5. Vector Network Analyzer (VNA)

A vector network analyzer (VNA) is an electronic instrument widely used for high-frequency measurements. VNA is used to measure the frequency dependent electrical properties i.e. permittivity (ε), permeability (μ), reflection loss (R_L) and shielding effectiveness (*SE*) simultaneously from measured *S*-parameters. S-parameters are scattering parameters and described as reflection (S_{11}) and transmission coefficients (S_{21}). Prior to measuring the sample, the VNA and associated cable connections should be calibrated. To check the calibration, an empty sample holder can be measured first. If the test of the empty sample holder showed no losses with a permittivity and permeability of 1, the calibration is completed and the VNA facility is ready for use.

Microwave absorption properties of BaM were evaluated by determination of their reflection and transmission properties with the help of a HP 8720D network analyzer (1 GHz – 20 GHz). For measurement, the prepared BaM pellet was placed into the rectangular waveguide, sample holder, which was lying between two longer waveguides. The reflection coefficient (S_{11}), and the transmission coefficient (S_{21}), were determined over the frequency range 12 to 18 GHz for K_u band.

Chapter 4

RESULTS & DISSCUSSION

Overview

This chapter deals with the experimental results of prepared BaM powders and films. Influence of milling time, sintering temperature, Fe^{3+} ion vacancy and substitution on the magnetic properties of prepared powders and their respective films are studied. Substitution is made by rare earth metal La^{3+} on Ba^{2+} and Co^{2+}-Ti^{4+} on Fe^{3+} site respectively. Preferential site occupation of Fe^{3+} ion with varied mole ratio and Co^{2+} -Ti^{4+} ions at five different crystallographic sites are studied by Mössbauer spectroscopy. La^{3+} substituted barium hexaferrite prepared by two different methods is studied. In first method, La^{3+} substituted BaM is directly prepared by solid state synthesis from Fe_2O_3 and $BaCO_3$ with Fe/Ba molar ratio of 6:1. In the second method, solid state synthesis of Fe_2O_3 and $Ba_{1-x}La_xFe_2O_4$ in molar composition of 5:1 has been adopted. The effect of individual Co^{2+}, Ti^{4+} substitution and simultaneous substitution of Co^{2+}-Ti^{4+} is investigated. Magnetic properties of all the deposited films are measured in parallel and perpendicular directions. Magnetocrystalline anisotropy for all the films are calculated by the law to approach saturation. Finally, microwave property i.e. shielding effectiveness (SE) and reflection losses (R_L) in the frequency range of 12-18 GHz for BaM powders with different mole ratio are studied.

BaM is identified as a potential candidate for high frequency applications. The operating frequency of material is often determined by its FMR frequency, which in turn depends upon the magnetization (M_s), coercivity (H_c) and anisotropic field (H_a). These magnetic properties of materials are directly associated with phase purity, microstructure as well as on nature of ion substitution at Ba or Fe sites. Henceforth, in the present work we investigate the effect of process parameters, Fe/Ba mole ratio and ions substitution on the structural, magnetic and microwave properties of BaM films. This chapter is systematically organized on the following points.

1. Effect of milling time and sintering temperature on structural and magnetic properties of BaM powders and films.

2. Effect of Fe/Ba mole ratio on structural and magnetic properties of BaM powders and films.

3. Effect of La^{3+} substitution on structural and magnetic properties of BaM powders and films.

4. Effect of Co^{2+} and Ti^{4+} substitution on structural and magnetic properties of BaM powders and films.

5. Investigation of microwave properties of BaM powders.

4.1. Preparation of single phase BaM powder

BaM powder is prepared by solid state synthesis method at different calcination temperature. As-mixed powders are calcined between 1000 °C - 1200 °C. **Fig. 4.1** shows the representative XRD patterns of BaM powders calcined at different temperatures. Samples calcined at 1000 °C and 1100 °C shows minor peak of residual Fe_2O_3. Single phase BaM is obtained at 1200 °C without any impurity phase.

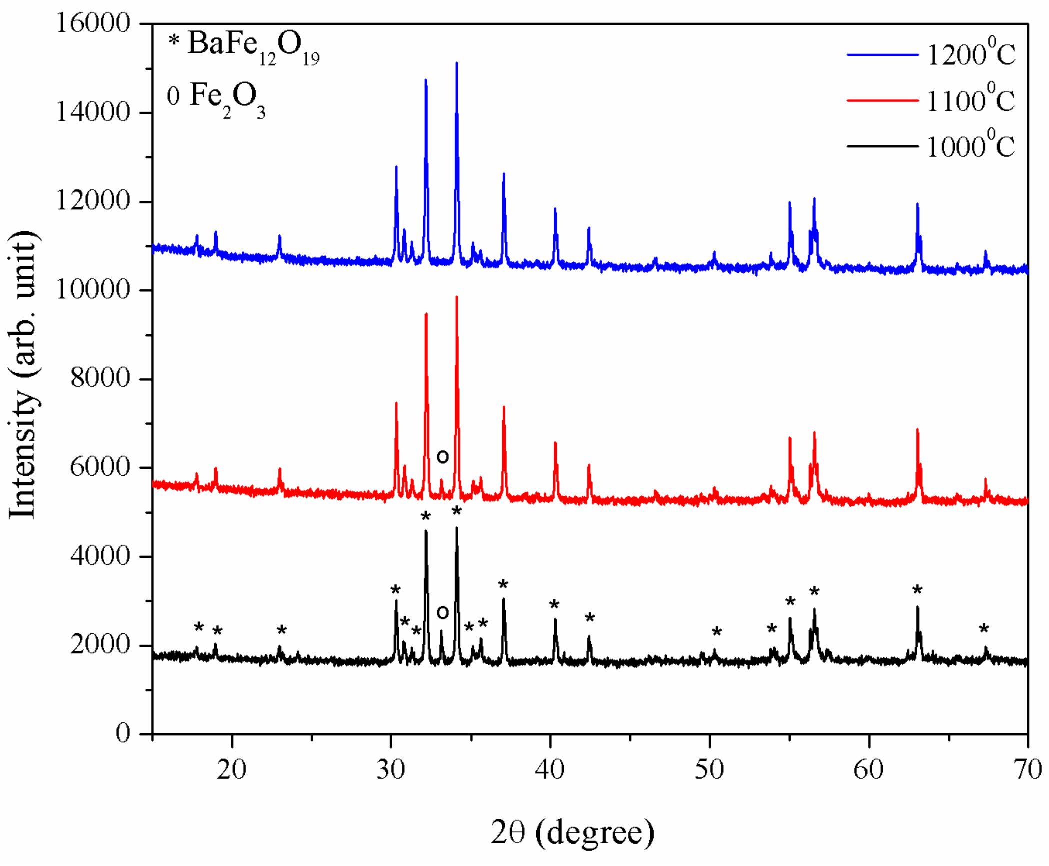

Fig. 4.1. XRD patterns for BaM powders calcined at 1000°C - 1200°C for 3 hours.

4.2. Effect of milling time

BaM powder has been prepared by conventional solid state reaction method. To induce particle size variation, calcined pellets were crushed and wet milled for 1, 2, 3, 4, and 8 hours, in a planetary ball mill using tungsten carbide milling media. The ball-to-charge ratio was kept constant i.e. 10:1 for all the sample.

4.2.1. XRD analysis

Fig. 4.2 shows the XRD patterns of BaM powder, milled for 1, 2, 3, 4 and 8 hours respectively. All XRD patterns are refined by Rietveld refinement using fullprof software with hexagonal symmetry (space group $P6_3/mmc$). The values of *R*-parameters suggest that refinement is best fitted. Refined patterns confirm the single phase of BaM. However, a minor peak of tungsten carbide (WC) is also detected in 4 and 8 hour milled powders. The presence of WC as impurity phase in BaM is due the wear of WC milling media. The intensity of WC found to increase with milling time. Lattice parameters $a = b = 5.89$ Å and $c = 23.21$ Å are nearly constant for all the samples. The average crystallite size (*C.S*) and fitted parameters (R_p, R_{wp} R_{exp} and χ^2) as obtained from refinement are listed in **Table 4.1.** The average *C.S.* is found to decrease from 90 nm to 67 nm with increasing milling time from 1 hour to 8 hour respectively.

Table 4.1. Crystallite size and *R*-factors of BaM powders as a function of milling time.

Milling time (hour)	***C.S.* (nm)**	***R*-factors**			χ^2
		R_p	R_w	R_{exp}	
1	90.03	2.69	3.39	3.13	1.08
2	85.18	2.70	3.41	3.13	1.18
3	76.07	2.65	3.36	3.12	1.18
4	74.12	3.33	3.65	3.16	1.33
8	67.42	2.83	4.64	3.18	2.13

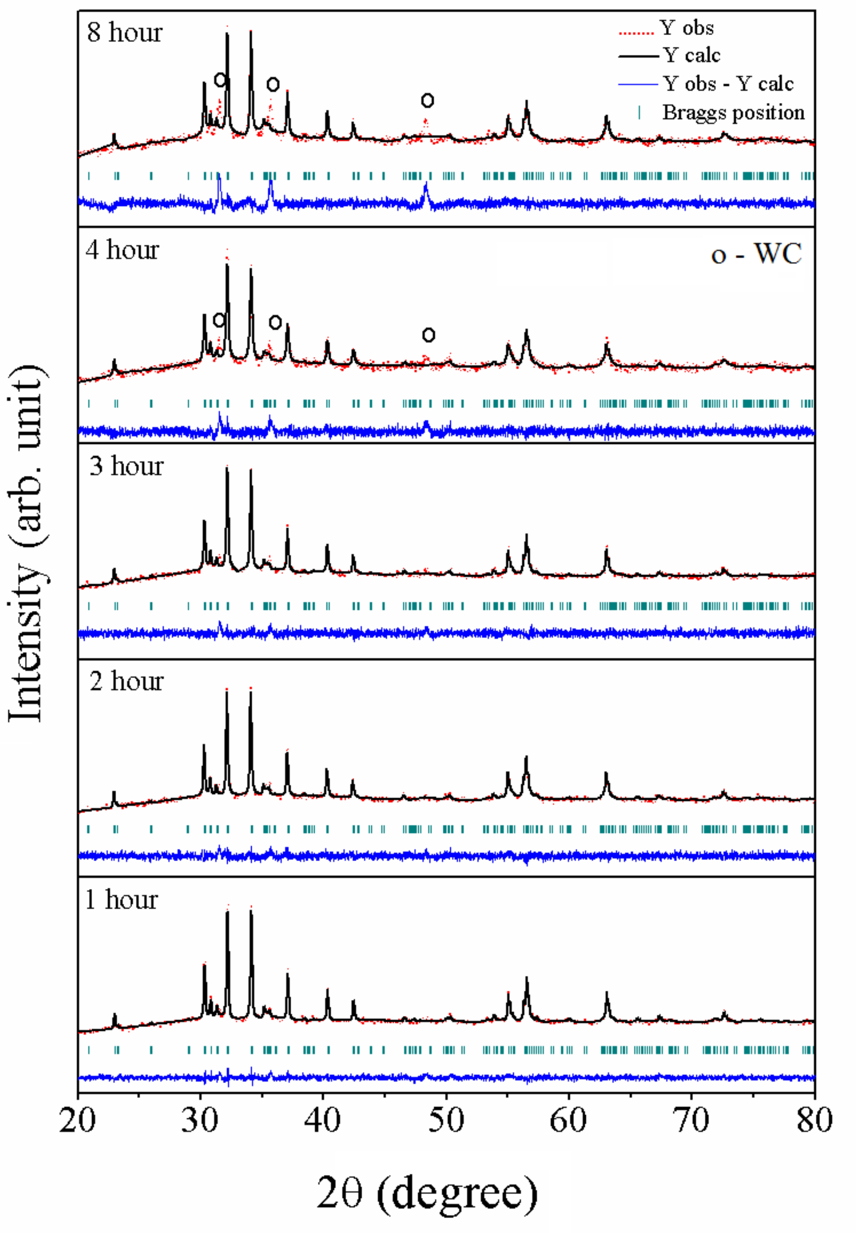

Fig. 4.2. X-ray diffraction patterns of BaM powders milled different hours.

4.2.2. Particle size measurement

Fig. 4.3 shows the SEM micrographs of the BaM powders milled for 1, 2, 3, 4 and 8 hours. It is clear that powder milled for 1 hour shows discrete particle, however with increasing milling agglomeration in the powder is observed. The inset included in 1 hour and 4 hour milled powder micrographs reveal the hexagonal shape of the powder. The particle size is measured by Axio-vision software measuring atleast 100 particles.

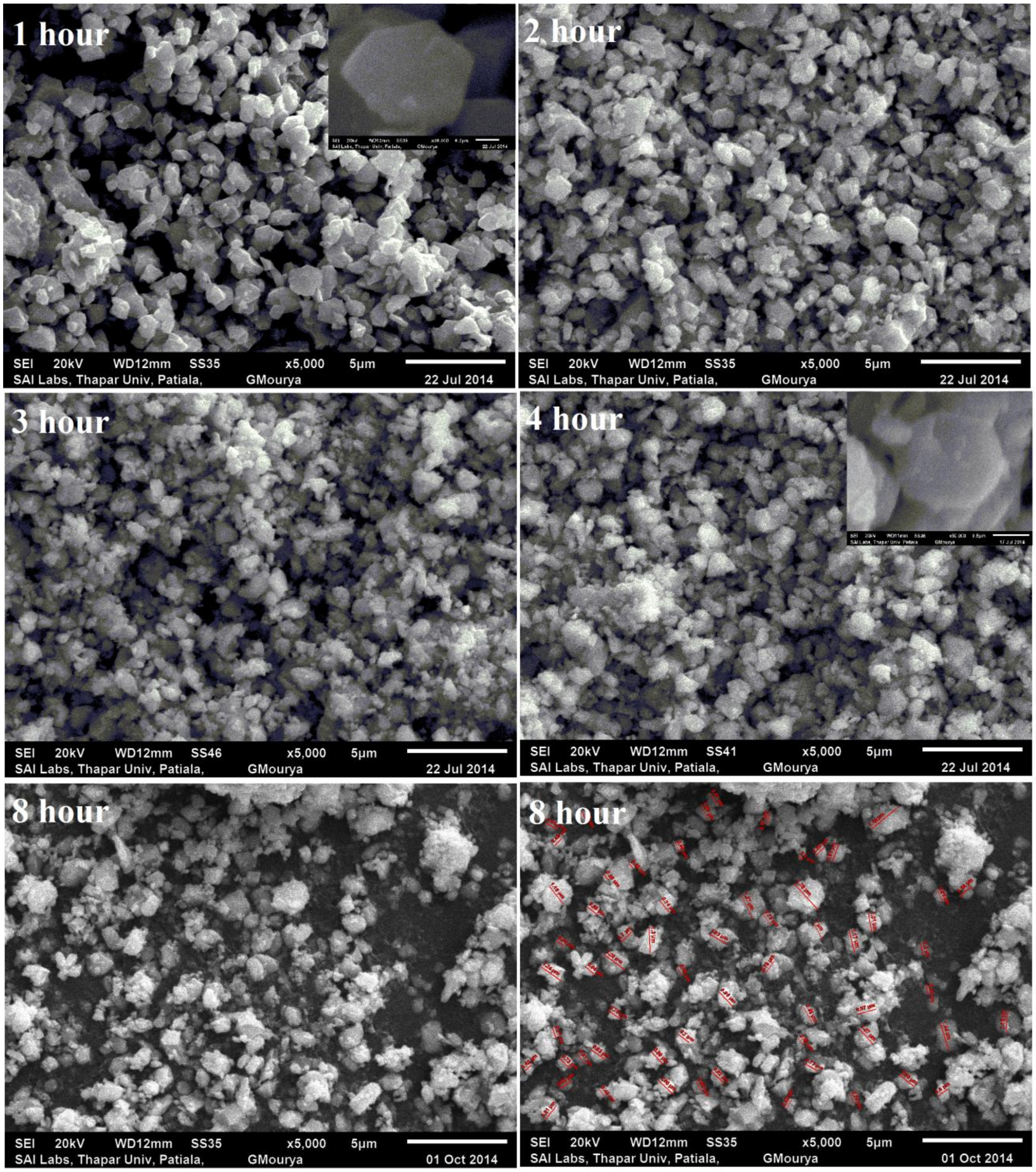

Fig. 4.3. The SEM micrographs of BaM powders milled for 1, 2, 3, 4, and 8 hours. Representative micrographs milled for 8 hour showing 8 hour particle size measurement.

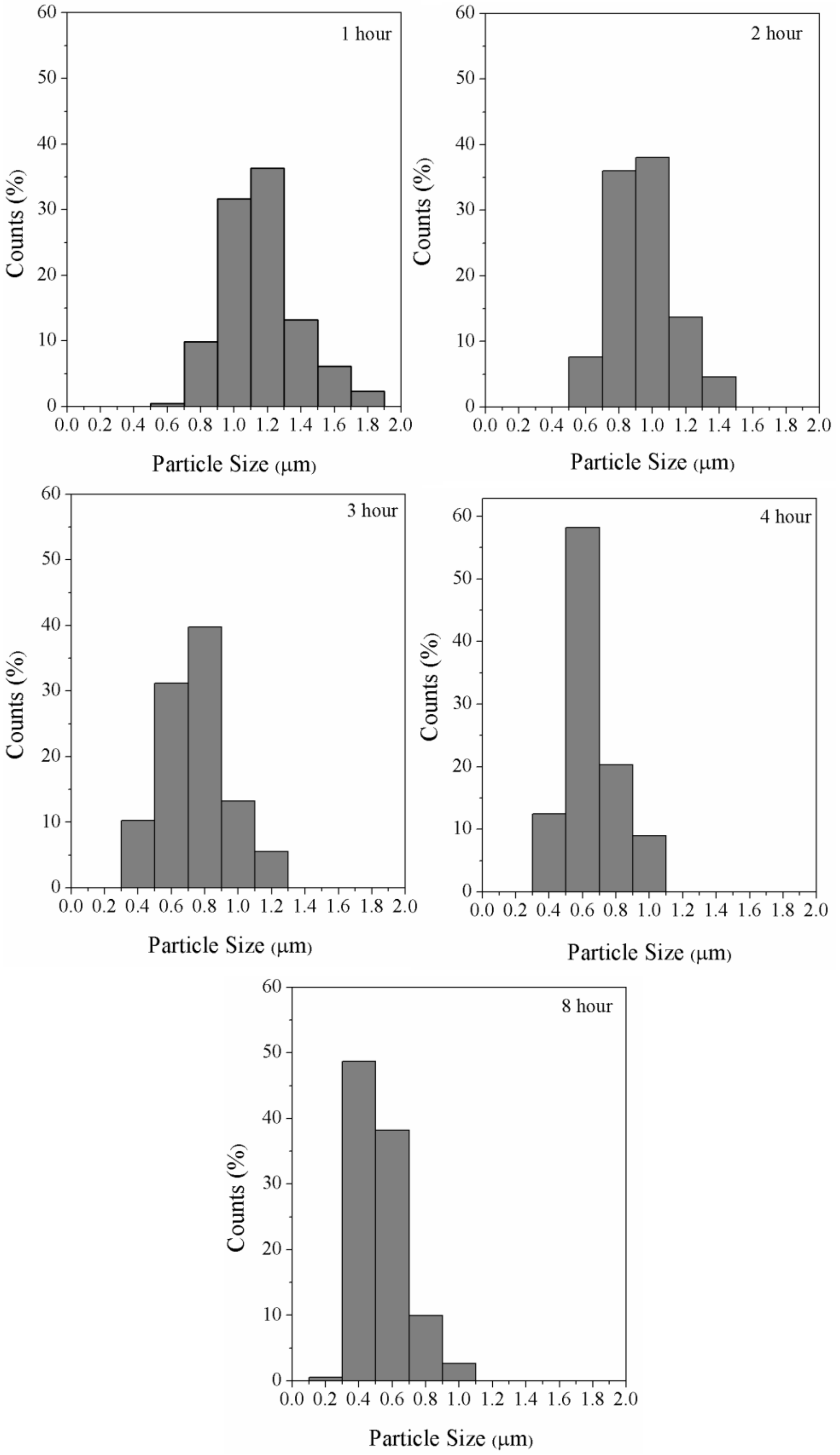

Fig. 4.4. Particle size distribution measured by SEM.

Fig. 4.4 shows the particle size distribution of BaM powder milled for different hours. The x-y axis is kept constant for all histograms for visual comparison. It is clearly visible that particle diameters are in the range of 0.7 – 1.4 μm for 1 hour milled powder. The average particle size is 1.06 ± 0.20 μm. While for 8 hour milled powder, particle diameters are lying in range of 0.3 – 0.7 μm. It is observed that the particle size distribution is narrowing and continuously shifting towards the lower particle size with milling time [201]. The variation in the average particle size with milling time graphically depicted in the **Fig. 4.5.**

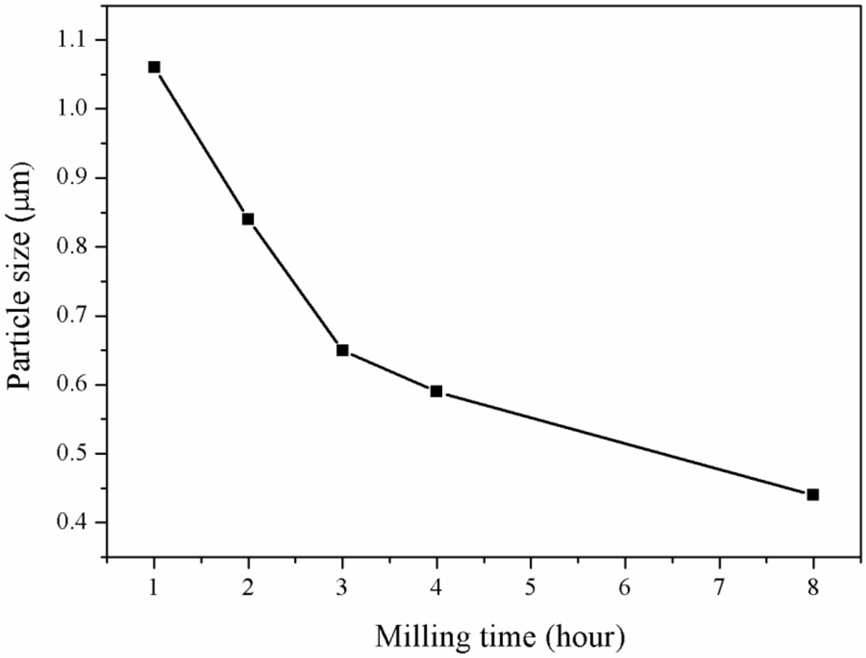

Fig. 4.5. Variation of particle size with milling time.

4.2.3. Magnetic measurement

Fig. 4.6 illustrates the *M-H* loop of BaM powders milled for 1, 3 and 8 hours. The *M* is found to decrease with increase in milling time. However no remarkable change in H_c is observed. The decrease in *M* is directly associated with the presence of non magnetic phase of WC. As explained earlier, the content of WC increases with milling time, hence *M* decreases. The magnetic properties of the powders are listed in **Table 4.2**.

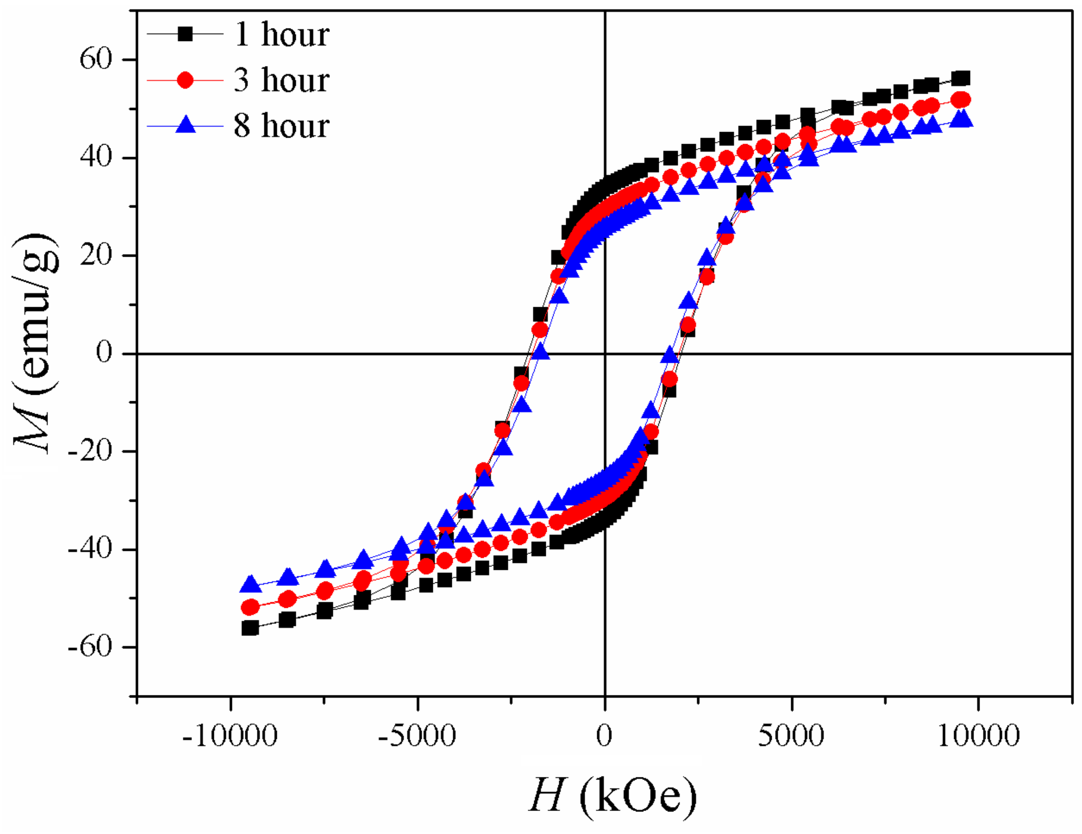

Fig. 4.6. Hysteresis loop of BaM powders milled for different time.

Table 4.2. Magnetic properties of BaM powder milled for different milling time.

Milling time (hour)	***M* (emu/g)**	**M_r (emu/g)**	**H_c (kOe)**
1	56.12	33.62	2.01
2	56.04	33.18	1.95
3	51.91	29.44	1.92
4	48.47	27.61	1.84
8	47.63	25.73	1.73

4.2.4. Preparation of BaM films

It is observed that BaM powder calcined at 1200 °C shows the single BaM phase without any residual Fe_2O_3. Higher milling time of the powders shows adverse effect on the magnetic properties due to the presence of WC phase. Therefore, one hour milled powder calcined at 1200 °C is chosen for the preparation of BaM thick films.

Fig. 4.7 shows the XRD pattern of the screen printed BaM films sintered at 1300 °C. XRD pattern shows peaks corresponding to Al_2O_3 substrate and BaM phase. No other impurity phase is observed.

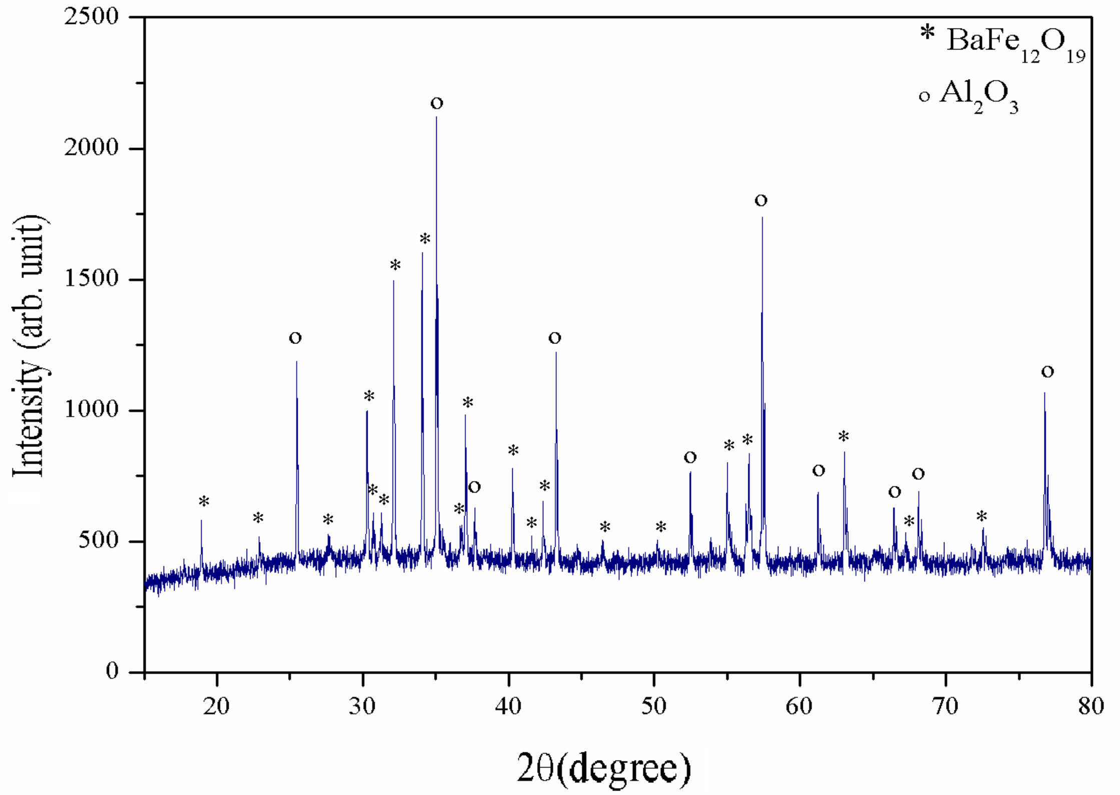

Fig. 4.7. XRD pattern of BaM film sintered at 1300 °C.

4.2.5. Surface morphology

Fig. 4.8 shows the SEM micrographs of the films sintered at 1200 °C, 1250 °C, 1300 °C and 1350 °C. The grain size is increases with sintering temperature from 1200 °C - 1300

°C. The film sintered at higher temperature shows dense microstructure with low porosity. However, SEM micrographs of the film sintered at 1350 °C shows the molten characteristics. During sintering, the observed microstructural changes are porosity reduction and grain growth. However, thick film sintered at 1300 °C shows fractional porosity and microstructure is not uniformly dense. Further to improve the microstructural features, pressure of 0.5 kg/cm^3 is applied on BaM film by hydraulic press, prior to sintering.

Fig. 4.9 (a) shows the effect of the pressure on the surface morphology of BaM thick film sintered at 1300 °C. It is clear that slight pressure improves the densification and reduces the porosity fraction. Micrographs also illustrate the co-existence of equiaxed and elongated grains. **Fig. 4.9 (b)** shows sharp interface between the film and substrate, suggesting no inter diffusion is between the films and substrate during sintering.

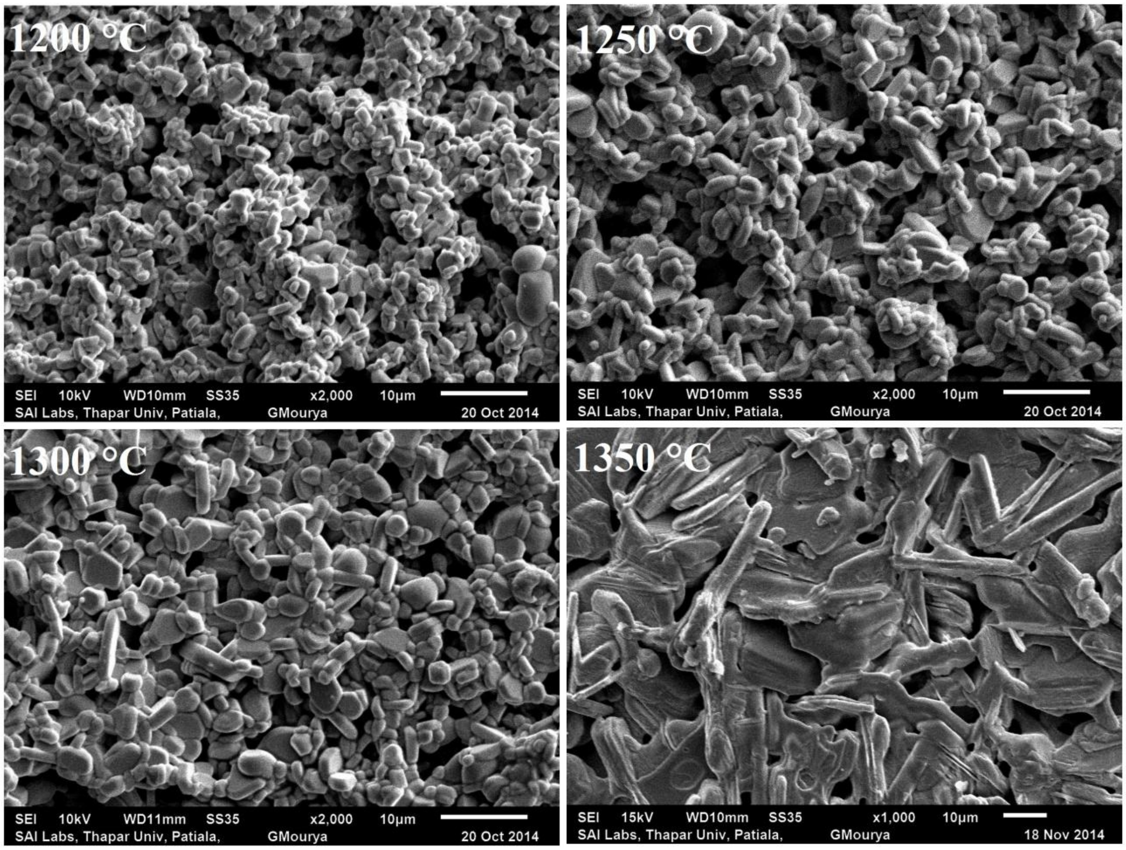

Fig. 4.8. SEM micrographs of BaM thick film sintered at 1200 °C - 1350 °C.

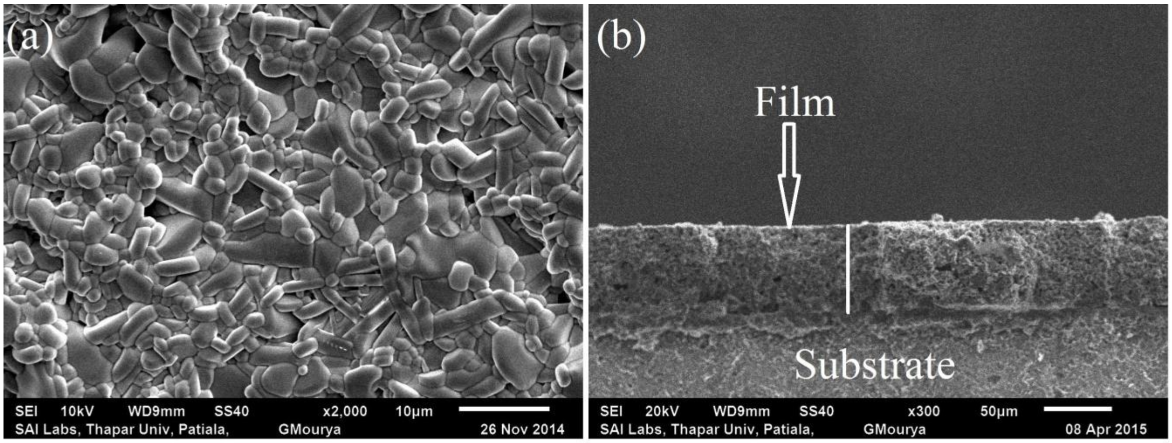

Fig. 4.9. (a) Effect of the pressure on the surface morphology of BaM thick film sintered at 1300 °C **(b)** Cross section view of BaM film.

4.2.6. Magnetic measurement

Fig. 4.10 shows *M-H* loops for BaM films, parallel (||) and perpendicular (⊥) direction to the applied magnetic field. It is evident that *M* and M_r are higher in || direction as compared to ⊥ direction, suggesting in plane anisotropy in the films. *M* of films is relatively lower than powder sample. It is due to addition of nonmagnetic Bi_2O_3 phase. Bi_2O_3 or glass frit is required for better adhesion between substrate and films. Without addition of these phases, film chip-out from the substrate. Magnetic properties of BaM film in parallel (||) and perpendicular (⊥) direction to the applied magnetic field are listed in **Table 4.3.**

Table 4.3. Magnetic properties of BaM film in parallel and perpendicular direction to the applied magnetic field.

Direction	M_s **(emu/g)**	M_r **(emu/g)**	H_c **(kOe)**
parallel (||)	52.62	25.89	1.31
perpendicular (⊥)	46.64	14.42	1.32

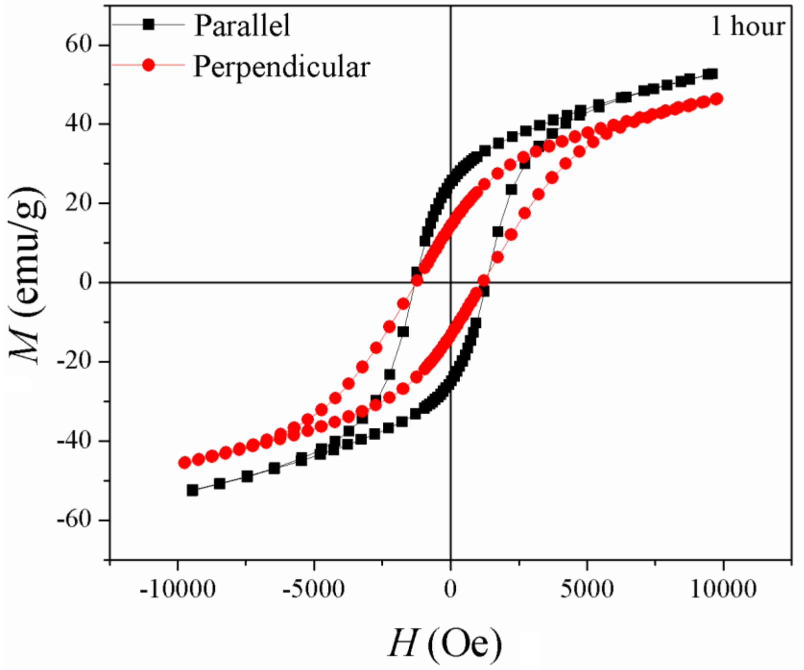

Fig. 4.10. *M*-*H* loop in parallel (||) and perpendicular (⊥) direction for BaM film.

4.3. Effect of Fe/Ba mole ratio

4.3.1. XRD analysis

Fig. 4.11 shows the XRD patterns of calcined BaM powders with different Fe/Ba mole ratios. All XRD patterns are refined using P6_3/mmc space group. Single phase BaM is obtained in the samples with mole ratio of 5.5 - 6.0. However, a minor peak of orthorhombic barium monoferrite ($BaFe_2O_4$) is also detected for lower mole ratios. The estimated volume percent of $BaFe_2O_4$ phase is below 0.25. The lattice parameters (a and c) and R-factors (R_p, R_w, R_{exp} and χ^2), as obtained from refinement are given in **Table 4.4**. R-factor values suggest that refinements are best fitted. Lattice constant 'a' and 'c' are nearly constant for all the samples. The average crystallite size (*C.S.*) of prepared hexaferrite powders are ~90 nm. The refined atomic positions for the x = 5.0 and x = 6.0 are shown in **Table 4.5**. The difference in atomic position parameters values are due to vacant Fe^{3+} ion sites.

Table 4.4. Lattice parameters, R-factor, volume of unit cell and phase percentage of Ba.Ox(Fe_2O_3) powders.

x	**Lattice parameters**		***R*-factors**				**Vol**	**Phase (%)**	
	***a* (Å)**	***c* (Å)**	R_p	R_w	R_{exp}	χ^2	**(Å)^3**	$BaFe_{12}O_{19}$	$BaFe_2O_4$
5.0	5.899(7)	23.231(3)	3.95	5.00	4.62	1.17	700.31	99.76	0.24
5.25	5.898(6)	23.220(3)	3.95	4.97	4.58	1.18	699.33	99.83	0.17
5.5	5.899(7)	23.230(3)	3.68	4.62	4.37	1.12	700.11	100	0
5.75	5.900(4)	23.236(2)	3.84	4.83	4.53	1.14	700.49	100	0
6.0	5.901(4)	23.239(2)	3.26	4.12	3.90	1.11	700.59	100	0

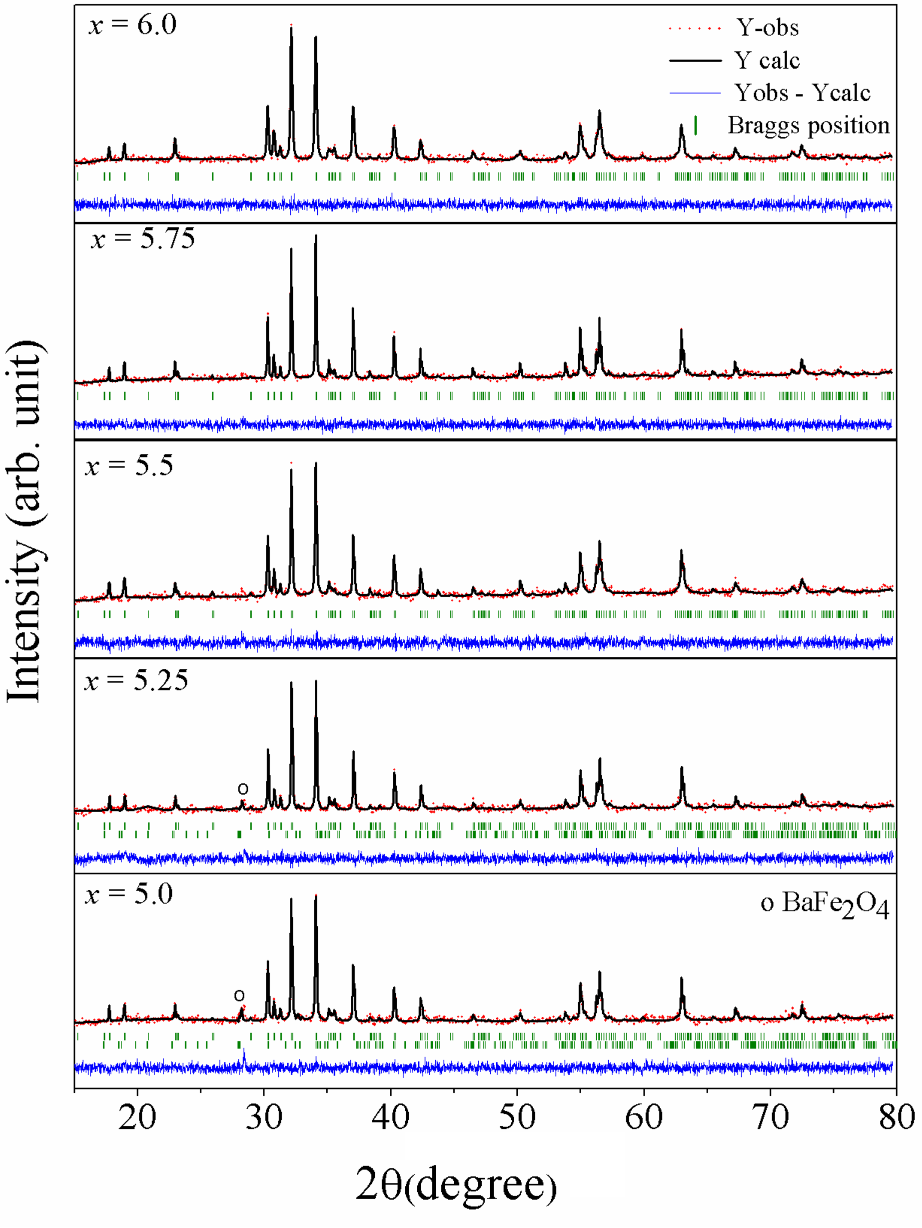

Fig. 4.11. Refined XRD patterns of BaO.x(Fe_2O_3) powders.

Table 4.5. Atomic positions for BaO.*x*(Fe_2O_3), *x* = 5.0 and *x* = 6.0 samples, as obtained from the Rietveld analysis.

Atoms	**Site**	**BaO.5(Fe_2O_3)**			**BaO.6(Fe_2O_3)**		
		x	***y***	***z***	***x***	***y***	***z***
Ba	2*d*	0.6666	0.3333	0.2500	0.6666	0.3333	0.2500
Fe1	2*a*	0	0	0	0	0	0
Fe2	2*b*	0	0	0.2641(2)	0	0	0.246(4)
Fe3	4f_1	0.3333	0.6666	0.0237(1)	0.3333	0.6666	0.028(8)
Fe4	4f_2	0.3333	0.6666	0.1901(4)	0.3333	0.6666	0.1912(5)
Fe5	12*k*	0.1670(2)	0.3339(3)	0.8917(3)	0.1675(3)	0.3350(2)	0.8915(4)
O1	4*e*	0	0	0.1497(2)	0	0	0.150(12)
O2	4*f*	0.3333	0.6666	0.9470(4)	0.3333	0.6666	0.9443(16)
O3	6*h*	0.1821(4)	0.3129(1)	0.2501	0.1817(2)	0.3411(3)	0.250
O4	12*k*	0.1568(7)	0.3129(1)	0.0520(3)	0.1590(1)	0.3138(4)	0.0516
O5	12*k*	0.5106(1)	0.0043(4)	0.1533(5)	0.5026(5)	0.0043(1)	0.1469(10)

4.3.2. Mössbauer analysis

Fig. 4.12 shows the *R-T* Mössbauer spectra for different Fe/Ba mole ratio. Mössbauer spectra are fitted for five discrete sextets. Each sextets corresponding to one of the five different crystallographic Fe sites i.e. 12*k*, 4f_1, 4f_2, 2*a* and 2*b* respectively. No component for residual $BaFe_2O_4$ is considered due to its negligible volume fraction. The obtained fitted parameters, hyperfine field (B_{hf}), quadrupolar shift (*QS*), isomer shift (δ) and the line width (Γ) are given in **Table 4.6**. The fitted Mössbauer parameters are in good agreement with the previously reported data for BaM [202].

The number of Fe vacancy (N_{Fe}) and vacancy fraction (F_{v}) on the i^{th} site can be estimated from respective relative areas by using the formula [202]

$$N_{\mathrm{Fe}}(i) = C_{\mathrm{Fe}}\left[\frac{S(i)}{\sum_{i=1}^{5} S(i)}\right], \tag{4.1}$$

$$F_{\text{v}} = \frac{N(i) - N_{Fe}(i)}{N(i)} \times 100\%\,, \tag{4.2}$$

where C_{Fe} denotes the iron content (C_{Fe} = 12-2x), $S(i)$ is the subspectral area of i^{th} site obtained from the least square fit and $N(i)$ is the number of vacancy for i^{th} site.

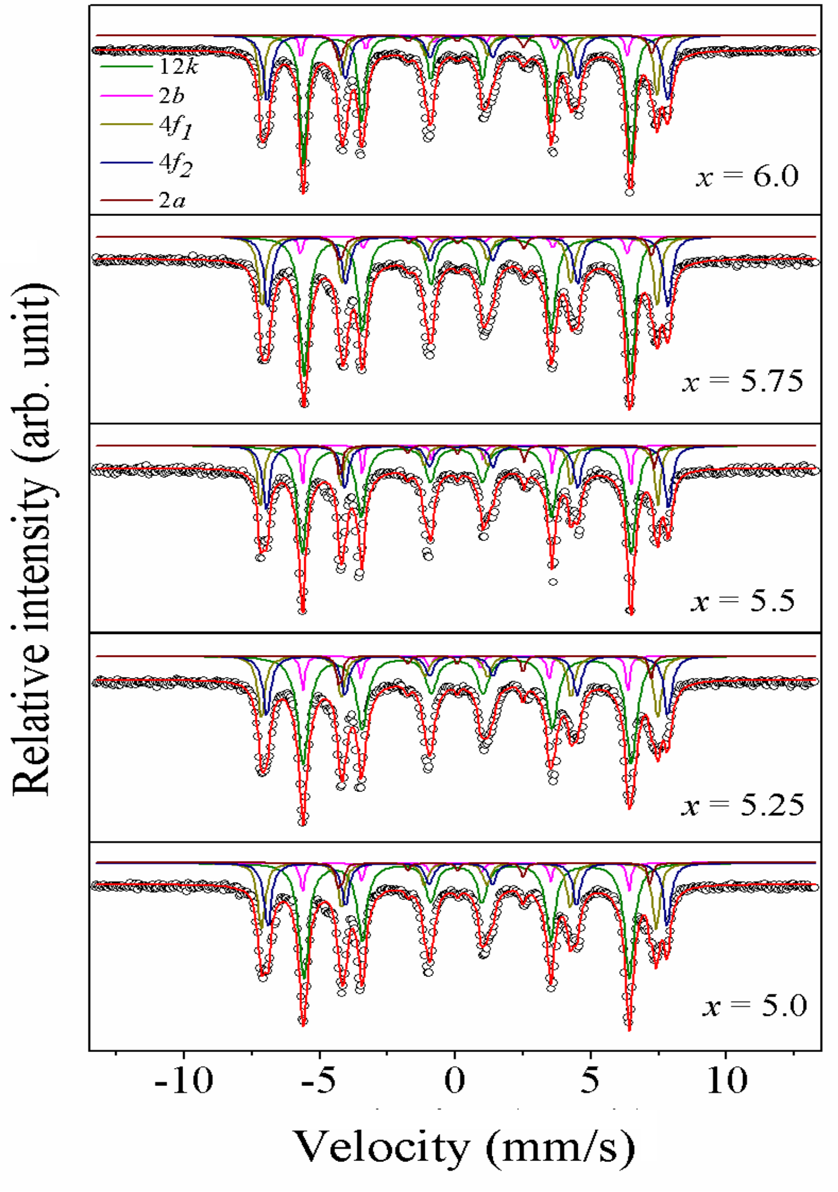

Fig. 4.12. Mössbauer spectra for BaO.xFe$_2$O$_3$.

Table 4.6. Mössbauer parameters of BaO.xFe$_2$O$_3$.

Sites	x	Γ (mm/s)	*IS* (mm/s)	*QS* (mm/s)	B_{hf} (T)	*S* (%)
12*k*	5.0	0.373	0.248	0.405	41.000	50.5
	5.25	0.401	0.242	0.407	41.034	50.7
	5.5	0.316	0.238	0.399	41.341	50.8
	5.75	0.404	0.242	0.406	41.325	50.4
	6.0	0.362	0.240	0.402	41.216	50.2
4f_1	5.0	0.302	0.159	0.247	48.516	17.3
	5.25	0.423	0.144	0.244	48.745	16.8
	5.5	0.392	0.163	0.244	49.109	16.1
	5.75	0.398	0.157	0.226	48.935	16.5
	6.0	0.382	0.159	0.227	48.756	16.8
2*a*	5.0	0.251	0.325	0.196	51.452	8.2
	5.25	0.264	0.306	0.166	51.501	8.2
	5.5	0.133	0.292	0.278	52.391	8.3
	5.75	0.274	0.272	0.192	51.803	8.2
	6.0	0.207	0.299	0.216	51.763	8.1
4f_2	5.0	0.381	0.232	0.178	50.295	16.7
	5.25	0.309	0.217	0.194	50.316	16.4
	5.5	0.245	0.269	0.182	51.168	16.2
	5.75	0.330	0.248	0.156	50.876	16.5
	6.0	0.302	0.255	0.179	50.483	16.7
2*b*	5.0	0.281	0.220	2.255	40.183	7.3
	5.25	0.271	0.213	2.282	40.283	7.9
	5.5	0.294	0.218	2.308	40.772	8.6
	5.75	0.288	0.211	2.343	40.562	8.4
	6.0	0.301	0.207	2.330	40.387	8.2

The number of iron site vacancy $N_{Fe}(i)$ and relative vacancy fraction $F_v(i)$ of Fe on the five sites are shown in **Fig. 4.13 (a)** and **(b)** respectively. It is clear that F_v is more at 4f_1 and 4f_2 sites for Fe/Ba mole ratio of 5.5. Further decreasing the mole ratio, F_v is apparently higher for 2*b* site which suggest that 2*b* site has more Fe ion vacancy as compared to other sites. The variation of B_{hf} for each site first increased and then decreased as Fe/Ba mole ratio varies from 5.0 - 6.0 [**Table 4.6**]. The B_{hf} is found to higher for Fe/Ba mole ratio of 5.5. No variation in δ and *QS* is observed.

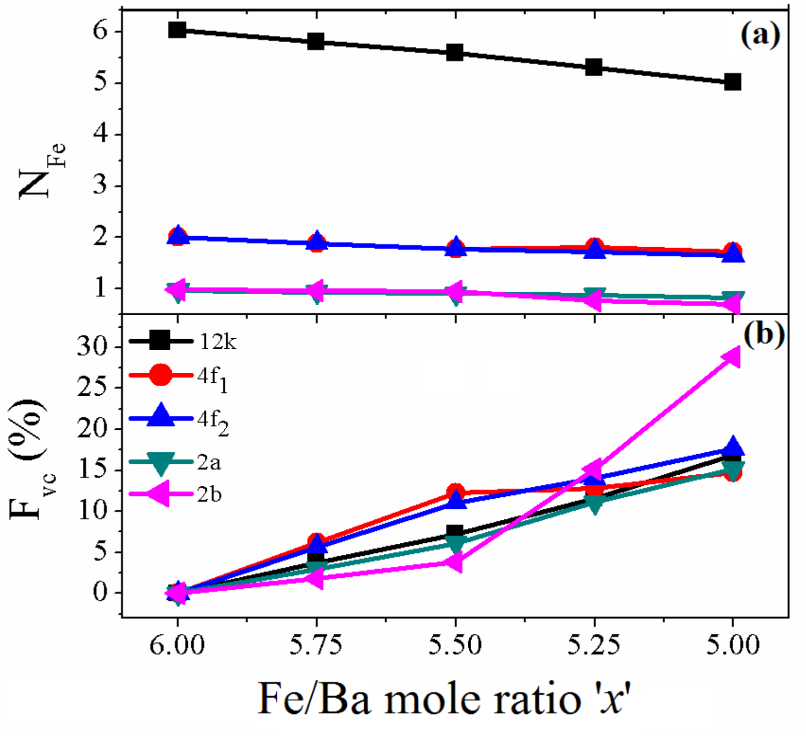

Fig. 4.13. (a) Site occupation number for Fe (N_{Fe}) and **(b)** site vacancy fraction F_v, as obtained from mössbauer fitting for BaO.xFe$_2$O$_3$.

4.3.3. Magnetic measurement

The ferromagnetic hysteresis (*M-H*) loops for BaM powders are shown in **Fig. 4.14**. and **Fig. 4.15** shows the *M-H* loop for films measured in parallel direction only, because not much change in magnetic properties is observed in parallel (||) and perpendicular (⊥)

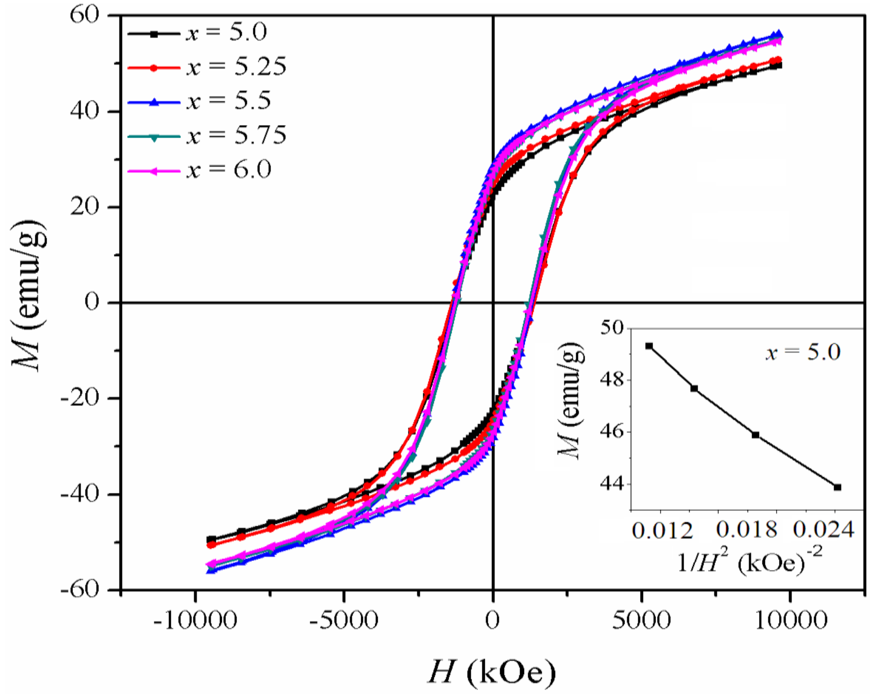

Fig. 4.14. *M-H* loop for BaO.*x*Fe_2O_3 powders. Inset shows the dependence of *M* on 1/H^2 for *x* = 5.0.

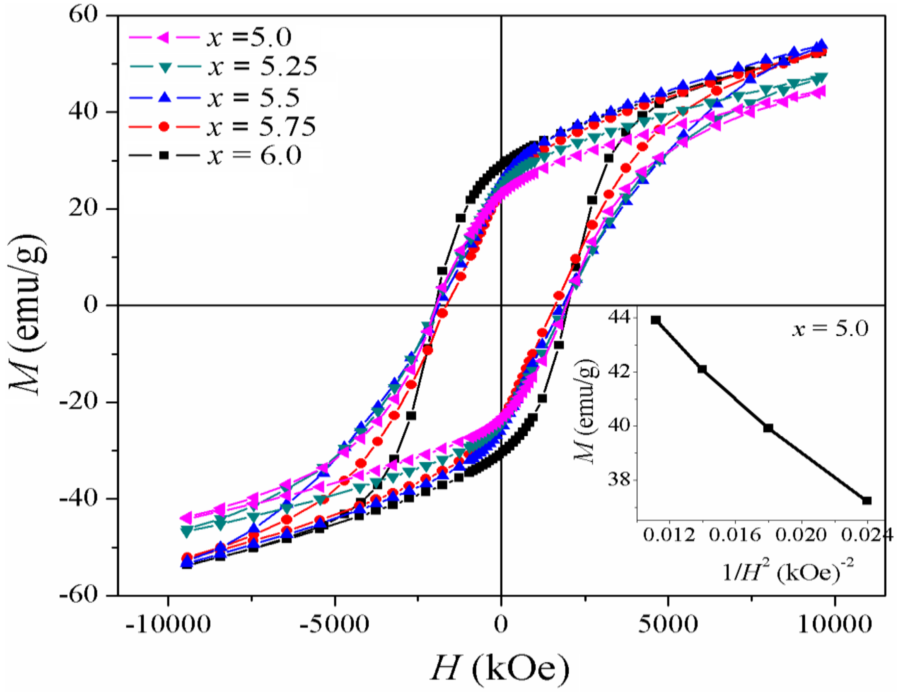

Fig. 4.15. *M-H* loop spectra for BaO.*x*Fe_2O_3 films. Inset shows the dependence of *M* on 1/H^2 for *x* = 5.0.

direction. The samples show the behaviour of hard magnetic materials with high H_c and large M. The variations of magnetic properties of powders and films with Fe/Ba mole ratio are given in **Table 4.7**. M is found to increase with decreasing Fe/Ba mole ratio, and is maximum for 5.5 mole ratio. The higher M is attributed due to the larger vacant fraction of Fe ions at spin down sites ($4f_1$ and $4f_2$), which is also evident from estimated F_v from the mössbauer measurements. Further decreasing the mole ratio, M decreases due to larger F_v at spin up site ($2b$). Larger hyperfine field for 5.5 mole ratio sample also supports the higher magnetization in the powder and films. It is noted that H_c has no measurable variation among the studied samples. H_c primarily depends upon the grain size and H_a. The similar microstructural features imply the invariable H_c for all the films [**Fig. 4.16**].

The H_a field of the magnetic materials was deduced from the law of approach to saturation [203]:

$$M(H) = M_s\left(1 - \frac{A}{H} - \frac{B}{H^2}\right) + \chi_p H \qquad (4.3)$$

where, H is applied field, χ_p is field associated with the induced increase in the spontaneous magnetization of domains. A is the inhomogeneity parameter and the term A/H is related to the existence of inhomogeneities in the microcrystals. The B/H^2 gives the magnetocrystalline anisotropy contribution. A plot of M vs $1/H^2$ in the field region 6 kOe < H < 10 kOe for each sample gave a straight line, indicates that the terms A and χ_p terms are negligible [204]. The slope of straight line (B) was used to determine H_a. B can be expressed as

$$B = \frac{1}{15} H_a^2 \qquad (4.4)$$

The first anisotropy constant was evaluating from relation:

$$H_a = \frac{2K_1}{M_s} \qquad (4.5)$$

Inset in **Fig. 4.14** and **4.15** shows the dependence of M on $1/H^2$ for powders and films respectively. The calculated values of H_a and K_1 are listed in **Table 4.7** and found that H_a and K_1 first increases and then decrease with mole ratio. H_a is an intrinsic property and does not depend upon the grain size and shape. Therefore, the variation in H_a is arising due to different Fe ion occupancy with mole ratio as is evident from **Fig. 4.14**. The H_a for single crystal BaM is ~ 17 kOe, the low H_a value is due to the polycrystalline nature and random crystal orientation of the films. Hence we conclude that site occupancy of Fe ion plays a key role in H_a variation.

Table 4.7. Magnetic properties of BaM powder and films for different mole ratios.

x	M (emu/g)		M_r (emu/g)		H_a (kOe)		$K_1 \times 10^6$ (erg/cm^3)	
	Powder	**Film**	**Powder**	**Film**	**Powder**	**Film**	**Powder**	**Film**
5.0	49.63	44.42	22.40	23.22	9.31	9.25	1.22	1.41
5.25	50.84	47.46	24.99	24.66	9.40	9.36	1.26	1.49
5.5	56.09	53.91	28.48	25.56	9.75	10.33	1.45	1.53
5.75	55.06	52.55	26.41	23.82	9.61	10.22	1.40	1.49
6.0	54.66	52.28	27.05	29.83	9.55	9.74	1.38	1.41

4.3.4. Surface morphology of films

Fig 4.16 (a - c) shows the surface morphology of sintered BaM films for Fe/Ba mole ratio of 5.0 and 6.0. All films have dense microstructure with limited porosity. No variation in microstructure with mole ratio is observed. The microstructure consisted of elongated and equiaxed grains with well separated grains boundaries. The random orientation of the grains suggests the isotropic nature of the films. Few hexagonal shaped grains are also observed. The average grain size of the films is 2-3 μm. However, the elongated grains show an aspect ratio of ~ 3. **Fig. 4.16 (d)** shows the cross sectional image of the BaM thick film sintered at 1300°C. The initial thickness of the BaM film was kept constant to ~ 75 μm. The measured final thickness of the film is ~ 67 μm and remains uniform throughout the cross section. The reduced thickness is the effect of shrinkage during the sintering, which leads densification of the films [205]. The sharp interface between the film and substrate suggest no inter diffusion.

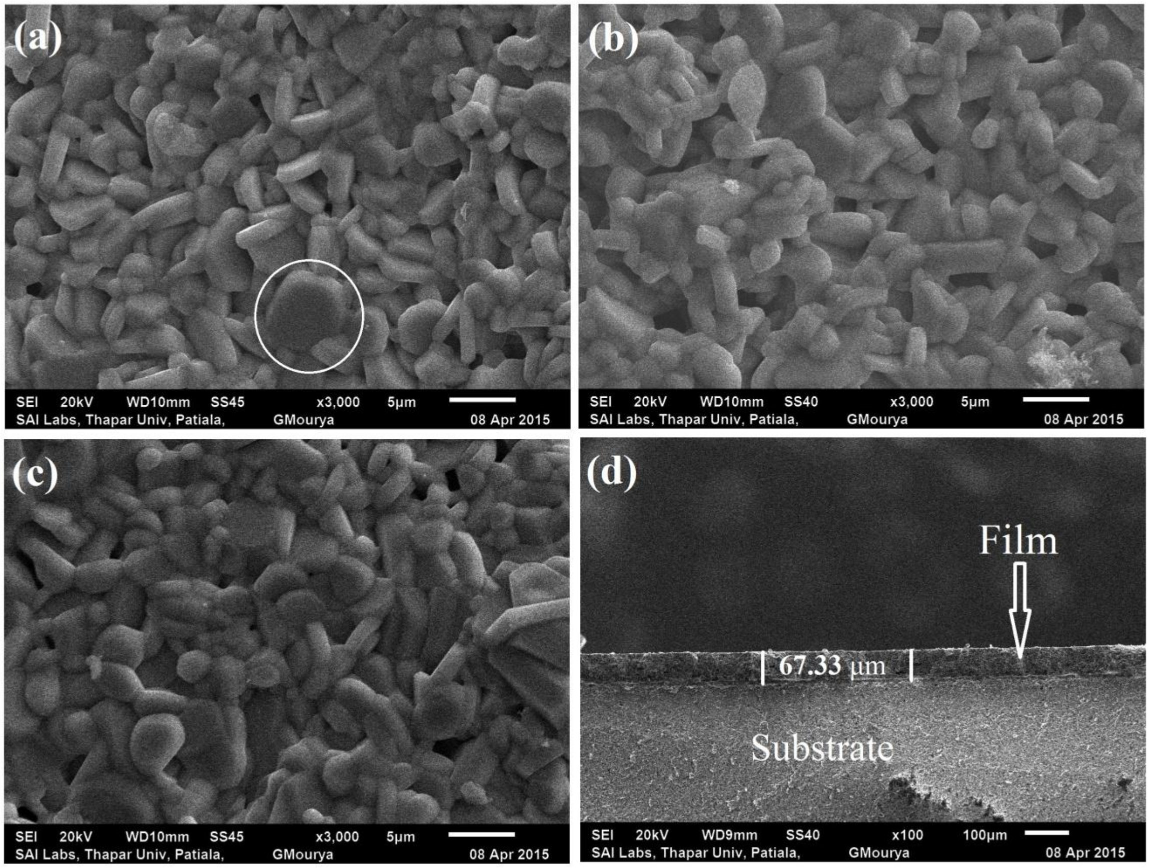

Fig. 4.16. Surface morphology for BaO.xFe$_2$O$_3$ films of **(a)** $x = 5.0$ **(b)** $x = 5.5$ and **(c)** $x = 6.0$. Circle in fig. 4.16 (a) shows the hexagonal shape of the particles. **(d)** Cross section view of BaM thick film.

4.4. Effect of La substitution

$Ba_{1-x}La_xFe_{12}O_{19}$ (x = 0.0 - 0.2) has been prepared by solid state synthesis, adopting two different substitution methods. In first method (M-I), $Ba_{1-x}La_xFe_{12}O_{19}$ is directly prepared by mixing $BaCO_3$, Fe_2O_3 with La_2O_3 in planetary ball mill. In the second method (M-II), first $Ba_{1-x}La_xFe_2O_4$ is prepared by solid state synthesis of equimolar composition of $BaCO_3$ and Fe_2O_3 with La_2O_3. As-mixed powders were calcined at 1000 °C for 2 hour. Further, as-prepared powder of $Ba_{1-x}La_xFe_2O_4$ and Fe_2O_3 were mixed in 1:5 molar compositions in ball mill for 3 hours followed by calcination.

4.4.1. XRD analysis

Fig. 4.17 shows the refined XRD pattern of $Ba_{1-x}La_xFe_2O_4$ (x = 0.0 - 0.2) prepared at 1000 °C for 2 hour. The patterns are refined with orthorhombic symmetry with space group $Bb2_1m$ [206]. Samples shows single phase of $BaFe_2O_4$ for x = 0.0; however a secondary phase of $LaFeO_3$ was also detected for x = 0.1 and 0.2. The percentage of secondary phase increases with increasing La substitution. The refined lattice parameters and Bragg R- factors for all the $Ba_{1-x}La_xFe_2O_4$ samples are listed in **Table 4.8**.

Table 4.8. Lattice parameters, *R*- factors and phase percentage for $Ba_{1-x}La_xFe_2O_4$.

x	Lattice parameters			*R*-factors				Phase (%)	
	a(Å)	*b*(Å)	*c*(Å)	R_p	R_{wp}	R_{exp}	Ψ^2	$BaFe_{12}O_{19}$	Fe_2O_3
0.0	19.040(2)	5.381(2)	8.444(4)	5.03	6.35	5.71	1.23	100	0
0.1	19.039(8)	5.382(3)	8.445(4)	5.61	7.2	5.76	1.56	90.72	9.28
0.2	19.037(9)	5.383(3)	8.445(4)	5.82	7.5	5.82	1.66	83.18	16.82

The representative X-ray diffraction patterns for La substituted $BaFe_{12}O_{19}$ prepared by M-I and M-II methods at 1250 °C are shown in **Fig. 4.18 and 4.19** respectively. XRD patterns are refined with hexagonal symmetry (space group $P6_3/mmc$). Fitting parameters R_p, R_{wp} and R_{exp} for all the samples are below 4.5 and Ψ^2 is ≈ 1.5, which suggests that the refinement of all the samples is best fitted. Single phase $BaFe_{12}O_{19}$ is found for all the samples. However, a small trace of residual α-Fe_2O_3, (< 0.50%) is observed for substituted samples. Lattice parameters show shrinkage along c-axis, due to higher ionic radii of Ba^{2+} (0.135nm) as compared with the La^{3+} (0.106nm). Further increase in La substitution to, $x = 0.2$ a slight increase in 'c' is observed. The higher substitution amount of La^{3+} converts Fe^{3+} ion into Fe^{2+} ion, which may also increase the lattice parameters due to larger ionic radius of Fe^{2+} (0.080 nm) than that of Fe^{3+} (0.067nm). Refined parameters and phase composition of $Ba_{1-x}La_xFe_{12}O_{19}$ as obtained from refinement is listed in **Table 4.9.** The refined atomic positions values for $x = 0.0$ and $x = 0.2$ samples prepared from M-I and M-II methods are given in **Table 4.10** and **4.11** respectively. The difference in atomic positions is due to smaller ionic radii of La^{3+} as compared to Ba^{2+}.

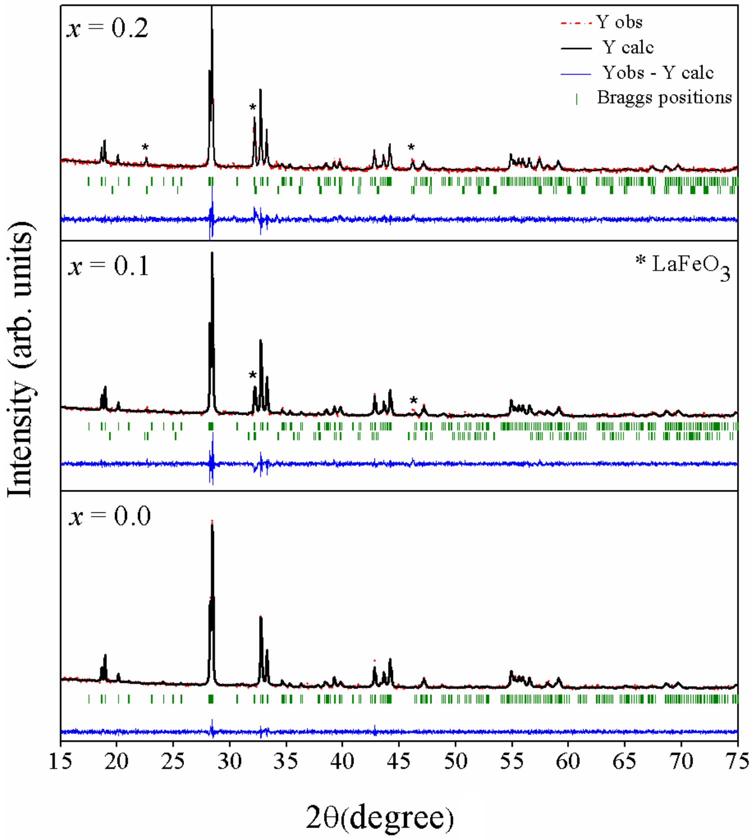

Fig. 4.17. XRD patterns for $Ba_{1-x}La_xFe_2O_4$ (x = 0.0 - 0.2).

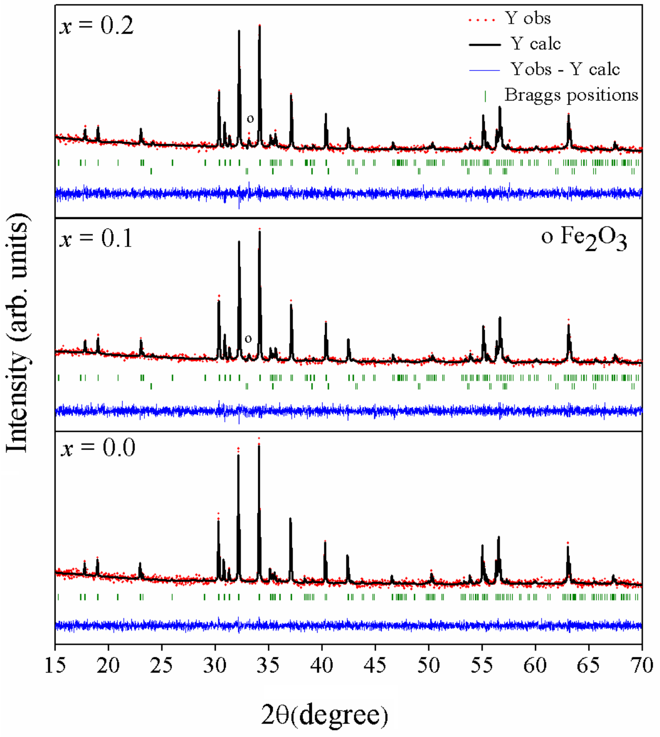

Fig. 4.18. XRD patterns of $Ba_{1-x}La_xFe_{12}O_{19}$ prepared by M-I method.

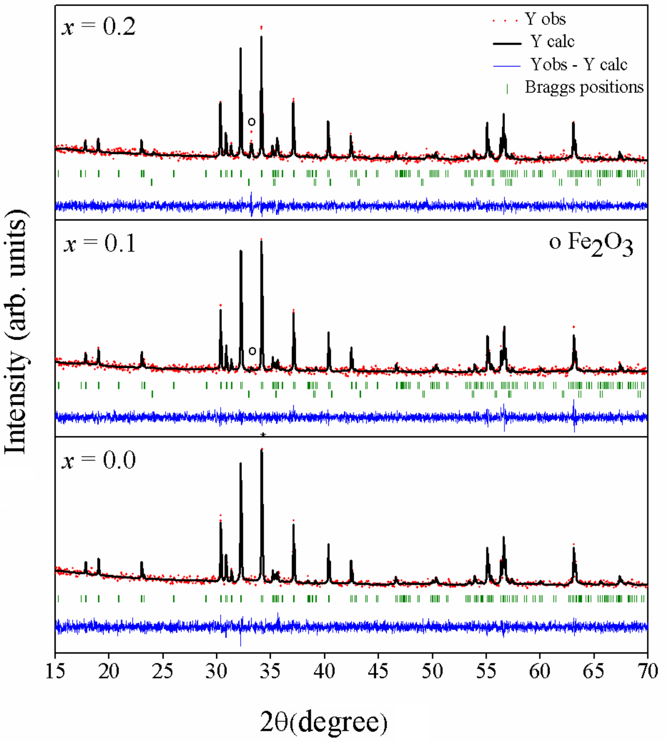

Fig. 4.19. XRD patterns of $Ba_{1-x}La_xFe_{12}O_{19}$ prepared by M-II method.

Table 4.9. Crystallite size, lattice parameters and phase composition of $Ba_{1-x}La_xFe_{12}O_{19}$.

x	Method	Lattice parameters		Volume (Å)^3	Phase (%)	
		***a*(Å)**	***c*(Å)**		**$BaFe_{12}O_{19}$**	**Fe_2O_3**
0.0	(M-I)	5.8955(2)	23.2161(18)	698.81	100	0
	(M-II)	5.8889(2)	23.1871(7)	696.34	100	0
0.1	(M-I)	5.8894(2)	23.1615(12)	695.70	99.78	0.22
	(M-II)	5.8890(9)	23.1725(6)	695.97	99.85	0.15
0.2	(M-I)	5.8897(3)	23.1570(12)	695.61	99.80	0.20
	(M-II)	5.8937(5)	23.1941(2)	697.73	99.57	0.43

Table 4.10. Atomic positions for $Ba_{1-x}La_xFe_{12}O_{19}$, x = 0.0 and x = 0.2 samples prepared from M-I method.

Atoms	Site	$BaFe_{12}O_{19}$			$Ba_{0.8}La_{0.2}Fe_{12}O_{19}$		
		x	***y***	***z***	***x***	***y***	***z***
Ba	2*d*	0.6666	0.3333	0.2500	0.6666	0.3333	0.2500
Fe1	2*a*	0	0	0	0	0	0
Fe2	2*b*	0	0	0.2563(2)	0	0	0.2629(9)
Fe3	$4f_1$	0.3333	0.6666	0.0267(4)	0.3333	0.6666	0.026(8)
Fe4	$4f_2$	0.3333	0.6666	0.191	0.3333	0.6666	0.1904(7)
Fe5	12*k*	0.1689(2)	0.3378(3)	0.8907(3)	0.1617(3)	0.3234(2)	0.8913(4)
O1	4*e*	0	0	0.1508(2)	0	0	0.157(3)
O2	4*f*	0.3333	0.6666	0.9428(4)	0.3333	0.6666	0.943(2)
O3	6*h*	0.1817(4)	0.3654(1)	0.2500	0.1674(2)	0.3411()	0.250
O4	12*k*	0.1565(7)	0.3120(1)	0.0532(3)	0.1670(1)	0.4138(4)	0.0524(3)
O5	12*k*	0.5047	0.0049(4)	0.1508(5)	0.4953(5)	0.0043(1)	0.1531(4)

Table 4.11. Atomic positions for $Ba_{1-x}La_xFe_{12}O_{19}$, $x = 0.0$ and $x = 0.2$ samples, prepared from M-II method.

Atoms	**Site**	**$BaFe_{12}O_{19}$**			**$Ba_{0.8}La_{0.2}Fe_{12}O_{19}$**		
		x	***y***	***z***	***x***	***y***	***z***
Ba	2*d*	0.6666	0.3333	0.2500	0.6666	0.3333	0.2500
Fe1	2*a*	0	0	0	0	0	0
Fe2	2*b*	0	0	0.2563(2)	0	0	0.260(2)
Fe3	$4f_1$	0.3333	0.6666	0.02671	0.3333	0.6666	0.0271(9)
Fe4	$4f_2$	0.3333	0.6666	0.191	0.3333	0.6666	0.1898(8)
Fe5	12*k*	0.1689(2)	0.3378(3)	0.8907(3)	0.170(3)	0.340(3)	0.8908(4)
O1	4*e*	0	0	0.1508(2)	0	0	0.149(3)
O2	4*f*	0.3333	0.6666	0.9428(4)	0.3333	0.6666	0.947(2)
O3	6*h*	0.1817(4)	0.3654(1)	0.2500	0.20(3)	0.367(12)	0.250
O4	12*k*	0.1565(7)	0.3120(1)	0.0532(3)	0.179(1)	0.306(9)	0.0553(4)
O5	12*k*	0.5047	0.0049(4)	0.1508(5)	0.499(7)	0.0043(7)	0.1515(4)

4.4.2. Mössbauer study

R-*T* Mössbauer spectra of $Ba_{1-x}La_xFe_{12}O_{19}$ ($x = 0.0 - 0.2$) prepared by M-I and M-II methods are shown in **Fig. 4.20 and 4.21**. All spectra are fitted with a non-linear least-square method. The spectrum shows five discrete sextets, each sextet corresponding to one of the five crystallographic sites for Fe^{3+} i.e. 12*k*, $4f_1$, $4f_2$, 2*a* and 2*b*. The fitted parameters are the hyperfine field (B_{hf}), the quadrupolar splitting (*QS*) and the isomer shift (δ). It is observed that the fitted values are consistent for both methods and comparable with previously reported results for $BaFe_{12}O_{19}$ [71]. The obtained hyperfine parameters are listed in **Table 4.12**. For both M-I and M-II methods, B_{hf} for all sites is found to increase with La-substitution amount till $x = 0.1$ and then decreases for $x = 0.2$. *QS* for $Ba_{1-x}La_xFe_{12}O_{19}$ is smaller than that of $BaFe_{12}O_{19}$, which shows that La^{3+} substituted samples are more symmetric, due to smaller radius of La^{3+} as compared to

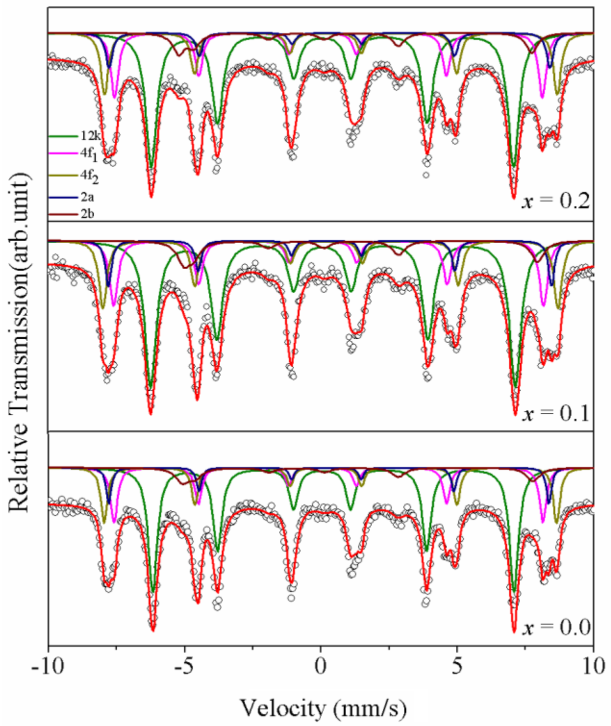

Fig. 4.20. Mössbauer spectra for $Ba_{1-x}La_xFe_{12}O_{19}$ (x = 0.0 - 0.2) prepared by M-I method.

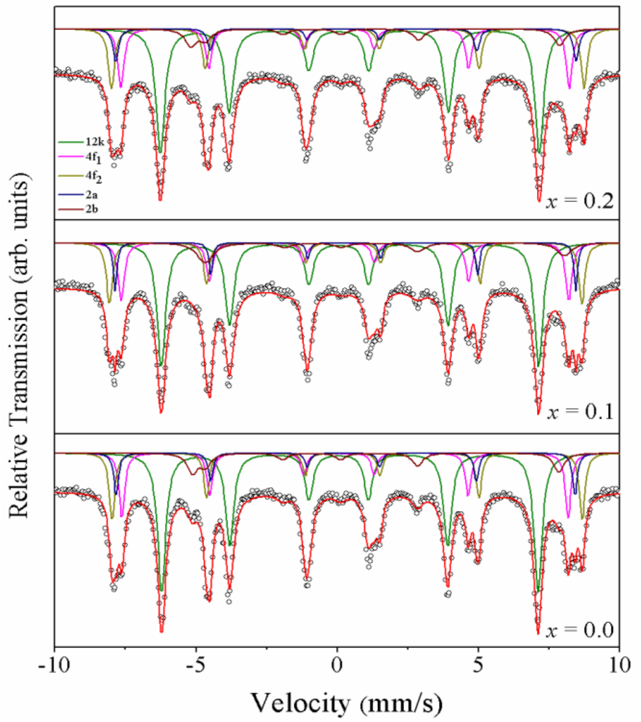

Fig. 4.21. *R-T* Mössbauer spectra for $Ba_{1-x}La_xFe_{12}O_{19}$ (x = 0.0 - 0.2) prepared by M-II method.

Table 4.12. Mössbauer parameters for $Ba_xLa_xFe_{12}O_{19}$ prepared by M-I and M-II method.

Site	***x***	***IS* (mm/s)**		***QS* (mm/s)**		**B_{hf} (T)**	
		M-I	**M-II**	**M-I**	**M-II**	**M-I**	**M-II**
12*k*	0.0	0.24	0.24	0.41	0.39	41.0	41.3
	0.1	0.25	0.24	0.38	0.39	41.4	41.6
	0.2	0.24	0.24	0.36	0.39	41.1	41.5
4f_1	0.0	0.16	0.16	0.21	0.21	48.7	49.0
	0.1	0.17	0.16	0.20	0.20	48.8	49.2
	0.2	0.17	0.16	0.21	0.22	48.6	49.1
4f_2	0.0	0.26	0.26	0.16	0.15	51.4	51.6
	0.1	0.27	0.25	0.14	0.08	51.7	51.8
	0.2	0.27	0.26	0.19	0.19	51.4	51.8
2*a*	0.0	0.24	0.25	0.09	0.07	50.0	50.4
	0.1	0.26	0.26	0.12	0.04	50.3	50.5
	0.2	0.26	0.26	0.09	0.08	50.1	50.5
2*b*	0.0	0.23	0.30	2.24	2.35	39.9	39.9
	0.1	0.28	0.39	2.37	2.50	40.2	40.6
	0.2	0.18	0.30	2.17	2.24	40.1	40.4

Ba^{2+}. δ is found to be increased with La substitution for 2*a*, 2*b* and 4f_2 sites, which suggests the change of Fe^{3+} ion into Fe^{2+} ion. δ is found to be more for samples prepared from M-II method, which may be due to higher site occupancy of La by the M-II method, and therefore more tendency to convert Fe^{3+} to Fe^{2+} for charge compensation.

4.4.3. Magnetic measurement

The *R*-*T* hysteresis loops of $Ba_{1-x}La_xFe_{12}O_{19}$ powders prepared by M-I and M-II methods are shown in **Fig. 4.22** and **4.23** respectively. The *M* of the samples is measured at maximum field of 10 kOe. The magnetic properties are shown in **Table 4.13**. The value

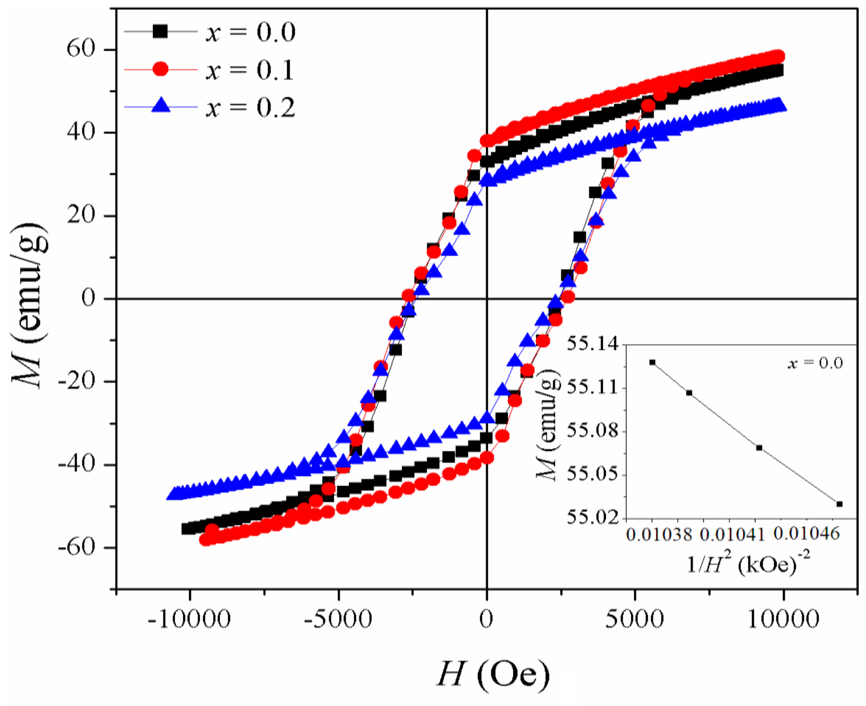

Fig. 4.22. *M-H* loop for $Ba_{1-x}La_xFe_{12}O_{19}$ prepared from M-I method.

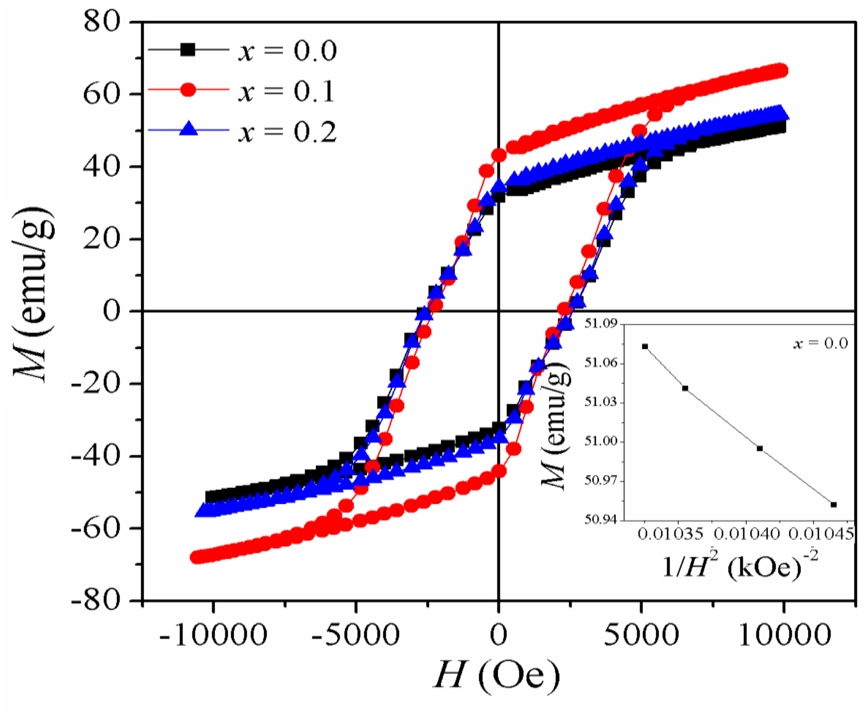

Fig. 4.23. *M-H* loop for $Ba_{1-x}La_xFe_{12}O_{19}$ prepared from M-II method.

Table 4.13. Magnetic properties of $Ba_{1-x}La_xFe_{12}O_{19}$ powders prepared from M-I and M-II method.

x	**Method**	M **(emu/g)**	H_c **(kOe)**	H_a **(kOe)**	$K_1 \times 10^6$ **(erg/cm^3)**
0.0	(M-I)	55.08	2.46	8.31	1.34
	(M-II)	51.41	2.57	8.45	1.24
0.1	(M-I)	59.13	2.68	8.25	1.25
	(M-II)	67.52	2.32	8.55	1.34
0.2	(M-I)	46.51	2.39	8.42	1.41
	(M-II)	55.34	2.51	9.18	1.75

of M increased to the maximum value for $x = 0.1$ and then decreased for $x = 0.2$ for both M-I and M-II, which is in agreement with previously reported results [76-78, 207]. The increase in M for $x = 0.1$ is due to enhancement of B_{hf} at all crystallographic sites. B_{hf} depends upon superexchange interaction and exchange interaction mainly depends on M–O–M bond length. Due to substitution of Ba^{2+} by smaller La^{3+} ion, c-axis decreases, which reduces the Fe–O–Fe bond length [71]; hence exchange interaction increased. Due to increase in exchange interaction, M and B_{hf} also increases. The decrease in M is mainly caused by magnetic dilution and decrease in superexchange interaction field. Substituting La^{3+} for Ba^{2+}, charge compensation occurs by change of valence state of Fe^{3+} to Fe^{2+} at 2*b* site, as is evident from isomer shift, which dilutes the overall magnetization. Thus changing behaviour of magnetic dilution depends on the conversion of Fe^{3+} to Fe^{2+} ionic state on 2*b* site which caused reduction in spin canting, superexchange field and presence of secondary phase α-Fe_2O_3 [71]. However, contrary results are published by H.Sozeri, where M decreased continuously with increase in La substitution $x = 0.0 - 0.5$ [79].

H_c remains nearly constant for all samples; however, a little variation was observed with substitution [**Table 4.13**]. H_c is an extrinsic property which depends upon crystallite size (*C.S.*), particle size, defects, etc. In the case of M-I method, the H_c first increases for $x = 0.1$ and then decreases for $x = 0.2$. H_c is directly related to reduction of *C.S*, from 173.7 nm for $x = 0.0$ to minimum value 142.0 nm for $x = 0.1$, and then increase to 156.2 nm for $x = 0.2$. Decrease in *C.S.* is obtained due to shrinkage along *c*-axis, because of low ionic radius of La^{3+} (0.106 nm) as compared to Ba^{2+} (0.135 nm). Further increase in *C.S.* for $x = 0.2$ is due to a slight increase in *c*-axis. The higher substitution amount of La^{3+} converts Fe^{3+} ion into Fe^{2+} ion, which may also increase the lattice parameters due to larger ionic radius of Fe^{2+} (0.080 nm) than that of Fe^{3+} (0.067nm). In the case of M-II method, H_c decreased first for $x = 0.1$, due to increase in *C.S* from 154 nm to 175 nm as x varies from 0.0 to $x = 0.1$ and further H_c increased for $x = 0.2$, due to decrease in *C.S.* to 169.2 nm. However, the previous studies suggest that with La substitution H_c shows a gradual increase [74]. Nevertheless, in the present work, enhancement in M is observed with marginal variation in H_c.

The magnetic anisotropy field H_a of the samples is determined by the law of approach to saturation. Inset in **Fig. 4.22** and **4.23** shows a plot of M vs $1/H^2$ in the field region 7 kOe $< H <$ 10 kOe, gave a straight line. The obtained values of H_a and K_1 are listed in **Table 4.12**. With increasing the La substitution, a monotonic increase in H_a and K_1 are observed. The increase is explained by the changing Fe^{3+} to Fe^{2+} at the lattice sites, in order to compensate the additional charge due to valance difference of La^{3+} ion and the Ba^{2+} ion.

Fig. 4.24 shows *M-H* loop for La^{3+} substituted BaM films parallel (||) and perpendicular (⊥) direction to the applied magnetic field. M is found to be higher in || direction. However, for $x = 0.1$ M remains nearly same due to random orientation of grains in both directions. **Fig. 4.24 (d)** shows the variation of M and H_c of film in || and ⊥ direction with La^{3+} substitution. M of films is relatively lower than powder sample due to the addition of non-magnetic Bi_2O_3 phase. H_c for La substituted film $x = 0.2$ is quit high than powder due to the higher value of H_a. **Table 4.14** illustrates the observed value of H_a and K_1 for films measured in || and ⊥ directions.

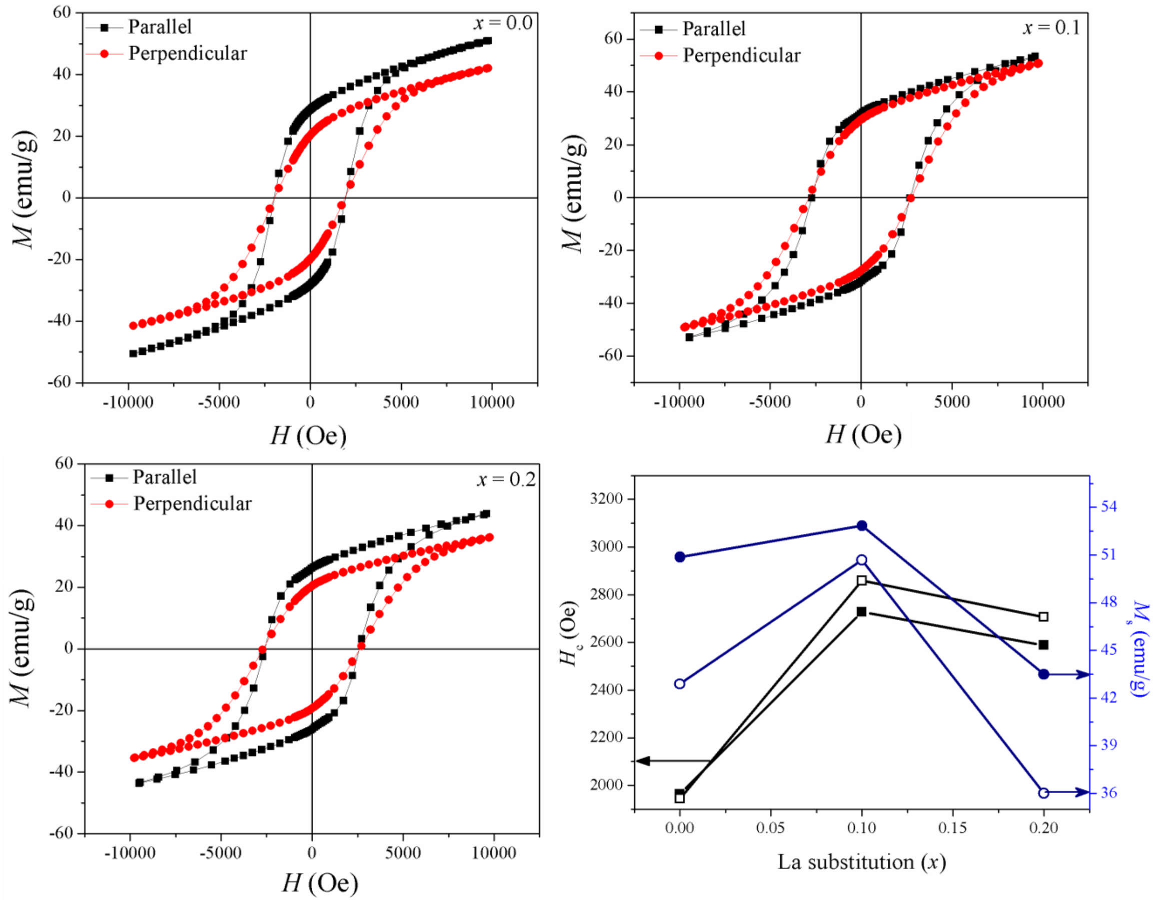

Fig. 4.24. (a-c) Hysteresis loop for $Ba_{1-x}La_xFe_{12}O_{19}$ films in parallel and perpendicular direction **(d)** variation of H_c and M with La substitution.

Table 4.14. The value of H_a and K_1 for films measured in || and ⊥ directions.

x	***H*_a (kOe)**		***K*_1 × 10^6(erg/cm^3)**	
	||	⊥	||	⊥
0.0	9.46	9.42	1.27	1.04
0.1	10.59	11.30	1.48	1.52
0.2	9.84	9.68	1.13	0.92

4.4.4. Surface morphology

Fig. 4.25 shows surface morphology of the sintered $Ba_{1-x}La_xFe_{12}O_{19}$ films. Sintering of the samples results a dense film with limited porosity. The average grain size of the films is found in the range of ~ 2 -3 μm. Micrograph shows that La successfully substituted in BaM, as no pinning effect on the gain boundaries are observed. For x = 0.0 films some aligned grains are found, however the same type of gains morphology are observed for all the films.

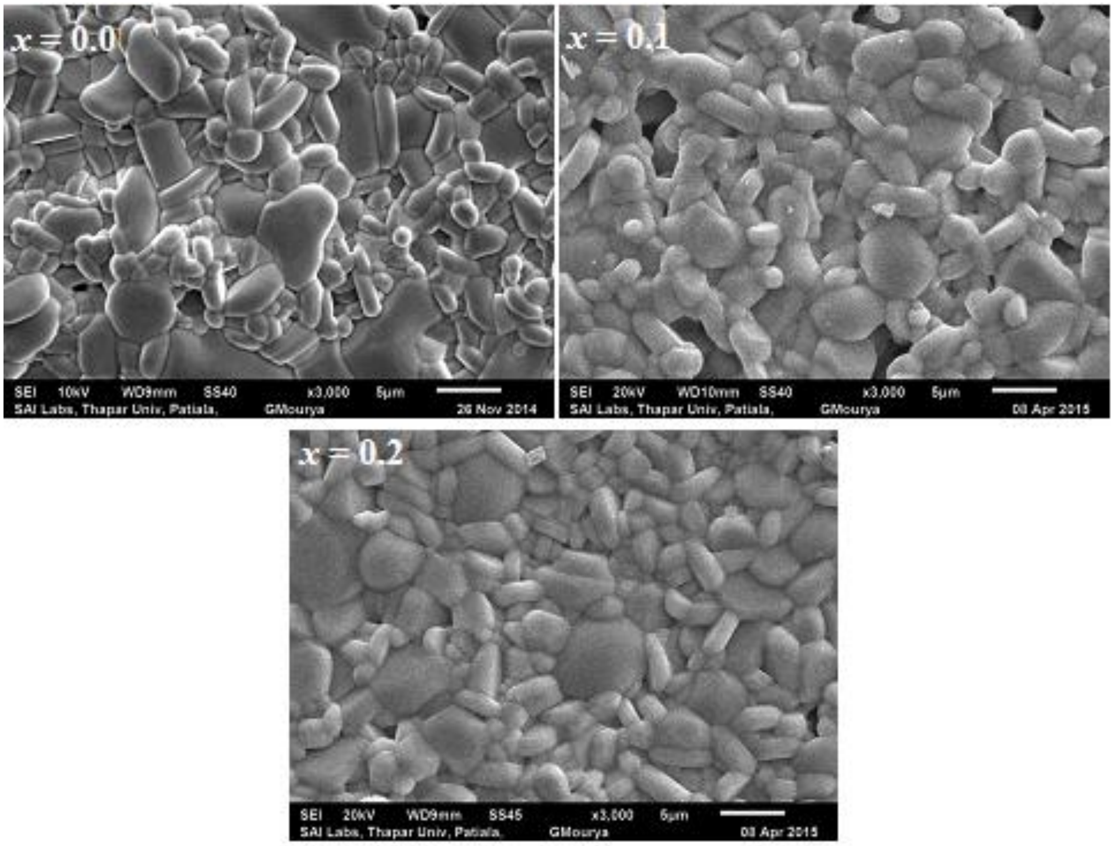

Fig. 4.25. Surface morphology of $Ba_{1-x}La_xFe_{12}O_{19}$ thick film.

4.5. Effect of Co substitution

4.5.1. XRD analysis

Fig. 4.26 shows the x-ray patterns of $BaFe_{12-x}Co_xO_{19}$. For un-substituted sample single phase BaM is formed where all the diffraction peaks matched with standard PCPDF card 27-1029. However, for substituted samples, secondary phase of $Ba_2Co_2Fe_{12}O_{22}$ is also observed. Intensity of secondary phase increases with increase in substitution amount.

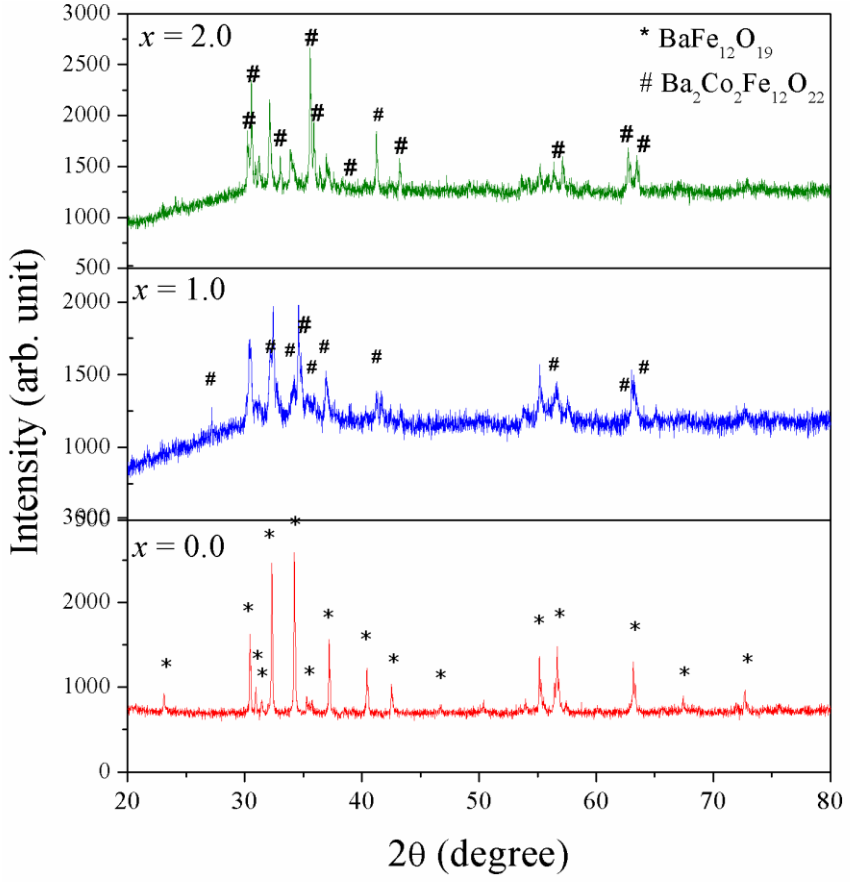

Fig. 4.26 XRD patterns of $BaFe_{12-x}Co_xO_{19}$.

4.5.2. Magnetic measurement

R-T hysteresis loop for all the samples are shown in **Fig. 4.27**. The values of magnetic properties obtained from *M-H* loop are given in **Table 4.15**. *M* is found to increase from

57.2 emu/g to 59.0 emu/g as '*x*' increased from 0.0 to 0.5, and then decreases to 48.4 emu/g for $x = 1.0$. Increased magnetization suggests that Co is substituting at down spin site. Further decrease in M for $x = 1.0 - 2.0$, is attributed to the presence of less magnetic $Ba_2Co_2Fe_{12}O_{22}$ phase [208] and non-magnetic Fe_2O_3 phase. As concentration of substituted amount increases, intensity of secondary phase increases hence H_c decreases. Due to the presence of impurity phase in Co^{2+} substituted BaM powders, studies on BaM thick films are not carried out.

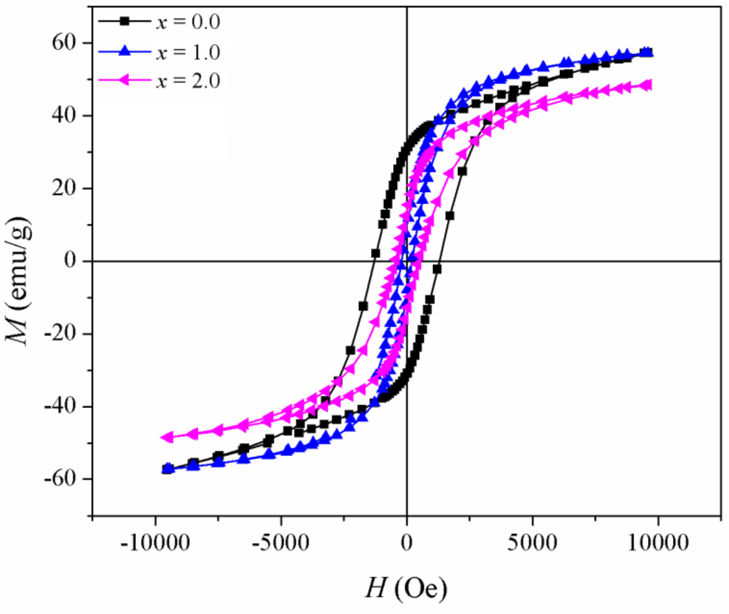

Fig. 4.27 *M-H* loop of $BaFe_{12-x}Co_xO_{19}$.

Table 4.15. Magnetic properties of $BaFe_{12-x}Co_xO_{19}$.

x	***M* (emu/g)**	**M_r (emu/g)**	**H_c (kOe)**
0.0	57.20	30.66	1.31
0.5	59.01	13.67	0.41
1.0	57.20	9.57	0.22
1.5	50.93	8.71	0.19
2.0	48.36	13.48	0.40

4.6. Effect of Ti substitution

4.6.1. XRD analysis

The refined x-ray diffraction patterns of $BaFe_{12-x}Ti_xO_{19}$ are shown in **Fig 4.28**. Single phase $BaFe_{12}O_{19}$ is observed for $x = 0.0 - 1.0$. However for $x = 1.5 - 2.0$, the major phase formed is $Ba_6Fe_{45}Ti_{17}O_{106}$ along with minor BaM and Fe_2O_3 phases. The fitted parameters (R_p, R_{wp} and R_{exp}) and chi^2 (χ^2) for all the samples are below 4.0 and 1.37 respectively, which suggest the refinement is best fitted. Lattice parameters, crystallite size and phase percent as obtained from refinement is listed in **Table 4.16**.

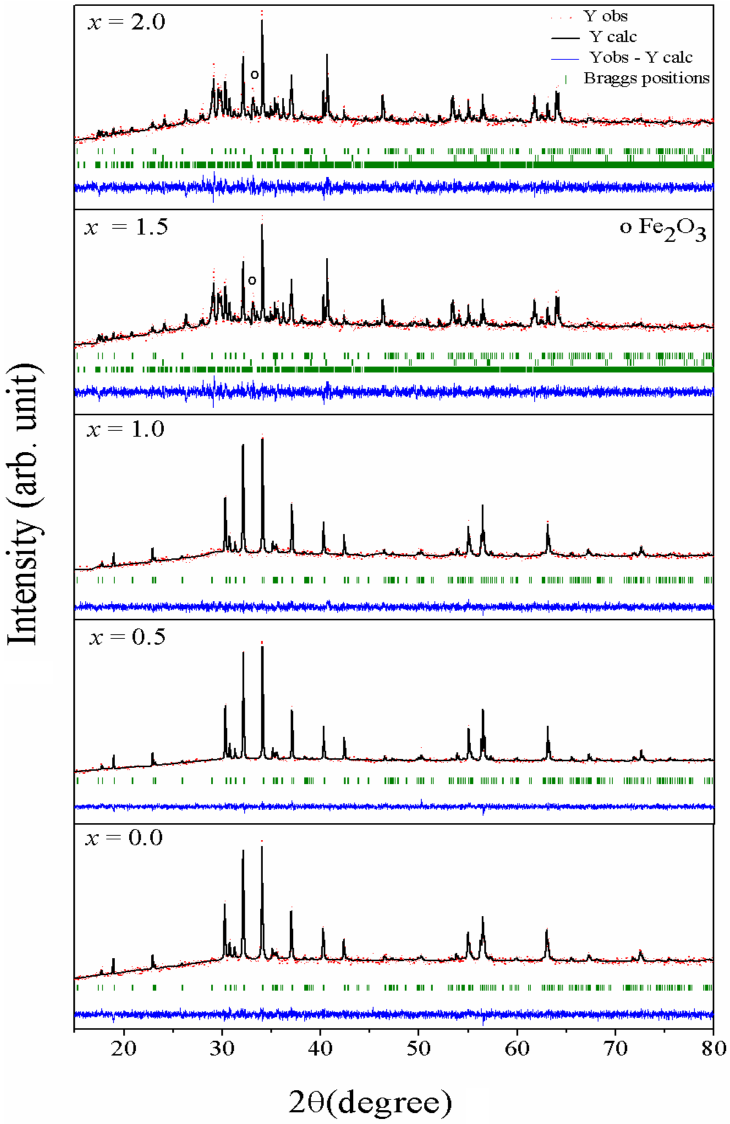

Fig. 4.28. Refined X-ray diffraction patterns for $BaFe_{12-x}Ti_xO_{19}$ ($x = 0.0 - 2.0$).

Table 4.16. Crystallite size, lattice parameters and phase percentage of $BaFe_{12-x}Ti_xO_{19}$.

x	***C.S.*** **(nm)**	**Lattice parameters**		**Phase (%)**		
		***a*(Å)**	***c*(Å)**	**$BaFe_{12}O_{19}$**	**$Ba_6Fe_{45}Ti_{17}O_{106}$**	**Fe_2O_3**
0.0	145.11	5.8964(8)	23.2246(3)	100.0	0.0	0.0
0.5	148.57	5.8896(8)	23.2328(6)	100.0	0.0	0.0
1.0	136.99	5.8889(9)	23.2523(10)	100.0	0.0	0.0
1.5	151.39	5.8886(2)	23.2352(11)	51.54	48.21	0.25
2.0	178.90	5.8909(3)	23.2392(14)	5.68	93.94	0.38

4.6.2. Magnetic measurement

R-T hysteresis loop of $BaFe_{12-x}Ti_xO_{19}$ is shown in **Fig. 4.29**. *M-H* loop clearly shows that lower substitution of Ti^{4+} (x = 0.5) shows high magnetization; however, it decreased dramatically to a very small value for large concentration of Ti^{4+}. H_c does not show much variation with substitution amount. Relevant magnetic properties of $BaFe_{12-x}Ti_xO_{19}$ are tabulated in **Table 4.17**.

The decrease in M with increasing substitution of Ti^{4+} ions can be understand by considering the magnetic moments of the substituted ions. In the present ferrite system, Fe^{3+} ions of magnetic moment ($5\mu_B$) are replaced by non magnetic Ti^{4+} ions. This leads to decrease in superexchange interaction field and hence magnetization of the samples. Further, the magnetic dilution is also caused due to the presence of paramagnetic phase $Ba_6Fe_{45}Ti_{17}O_{106}$ [209], which increase with increase in doping concentration. Mössbauer spectroscopy shows that the Ti^{4+} ion preferred to occupy the 2*b* (spin up site), hence M decreases. It is well known that H_c is associated with its H_a and particle size. The obtained values of H_a and K_1 are listed in **Table 4.17.** Table shows that with increasing the Ti substitution above x = 0.5, a monotonic decrease in H_a and K_1 are observed. The decrease in H_a is responsible for low value of H_c.

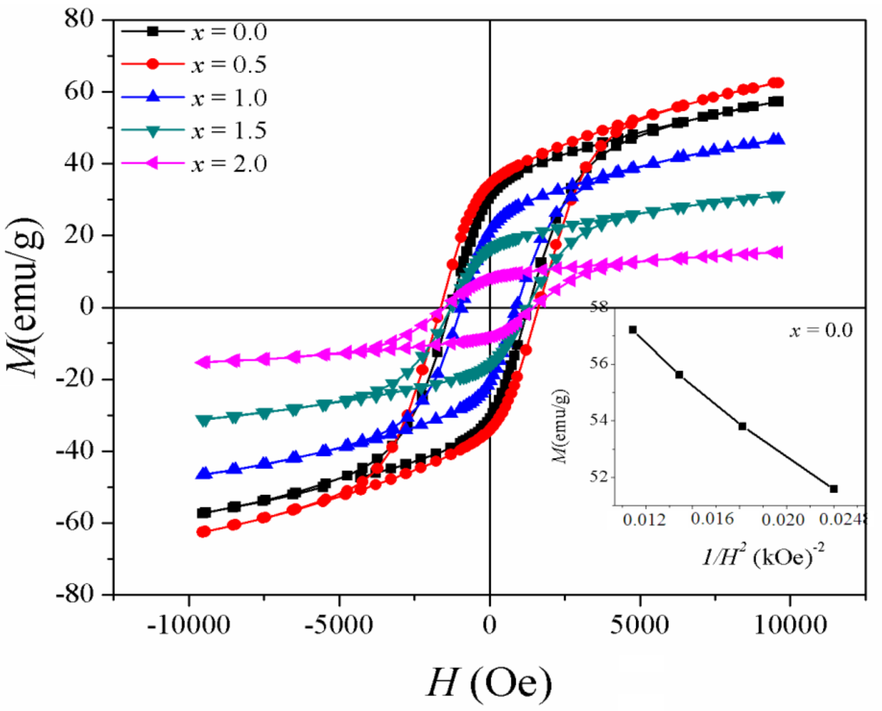

Fig. 4.29. Hysteresis loop for $BaFe_{12-x}Ti_xO_{19}$ ($x = 0.0 - 2.0$). Inset shows the dependence of M and $1/H^2$ for $x = 0.0$.

Table 4.17: Magnetic properties and first anisotropy constant (K_1) for $BaFe_{12-x}Ti_xO_{19}$ ($x = 0.0 - 2.0$).

x	M (emu/g)	M_r (emu/g)	H_c (kOe)	H_a (kOe)	$K_1 \times 10^6$ (erg/cm^3)
0.0	57.24	30.78	1.34	9.52	1.45
0.5	62.42	34.21	1.65	9.92	1.61
1.0	46.51	21.25	0.91	8.43	1.02
1.5	31.14	16.12	1.32	6.31	0.31
2.0	15.32	8.13	1.51	4.82	0.22

4.7. Effect of Co-Ti substitution

4.7.1. XRD analysis

Fig. 4.30 shows the refined XRD diffraction patterns of calcined $BaFe_{12-2x}Co_xTi_xO_{19}$ powders. All peaks correspond to single phase BaM with $P6_3/mmc$ space group. No secondary phase is detected within the measurable limits of XRD. The lattice parameters

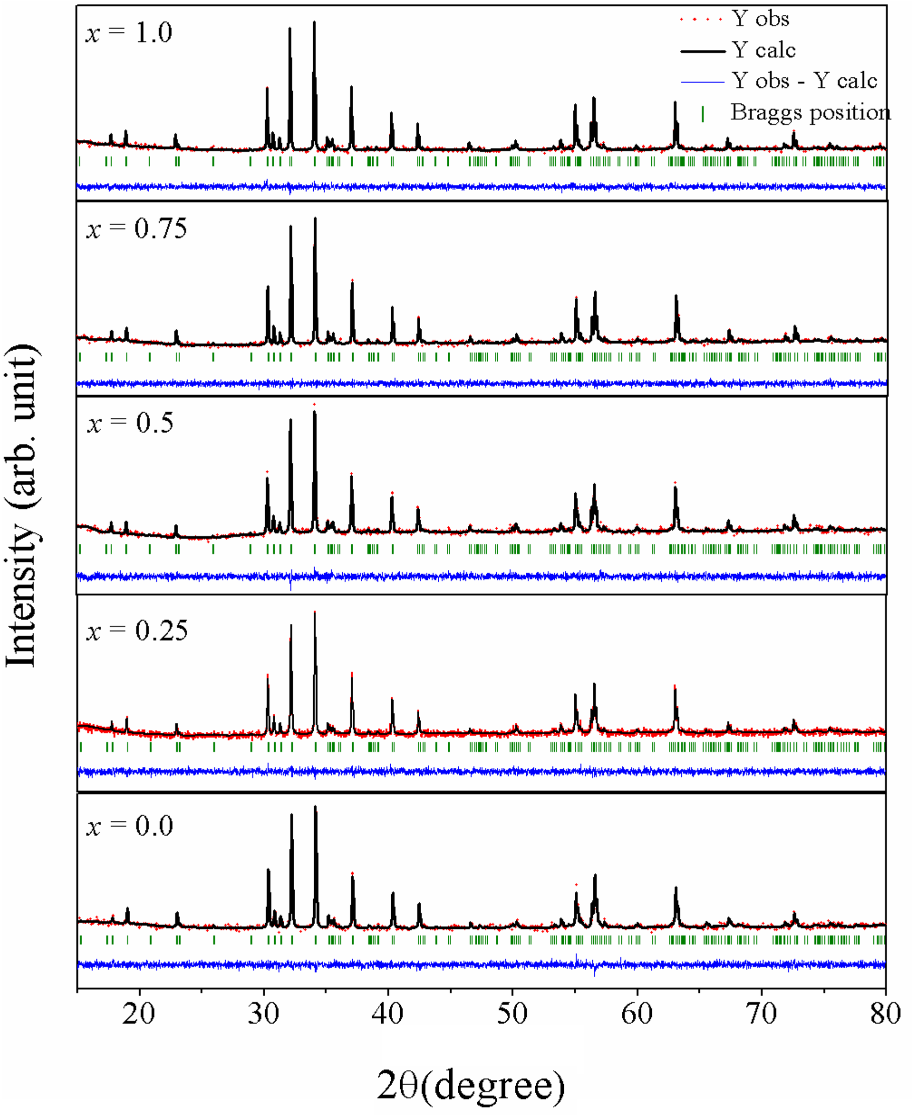

Fig. 4.30 Refined XRD patterns of $BaFe_{12-2x}Co_xTi_xO_{19}$ powders.

(a and c), R-factors (R_p, R_w, R_{exp} and χ^2) and average crystallite size (*C.S.*), as obtained from refinement are tabulated in **Table 4.18**. The values of fitting parameters suggest that refinement is best fitted. The increase in lattice parameters is attributed to the fact that ionic radii of substituted Co^{2+} and Ti^{4+} ions are larger compared to the Fe^{3+} ion [121]. Peaks shift towards lower angle indicates the compressive strains due to larger ionic radii of Co^{2+} and Ti^{4+} [**Fig. 4.31**]. Average crystallite size is also found to increase from 123.7 nm to 151.2 nm. The refined atomic positions for the $BaFe_{12}O_{19}$ and $BaFe_{10}Co_1Ti_1O_{19}$ are listed in **Table 4.19**. The difference in atomic position parameter values resulting from the substitution of Co^{2+}-Ti^{4+} for Fe^{3+} ion.

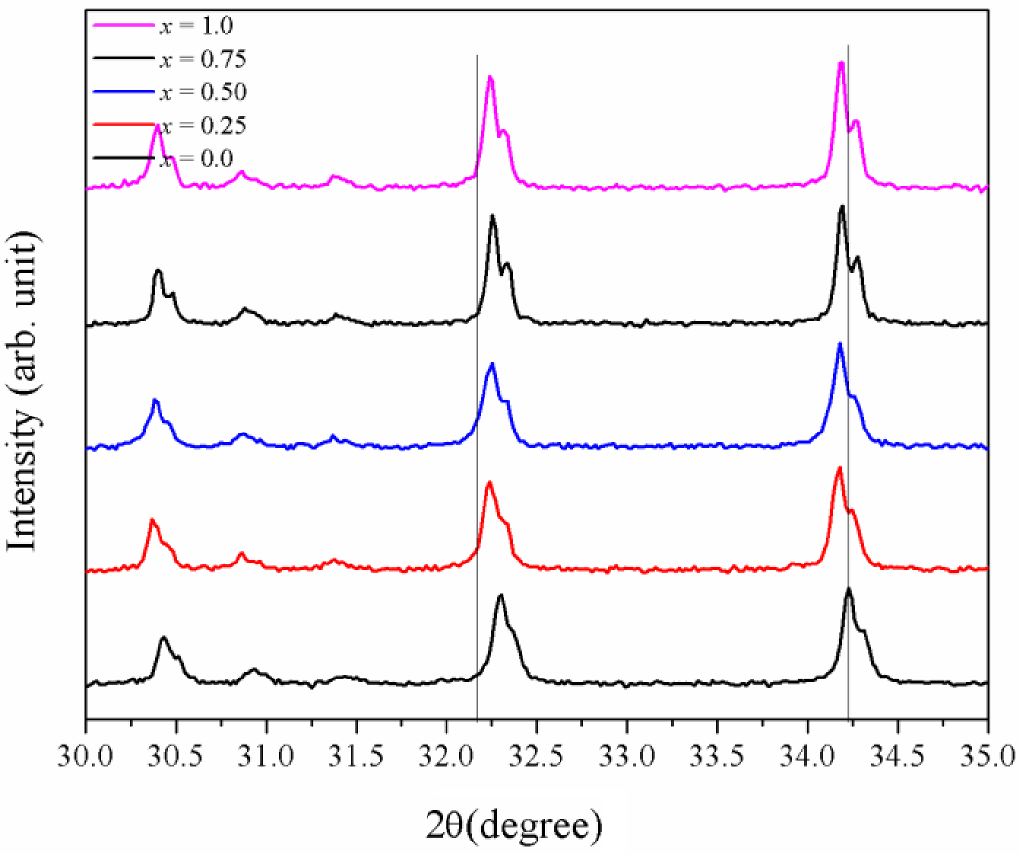

Fig. 4.31. XRD patterns of the peaks in 2θ range 31.5 - 35.0°.

Table 4.18. Crystallite size (*C.S.*), lattice parameters (*a* and *c*) and *R*-factors (R_p, R_w, R_{exp} and χ^2) of $BaFe_{12-2x}Co_xTi_xO_{19}$ powders.

x	***C.S.* (nm)**	**Lattice parameters**		***R*-factors**			
		***a*(Å)**	***c*(Å)**	R_p	R_w	R_{exp}	χ^2
0.0	123.11	5.8912(2)	23.2005(2)	3.06	3.85	3.65	1.12
0.25	124.67	5.8936(5)	23.2091(2)	3.15	3.97	3.62	1.20
0.50	140.04	5.8937(5)	23.2121(2)	3.09	3.86	3.66	1.11
0.75	145.18	5.8941(4)	23.2182(9)	3.01	3.78	3.61	1.09
1.0	151.04	5.8952(3)	23.2331(9)	2.96	3.74	3.52	1.13

Table 4.19. Atomic positions for $BaFe_{12}O_{19}$ and $BaFe_{10}Co_1Ti_1O_{19}$ samples, as obtained from the Rietveld analysis.

Atoms	**Site**	$BaFe_{12}O_{19}$			$BaFe_{10}Co_1Ti_1O_{19}$		
		x	*y*	*z*	*x*	*y*	*z*
Ba	2*d*	0.6666	0.3333	0.2500	0.6666	0.3333	0.2500
Fe1	2*a*	0	0	0	0	0	0
Fe2	2*b*	0	0	0.2605(1)	0	0	0.2604(4)
Fe3	$4f_1$	0.3333	0.6666	0.0265(3)	0.3333	0.6666	0.0292(8)
Fe4	$4f_2$	0.3333	0.6666	0.1901	0.3333	0.6666	0.1900(3)
Fe5	12*k*	0.170(4)	0.3404(7)	0.8911(5)	0.1642(3)	0.3285(1)	0.8918(8)
O1	4*e*	0	0	0.1507(2)	0	0	0.1548(9)
O2	4*f*	0.3333	0.6666	0.9416(9)	0.3333	0.6666	0.9465(6)
O3	6*h*	0.1972(1)	0.3655(5)	0.2500	0.1817(2)	0.3292(2)	0.2500
O4	12*k*	0.1560(7)	0.3123(8)	0.0572(4)	0.1558(1)	0.3119(4)	0.0523(6)
O5	12*k*	0.4767(5)	0.0043(2)	0.1527(3)	0.4993(5)	0.0043(1)	0.1519(4)

4.7.2. Mössbauer analysis of $BaFe_{12-2x}Co_xTi_xO_{19}$ powders

Fig. 4.32 shows *R-T* Mössbauer spectra of $BaFe_{12-2x}Co_xTi_xO_{19}$ powders. Spectra is fitted with five discrete sextets, corresponding to five different crystallographic Fe^{3+} sites i.e. 12*k*, 4f_1, 4f_2, 2*a* and 2*b*. For non-substituted sample, sub-spectral areas are constrained in the ratio of 6:2:2:1:1, and are kept free for substituted samples. The obtained fitted parameters, hyperfine field (B_{hf}), quadrupolar shift (*QS*), isomer shift (δ) line width (Γ) and relative sub-spectral (*S*) area are given in **Table 4.20**. The occupation number for Fe ion (N_{Fe}) and occupancy fraction of Co-Ti ($F_{Co\text{-}Ti}$) on the i^{th} site are estimated by using the formulae [210];

$$N_{\mathrm{Fe}}(i) = C_{\mathrm{Fe}}\left[\frac{S(i)}{\sum_{i=1}^{5} S(i)}\right] \tag{4.6}$$

$$F_{\mathrm{Co-Ti}}(i) = \frac{N(i) - N_{\mathrm{Fe}}(i)}{N(i)} \times 100\% \tag{4.7}$$

The $N_{Fe}(i)$ and $F_{Co\text{-}Ti}$ for Fe on the five sites are plotted in **Fig. 4.33 (a)** and **(b)** respectively. It is evident that Co-Ti ions sequentially occupies at 2*b*, 4f_2, 12*k*, 4f_1, however, 2*a* site is least substituted which is diverse to previously reported results [16]. The preferential site occupation of ions depends on its ionic radii and electronegativity. Owing to larger void space in octahedral (12*k*, 2*a* and 4f_2) compared to tetrahedral (4f_1) and bi-pyramidal (2*b*) site; the ion with larger ionic radii (Co^{2+}) preferably occupies 12*k*, 2*a* and 4f_2, whereas with smaller Ti^{4+} ion at 4f_1 and 2*b* site. Moreover, electronegativity of Co^{2+} and Ti^{4+} ions are 1.83 and 1.54 respectively; hence higher electronegative Co^{2+} ion preferably occupies octahedral sites [211].

Cumulative sum of B_{hf} at parallel and antiparallel site shows an increase with maximum at $x = 0.75$ and then decreases [**Table 4.20]**. This suggests that occupancy fraction is relatively higher at antiparallel 4f_1 and 4f_2 sites [**Fig. 4.33 b**]. Decrease in B_{hf} for $x = 1$, is attributed to higher occupancy fraction of low magnetic moment Co^{2+} (3.0 μ_B) and nonmagnetic Ti^{4+} ions. No measurable change in δ is observed, suggests no change in valence state for Fe^{3+} ion. A small change in *QS* with increasing '*x*' indicates slight site distortion due to larger ionic radii of Co^{2+} and Ti^{4+} ions.

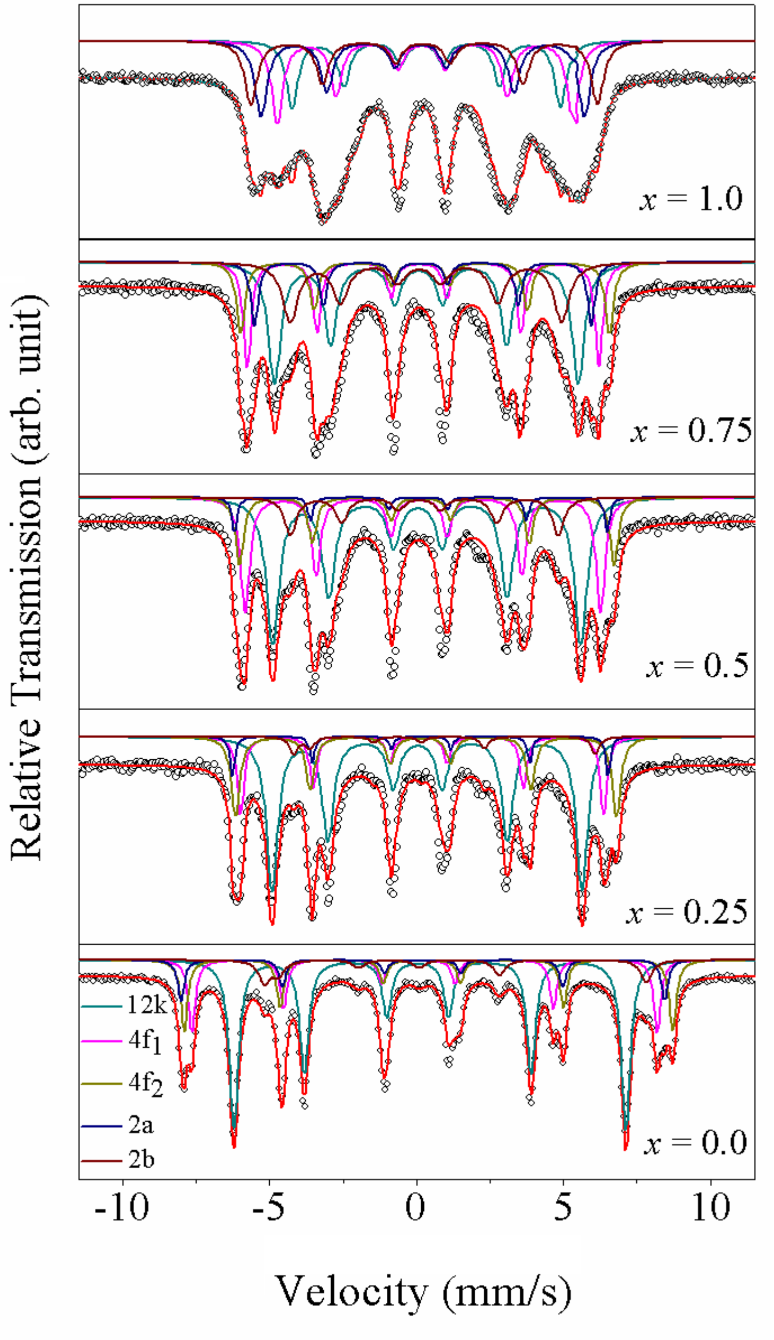

Fig. 4.32. Mössbauer spectra for $BaFe_{12-2x}Co_xTi_xO_{19}$ powders.

Table 4.20. Mössbauer parameters of $BaFe_{12-2x}Co_xTi_xO_{19}$ powders.

Sites	X	Γ (mm/s)	δ (mm/s)	QS (mm/s)	B_{hf} (T)	S (%)
12k	0.0	0.36	0.25	0.40	40.57	50.0
	0.25	0.42	0.24	0.38	40.81	51.08
	0.50	0.48	0.22	0.31	41.27	52.55
	0.75	0.53	0.26	0.36	41.35	53.01
	1.0	0.58	0.31	0.28	40.96	53.45
$4f_1$	0.0	0.28	0.25	0.23	48.71	16.66
	0.25	0.39	0.25	0.17	48.82	17.62
	0.50	0.41	0.26	0.16	48.75	17.02
	0.75	0.48	0.27	0.15	46.87	17.23
	1.0	0.52	0.29	0.14	46.85	18.22
2a	0.0	0.24	0.22	0.18	51.52	8.33
	0.25	0.26	0.16	0.16	51.64	8.64
	0.50	0.30	0.13	0.17	51.84	9.06
	0.75	0.38	0.22	0.19	52.93	9.28
	1.0	0.42	0.24	0.15	52.01	9.46
$4f_2$	0.0	0.27	0.24	0.22	50.07	16.66
	0.25	0.33	0.24	0.23	50.22	15.32
	0.50	0.42	0.25	0.25	50.59	14.35
	0.75	0.52	0.25	0.32	51.96	14.08
	1.0	0.61	0.29	0.34	51.09	13.75
2b	0.0	0.45	0.22	2.25	40.41	8.33
	0.25	0.51	0.29	2.20	40.53	7.34
	0.50	0.68	0.31	2.12	40.64	7.02
	0.75	0.72	0.35	1.99	42.52	6.41
	1.0	0.81	0.42	1.34	40.01	5.12

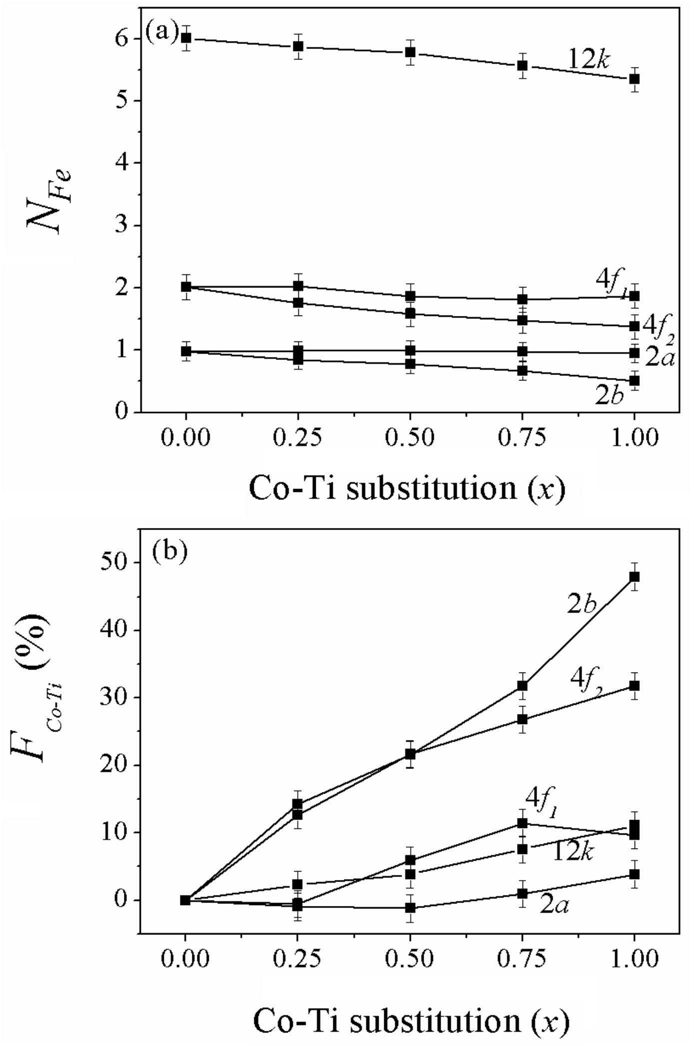

Fig. 4.33 (a) Site occupation number for Fe (N_{Fe}) and **(b)** occupancy fraction of Co-Ti ($F_{Co\text{-}Ti}$) ions as obtained from mössbauer fitting for $BaFe_{12-2x}Co_xTi_xO_{19}$.

4.7.3. Magnetic measurement

Fig. 4.34 shows *M-H* loops of $BaFe_{12-2x}Co_xTi_xO_{19}$ powders. Variation in *M*, H_c and remanence (M_r) with substitution is given in **Fig. 4.35**. *M* was found to increase from 55.6 emu/g to 62.1 emu/g as '*x*' increases from 0.0 to 0.75, and then decreases to 58.5 emu/g for $x = 1.0$. The *M* is directly associated with B_{hf} which is found to be highest for $x = 0.75$. M_r also decreases gradually with minimum (~ 4 emu/g) at $x = 1.0$. The sharp decrease in H_c from 1.98 kOe ($x = 0.0$) to 0.08 kOe ($x = 1.0$), exhibits a soft magnetic behavior [211].

Fig. 4.36 (a-e) shows *M-H* loops for Co-Ti substituted BaM films in parallel (||) and perpendicular (⊥) to the applied magnetic field. It is evident from figures that M and M_r are higher in || direction. **Fig. 4.36 (f)** shows the variation of M and H_c of films in || and ⊥ directions. The magnetic properties of films are comparable to the powders. However, M of films is relatively lower than powder which is due to addition of nonmagnetic Bi_2O_3 phase for better adhesion between substrate and films. H_c of BaM is governed by its anisotropy field (H_a) according to the relation [46]

$$H_c = C\,(H_a - N_d M_s) \tag{4.8}$$

where, C is constant and N_d is demagnetization factor which depends upon grain size and shape. H_a can be obtained from the law of approach to saturation. The linear nature of M vs $1/H^2$ in the field region 6 kOe < H < 10 kOe is found for all powder samples and films. Inset **Fig. 4.34** shows the linear dependence of M with $1/H^2$. The calculated values of H_a and K_1 for powders and films are listed in **Table 4.21** which shows that H_a declined considerably for substituted films. Higher value of H_a in ⊥ direction (x = 0.5) shows that Co-Ti promotes out-of-plane anisotropy. The site anisotropy of BaM has following order: 2*b* > 4f_2 > 2*a* > 4f_1 > 12*k* [213], hence reduction in H_a and H_c also supports that Co and Ti ions replaces Fe^{3+} at high anisotropic site 2*b* and 4f_2 sites **Fig. 33(b)**.

Table 4.21. The variation of magnetocrystalline anisotropy (H_a) and first anisotropy constant (K_1) with Co-Ti substitution '*x*' of powders and films measured in parallel (||) and perpendicular (⊥) direction.

x	**H_a (kOe)**			**$K_1 \times 10^6$ (erg/cm^3)**		
	Powder	**Film (||)**	**Film (⊥)**	**Powder**	**Film (||)**	**Film (⊥)**
0.0	8.59	9.84	9.42	1.26	1.32	1.05
0.5	8.26	8.68	10.02	1.34	1.33	1.31
1.0	3.14	4.53	4.43	0.49	0.62	0.55

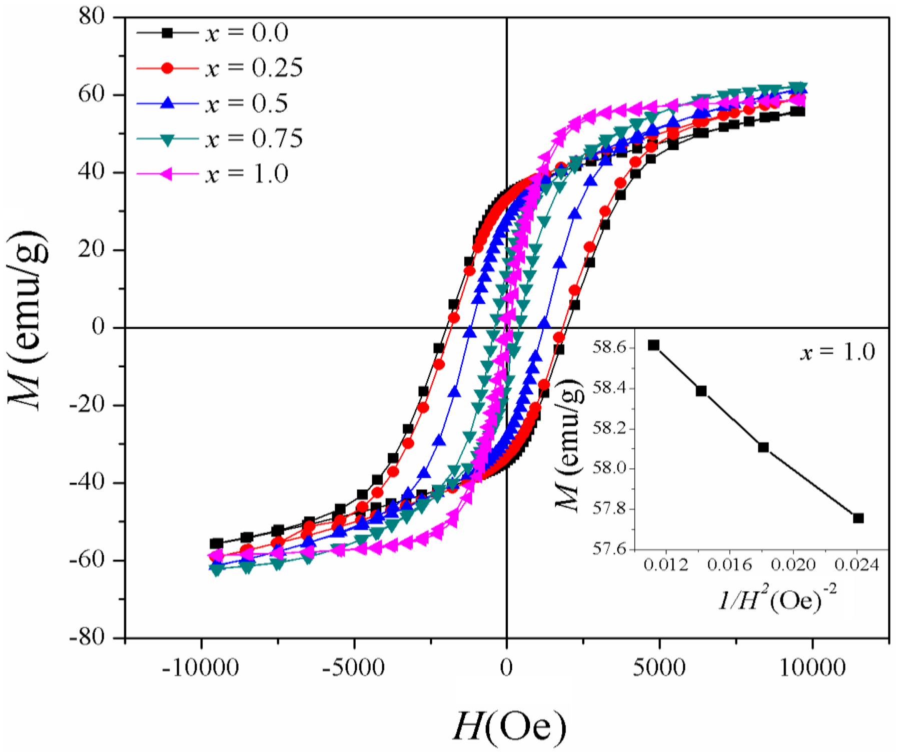

Fig. 4.34. Hysteresis loop of $BaFe_{12-2x}Co_xTi_xO_{19}$ powders. The inset shows the dependence of M on $1/H^2$.

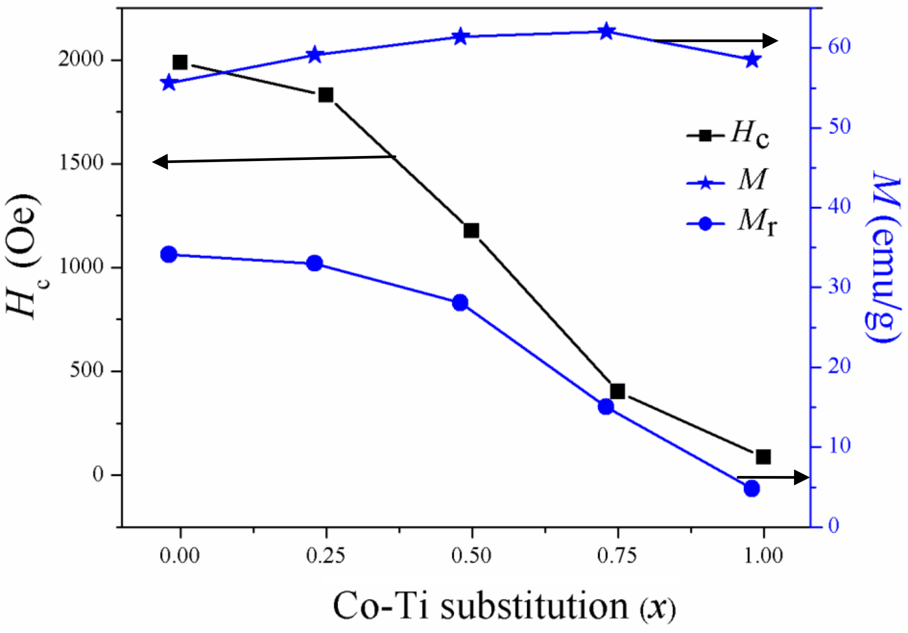

Fig. 4.35. Variation of H_c, M and M_r with Co-Ti substitution.

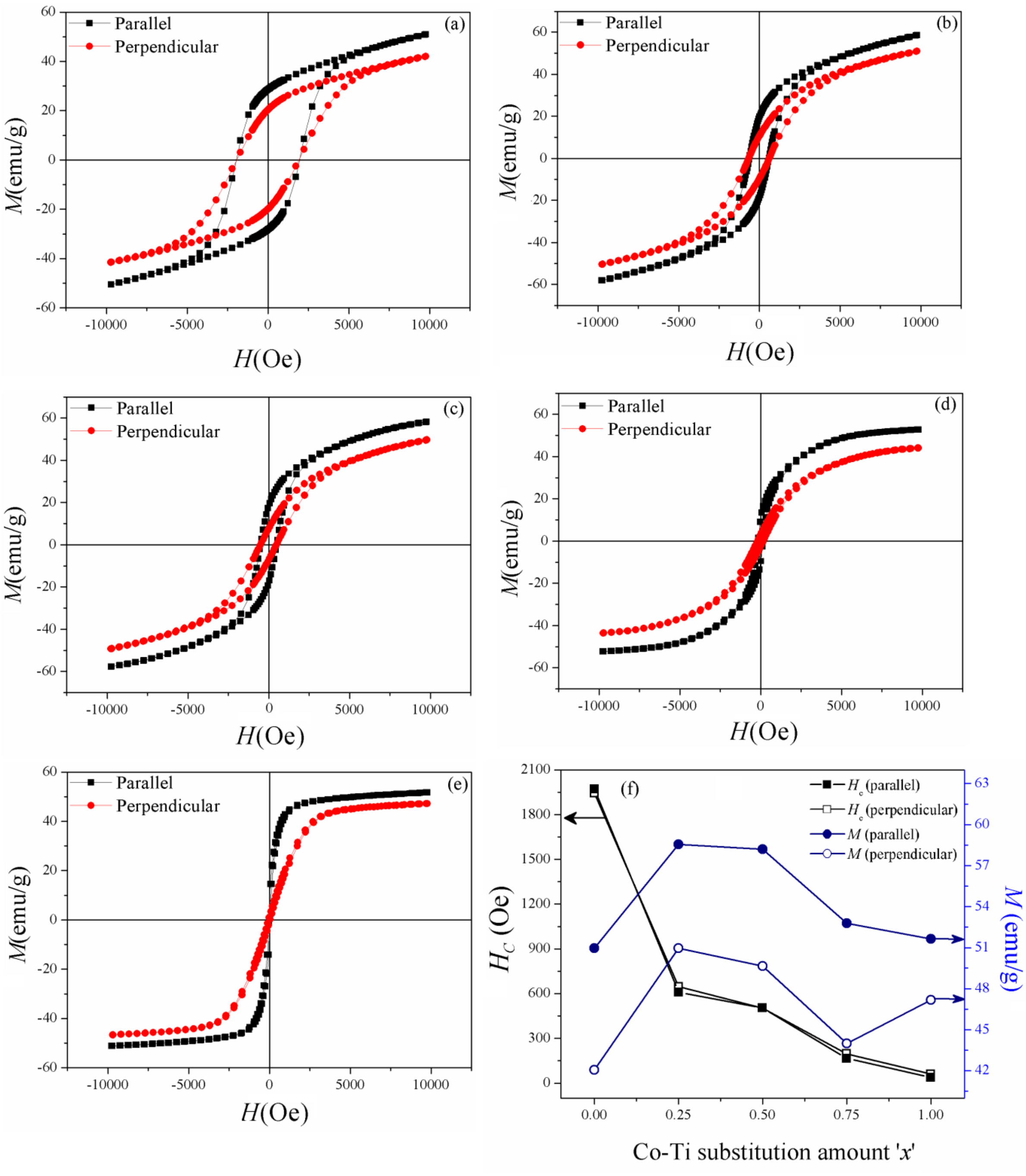

Fig. 4.36. Hysteresis loop for $BaFe_{12-2x}Co_xTi_xO_{19}$ films in parallel and perpendicular direction **(a)** x = 0.0, **(b)** x = 0.25, **(c)** x = 0.5, **(d)** x = 0.75 **(e)** x = 1.0 and **(f)** variation of H_c and M with Co-Ti substitution.

4.7.4. Surface morphology

Fig 4.37 (a-c) shows the SEM micrographs of sintered BaM films for $x = 0.0$, 0.5 and 1.0 respectively. All films show dense microstructure with limited porosity. Microstructural features of substituted films are remarkably distinct. Non-substituted film shows elongated grains, whereas grains become hexagonal for substituted films. The enlarged view of hexagonal grain is also depicted in fig. 6c. The higher H_a in ⊥ direction for substituted film may attribute to higher fraction of perpendicularly aligned hexagonal grains ($x = 0.5$). **Fig. 4.37 (a)** shows the cross sectional image of the BaM thick film. The initial thickness of the BaM film is kept constant to ~ 80 μm. The measured final thickness of the film is ~ 72 μm. Thickness of film is uniform throughout the cross section. The decrease in thickness is the effect of shrinkage during the sintering, which leads densification of the films [205]. The sharp interface between the film and substrate suggest no inter diffusion.

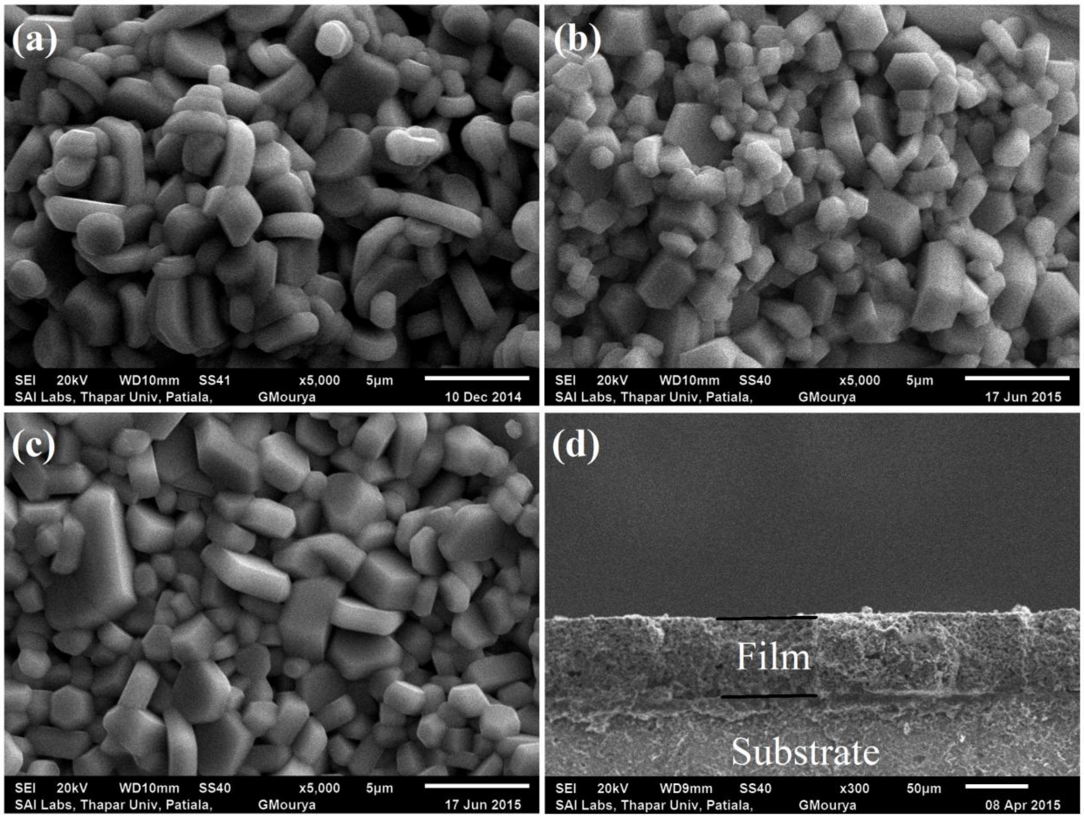

Fig. 4.37. SEM images of $BaFe_{12-2x}Co_xTi_xO_{19}$ films (a) $x = 0.0$ (b) $x = 0.5$ (c) $x = 1.0$ (d) film cross section. Inset in fig. 4.38(c) shows the hexagonal grain.

4.8. Investigation of microwave properties of BaM powder

Microwave electromagnetic SE and R_L are measured at room temperature by using two ports vector network analyzer. Shielding is the process of limiting the flow of electromagnetic field between two locations. Electromagnetic shielding effectiveness of a material is defined as the ratio of transmitted power to incident power and is given by

$$SE_t\ (dB) = SE_r + SE_a + SE_m = 10log_{10}\left(\frac{P_T}{P_I}\right) + 10log_{10}\left(\frac{E_T}{E_I}\right) + 10log_{10}\left(\frac{H_T}{H_I}\right), \quad (4.9)$$

where SE_t is the total shielding effectiveness, S_r is shielding due to reflection, SE_a is shielding due to absorption and SE_m is shielding due to multiple reflection, P_I (E_I or H_I) and P_T (E_T or H_T) are power (electric and magnetic field intensity) of incident and transmitted electromagnetic waves respectively. The incident and transmitted wave can be mathematically represented by scattering parameters (S- parameters) i.e. S_{11} (or S_{22}) and S_{12} (or S_{21}) respectively. Where, S_{11} and S_{12} represent the reflection (R) and transmittance (T) wave i.e.

$$R = |S_{11}|^2 = |S_{22}|^2 \quad (4.10)$$

$$T = |S_{12}|^2 = |S_{21}|^2 \quad (4.11)$$

The absorbance was calculated as

$$A = 1 - R - T \quad (4.12)$$

If the effect of multiple reflections is negligible, then the effective intensity of EM wave is

$$A_{eff} = \frac{1-R-T}{1-R} \quad (4.13)$$

Also, SE_M is negligible, when $SE_A \geq 10$ dB. Therefore

$$SE_t\ (dB) = SE_r + SE_a \quad (4.14)$$

where,

$$SE_r = -10\ log_{10}(1-R) \quad (4.15)$$

$$SE_a = -10\ log_{10}\left(1 - A_{eff}\right) = -10\ log_{10}\left(\frac{T}{1-R}\right) \quad (4.16)$$

The microwave reflection loss (R_L) are calculated according to equation

$$R_L = -20\, log_{10}\, |S_{11}|\, dB \tag{4.17}$$

Fig. 4.38 – 4.40 shows the frequency dependent shielding effectiveness (SE_a, SE_r , SE_t) of the BaM powder for different Fe/Ba mole ratio in the frequency range of 12-18 GHz. Shielding spectra shows a resonance peak for each sample which shifts continuously towards lower frequency band with in decrease Fe/Ba mole ratio '*x*'. Maximum absorption shielding effectiveness (SE_a) 10.20 dB is obtained for x = 5.0 at frequency 14.0 GHz. Same trend is obtained for reflection shielding effectiveness (SE_r); however this variation is very small. Thus the total shielding effectiveness (SE_t) mainly dominated by SE_a, while SE_r remains nearly constant. Total shielding effectiveness SE_t is found to be maximum 15.12 dB for x = 5.0 at frequency 13.9 GHz and minimum 7.8 dB for x = 6.0 at 15.8 GHz respectively.

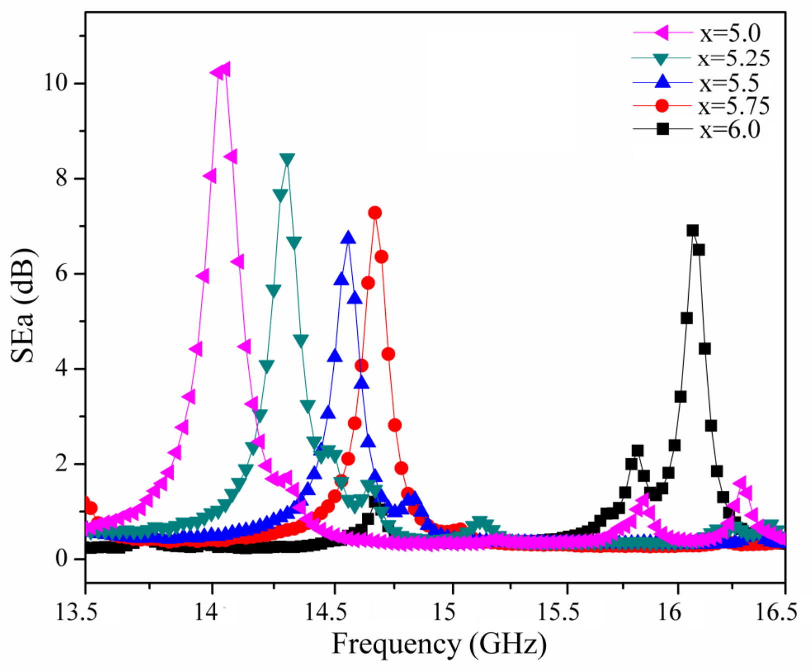

Fig. 4.38. Absorption shielding effectiveness (SE_a) vs frequency plots for BaO.xFe$_2$O$_3$.

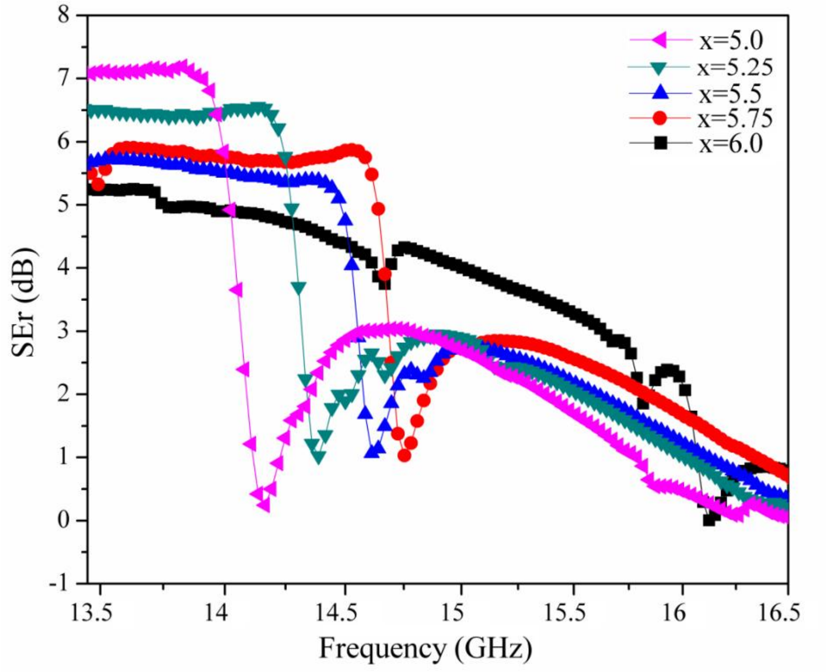

Fig. 4.39. Reflection shielding effectiveness (SE_r) vs frequency plots for BaO.xFe$_2$O$_3$.

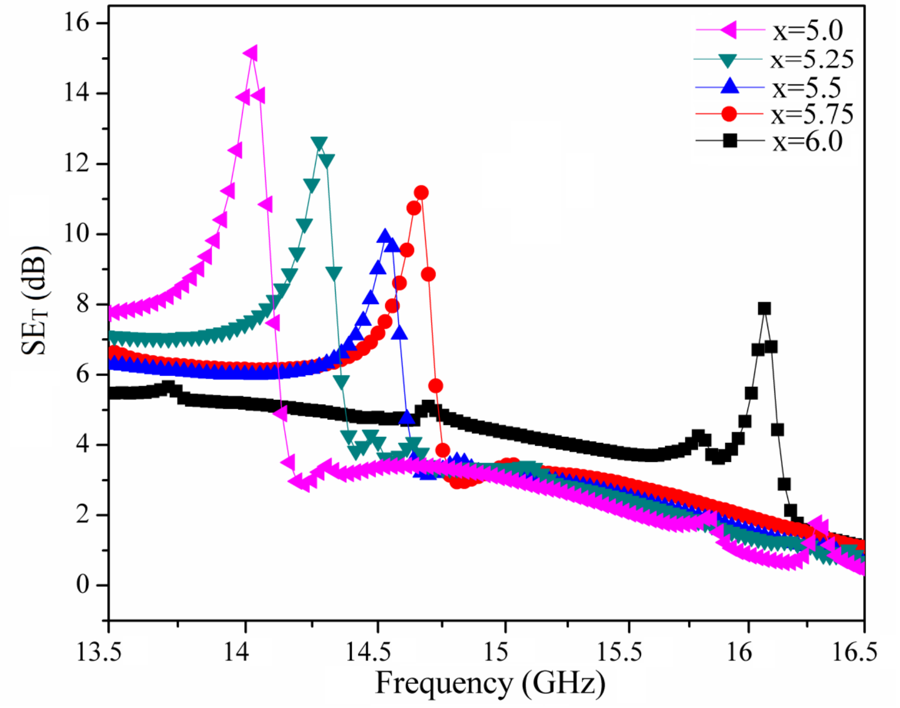

Fig. 4.40. Total shielding effectiveness (SE_t) vs frequency plots for BaO.xFe$_2$O$_3$.

Fig. 4.41 shows the frequency dependent reflection loss (R_L) of the BaM for different Fe/Ba mole ratio in the frequency range of 12-18 GHz. Minimum R_L or a dip in spectra is equivalent to the occurrence of minimal reflection or maximum absorption of microwaves. Absorption spectra show intensity and frequency of R_L increases with the mole ratio. Tunable microwave absorption spectra in the frequency range of 14.1 GHz to 16.2 GHz is observed. R_L found to be varies from -7.4 dB to -29.26 dB with mole ratio. It is noteworthy that in frequency range 16.0 - 16.25 GHz, BaM with mole ratio of 6.0 exhibits a maximum reflection loss of -29.26 dB at 16.12 GHz. This resonance frequency is shifted towards lower frequency from 16.06 GHz to 14.17 GHz with lower Fe/Ba mole ratio, suggesting that by decreasing the Fe/Ba mole ratio, resonance absorption peak can be tuned to lower side of the frequency band.

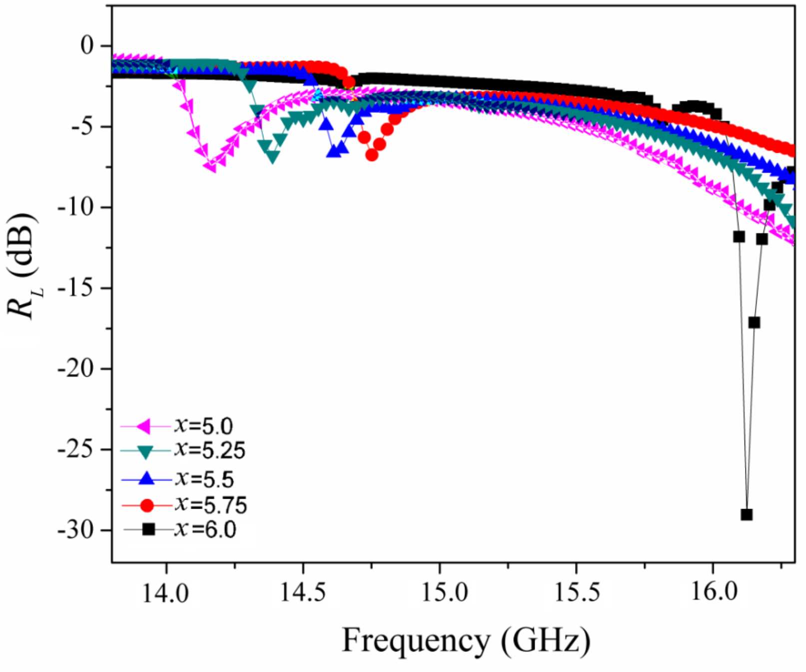

Fig. 4.41. Reflection losses (R_L) vs frequency plots for BaO.xFe$_2$O$_3$.

Chapter 5

CONCLUSIONS

Overview

The present chapter summarizes the results of the various experiments described in the previous chapters. The effect of important process parameters on the magnetic properties of barium hexaferrite is outlined. The influence of Fe/Ba mole ratio, lanthanum and cobalt-titanium substitutions on the magnetic properties of barium hexaferrite powders and films are discussed and tabulated. In the end, the suggestions for further research work in this area are outlined.

In summary, structural and magnetic properties of BaM powders and screen printed thick films are investigated. Firstly, pure BaM powder and films are prepared. The effect various process parameters such as calcinations temperature, milling time and sintering temperature are studied. Secondly, the effect of Fe/Ba mole ratio is studied. Finally, the effect of La^{3+} ion substitution for Ba and Co-Ti ion substitution for Fe site are studied. The conclusions drawn from the work are as follows:

- BaM powders are prepared from solid state synthesis at different calcinations temperature. Single phase BaM are obtained at1200 °C. Calcined powders are further milled for 1 to 8 hours to investigate the effect of particle size on their structural and magnetic properties. XRD patterns confirmed the formation of single phase for upto 3 hour milled sample; however, a minor peak of tungsten carbide (WC) is also observed due to higher milling time. Magnetization and coercivity decreases continuously as milling time increases. One hour milled powder shows maximum magnetization and is found suitable for the preparation of the thick films. BaM films are screen printed and sintered at different temperatures. The dense microstructure with limited porosity is obtained at 1300 °C. Magnetization for BaM films found is to be lower than BaM powders, because of addition of nonmagnetic Bi_2O_3 phase during screen printing.

- Single phase BaM powders and thick films with varying Fe/Ba mole ratio have been successfully prepared. Their structural, magnetic and microwave properties has been investigated. XRD patterns confirms the formation of single phase BaM for $x = 5.5 - 6.0$. However, secondary phase of $BaFe_2O_4$ is also observed for $x =$ 5.25 and 5.0. The formation of $BaFe_2O_4$ suggests that lower Fe/Be mole ratios are not favorable for the formation of single phase BaM. Microstructural feature reveals the densely packed grains with an average grain size of ~3µm. Mössbauer results show that Fe ion vacancy preferably occurred at ($4f_1$, $4f_2$) and $2b$ sites for mole ratio 5.5 and 5.0 respectively. Films with mole ratio 5.5 show the higher value of magnetization and magnetocrystalline anisotropy. Shielding effectiveness (*SE*) and Reflection loss (R_L) results shows that the microwave absorption properties can be tuned in 12-18 GHz frequency range by varying Fe/Ba mole ratio.

- $Ba_{1-x}La_xFe_{12}O_{19}$ (x = 0.0, 0.1 and 0.2) powder has been successfully prepared by solid state reaction method by adopting two different substitution methods. In first method, La^{3+} substituted BaM is directly prepared from Fe_2O_3 and $BaCO_3$ with Fe/Ba molar ratio of 6:1. In the second method, solid state synthesis of Fe_2O_3 and La substituted barium monoferrite ($Ba_{1-x}La_xFe_2O_4$) in molar composition of 5:1 has been adopted. Refined XRD patterns confirmed the formation of single phase barium hexaferrite by both the methods. Mössbauer studies show the increase in hyperfine field for all crystallographic sites. Higher value of isomer shift suggests change in ionic state from Fe^{3+} to Fe^{2+}. Magnetization is found to increase for x = 0.1 and then decreased for x = 0.2. However, the maximum value of magnetization (67.5emu/g) is obtained for the samples prepared by the second method. Coercivity is nearly constant for all the samples. The present experiments suggest an alternative method to develop substituted $BaFe_{12}O_{19}$ with high magnetization. As-prepared powders are further screen printed on alumina substrate to prepare BaM thick films. All films show dense microstructure without any measurable porosity. Magnetization is found to be higher in parallel direction due to higher fraction of parallel aligned grains. Coercivity for La^{3+} substituted films is higher than powder samples due to higher value of magnetocrystalline anisotropy.

- $BaFe_{12-x}Co_xO_{19}$ and $BaFe_{12-x}Ti_xO_{19}$ with (x = 0.0 - 2.0) are prepared from solid state reaction method and their structural and magnetic properties have been investigated. For Co^{2+} substituted BaM powders, a secondary phase of $Ba_2Co_2Fe_{12}O_{22}$ is detected. The magnetization is found to increase from 57.2 emu/g to 59.0 emu/g as x increased from 0.0 to 0.5, and then decreases to 48.4 emu/g for x = 1.0. Increased magnetization suggests that Co^{2+} is substituting at down spin site. Further decrease in magnetization for x = 1.0 - 2.0, is attributed to the presence of less magnetic $Ba_2Co_2Fe_{12}O_{22}$ phase and non-magnetic Fe_2O_3 phase. As concentration of substituted amount increases, intensity of secondary phase increases hence coercivity also decreases. For Ti^{4+} substituted BaM powders, single phase is observed for only for $x = 0.0 - 1.0$. However, for $x = 1.5 - 2.0$, the major phase formed is $Ba_6Fe_{45}Ti_{17}O_{106}$ along with minor BaM and Fe_2O_3 phases. The decrease in magnetization with substitution of Ti^{4+} ions is observed. The decrease in magnetization is attributed due to replacement of Fe^{3+} ions ($5\mu_B$) by Ti^{4+} ions ($0\ \mu_B$). Moreover, the magnetic dilution is also caused due to the presence of paramagnetic phase $Ba_6Fe_{45}Ti_{17}O_{106}$. The decrease in coercivity is observed due to the decrease in magnetocrystalline anisotropy.

- Co-Ti substituted BaM powders are prepared from solid state synthesis method and their structural and magnetic properties have been investigated. XRD patterns confirm the formation of single phase for all the substituted samples. The preferential site occupation of Co^{2+} and Ti^{4+} ion is studied by Mössbauer spectroscopy. It is observed that the Co-Ti ions preferred to occupy the $2b$, $4f_2$ and $12k$, sites. As-prepared powders are further screen printed on alumina substrate to prepare BaM thick films. Drastic decrease in H_c from ~2 kOe to ~ 0.080 kOe is observed, which is attributed to decrease in H_a. M initially increase up $x = 0.5$ and then decreases for $x = 1.0$. Magnetization for BaM films is found to be lower than BaM powders because of addition of nonmagnetic Bi_2O_3 phase during screen printing. M_r also decreased from 34 emu/g ($x = 0.0$) to 4 emu/g ($x = 1.0$). SEM micrographs shows that suitable substitution of Co^{2+} -Ti^{4+} ions promotes hexagonal grains and out-of-plane anisotropy.

- Summary of magnetic properties screen printed BaM thick films prepared from Fe/Ba mole ratio, La^{3+} and Co^{2+}-Ti^{4+} substitution are summarized in **Table 5.1**. Table demonstrate a versatile nature of BaM can be obtained by creating Fe ion vacancy and by substitution for Fe ion, which further drastically reduce or increase the H_a. Variation in H_a thus shifts the operating frequency i.e. FMR frequency of device. The Fe ion vacancy and La substitution allowing for applications from X- to K_u bands, while Co-Ti substitution allowing devices operated at S-, C-,X- to K_u bands.

Table 5.1. Summarized magnetic properties of screen printed BaM thick films for different series.

Series Name	x	M_s **(emu/g)**		M_r **(emu/g)**		H_a **(kOe)**		H_c **(kOe)**	
		(∥)	**(⊥)**	**(∥)**	**(⊥)**	**(∥)**	**(⊥)**	**(∥)**	**(⊥)**
$\mathbf{BaO.}x\mathbf{(Fe_2O_3)}$	5.0	44.4	-	23.2	-	9.3	-	1.9	-
	5.25	47.4	-	24.7	-	9.4	-	1.9	-
	5.5	53.9	-	25.6	-	10.3	-	1.9	-
	5.75	52.5	-	23.8	-	10.2	-	1.7	-
	6.0	52.2	-	29.8	-	9.7	-	2.0	-
$\mathbf{Ba_{1-x}La_xFe_{12}O_{19}}$	0.0	51.4	42.1	28.5	20.1	9.5	9.4	2.0	2.0
	0.1	52.1	51.0	33.2	29.5	10.6	11.3	2.7	2.8
	0.2	44.1	36.3	26.2	19.7	9.8	9.7	2.5	2.5
$\mathbf{BaFe_{12-2x}Co_xTi_xO_{19}}$	0.0	50.9	42.0	28.8	20.1	9.9	9.4	1.9	1.9
	0.25	58.6	50.9	19.6	9.8	9.9	9.5	0.7	0.7
	0.5	58.2	49.7	16.2	7.2	8.7	10.0	0.6	0.6
	0.75	52.8	44.0	10.5	2.8	5.3	6.4	0.2	0.2
	1.0	51.7	47.2	4.6	1.5	4.5	4.4	0.05	0.06

Scope for Future Work

On the basis of work done in the present study the few prospective suggestions for future work are following:

- For the realization of BaM thick films for high frequency applications, ferromagnetic resonance (FMR) measurements need to be investigated.

- The film thickness greatly affects the microwave absorption frequency, therefore the effect of thickness need to be investigated.

- It has been observed that the microstructure of conventionally sintered films is not uniform. Such films have defects such as porosity, grain shape etc. Therefore, microwave sintered thick films has to be processed. Their magnetic and microwave properties of microwave sintered films need to be investigated.

REFERENCES

[1] V.G. Harris, “Modern microwave ferrites”, IEEE Trans. Magn. 48(3) (2012) 1075-1104.

[2] M.P. Horvath, “Microwave applications of soft ferrites”, J. Magn. Magn. Mater. 215 (2000) 171-183.

[3] A. Guennou, P. Queffelec, P. Gelin, J.L. Mattei, “Self-biased *Y*-junction circulators using polycrystalline hexaferrite: An accurate electromagnetic analysis”, J. Appl. Phys. 99 (2006) 08P505-1 - 08P505-3.

[4] J. Wang, A. Geiler, P. Mistry, D.R. Kaeli, V.G. Harris, C. Vittoria, “Design and simulation of self-biased circulators in the ultrahigh frequency band”, J. Magn. Magn. Mater. 324 (2012) 991–994.

[5] O. Akman, H. Kavas, A. Baykal, Z. Durmus, B. Aktas, H. Sozeri, “Microwave absorption properties of $BaFe_{12}O_{19}$-TiO_2 composite coated with conducting polymer”, J. Supercond. Nov. Magn. 26 (2013)1369–1373.

[6] Y.J. Kim, S.S. Kim, “Magnetic and microwave absorbing properties of Ti and Co substituted M-hexaferrites in Ka-band frequencies (26.5~40 GHz)”, J. Electroceram. 24 (2010) 314-318.

[7] Y. Chen, A.L. Geiler, T. Sakai, S.D. Yoon, C. Vittoria, V.G. Harris, “Microwave and magnetic properties of self-biased barium hexaferrite screen printed thick films”, J. Appl. Phys. 99 (2006) 08M904-1 - 08M904-3.

[8] R.C. Pullar, “Hexagonal ferrits: a review of the synthesis, properties and applications of hexaferrite ceramics”, Prog. Mater. Sci. 57 (2012) 1191-1334.

[9] V.G. Harris, A. Geiler, Y. Chen, S.D. Yoon, M. Wu, A. Yang, Z. Chen, P. He, P.V. Parimi, X. Zuo, C.E. Patton, M. Abe, O. Acher and C. Vittoria, “Recent advances in processing and applications of microwave ferrite”, J. Magn. Magn. Mater. 321 (2009) 2035-2047.

[10] H.L. Glass, M.T. Elliott, “Attainment of the intrinsic FMR linewidth in yttrium iron garnet films grown by liquid phase epitaxy”, J. Cryst. Growth. 34 (1976) 285-288.

[11] R.C. Lecraw, E.G. Spencer, C.S. Porter, “Ferromagnetic resonance line width in yttrium iron garnet single crystals”, Phys. Rev. 110(6) (1958) 1311-1313.

[12] S.P. Gairola, V. Verma, V. Pandey, Ravi, L.P. Purohit, R.K. Kotnala, “Modified composition of cobalt ferrite as microwave absorber in x-band frequencies”, Integr. Ferroelectr. 119 (2010)151–156.

[13] S.P. Gairola, V. Verma, A. Singh, L.P. Purohit, R.K. Kotnala, “Modified composition of barium ferrite to act as a microwave absorber in X-band frequencies”, Solid State Commun. 150 (2010) 147-151.

[14] Z.H. Yang, Z.W. Li, L.B. Kong "Structural and magnetic properties of free-standing $Ni_{0.23}Cu_{0.11}Zn_{0.66}Fe_2O_4$, thick films prepared using a modified tape-casting method", J. Magn. Magn. Mater. 322 (2010) 557-561.

[15] C. Liu, B. Zou, A.J. Rondinone, Z.J. Zhang, "Chemical control of superparamagnetic properties of magnesium and cobalt spinel ferrite nanoparticles through atomic level magnetic couplings", J. Am. Chem. Soc. 122 (2000) 6263-6267.

[16] K.T. Han, "The origin of FMR parameter shift in polycrystalline $MgFe_2O_4$ ferrite spheres", Phys. Stat. Sol. (a). 155 (1996) 215-222.

[17] X. Zuo, A. Yang, S.D. Yoon, J.A. Christodoulides, V.G. Harris, C. Vittoria, "Large induced magnetic anisotropy in manganese spinel ferrite films", Appl. Phys. Lett. 87 (2005) 152505-1 - 152505-3.

[18] J.P. Chen, C.M. Sorensen, K.J. Klabunde, G.C. Hadjipanayis, E. Devlin, A. Kostikas, "Size-dependent magnetic properties of $MnFe_2O_4$ fine particles synthesized by coprecipitation", Phys. Rev. B. 54 (1996) 9288-9296.

[19] P.C. Dorsey, P. Lubitz, D.B. Chrisey, J.S. Horwitz, "$CoFe_2O_4$ thick films grown on (100) MgO substrates using pulse laser deposition", J. Appl. Phys. 79 (1996) 6338-6340.

[20] K.P. Chae, J. G. Lee, W. K. Kim, Y. B. Lee, "Magnetic properties of Ti-doped $CoFe_2O_4$ films", J. Magn. Magn. Mater. 248 (2002) 236-240.

[21] H. How, P. Shi, C. Vittoria, L.C. Kempel, K. D. Trott, "Single-crystal YIG phase shifter using composite stripline structure at X band", J. Appl. Phys. 87 (2000) 4966-4968.

[22] H.L. Glass, "Ferrites films for microwave and millimeter wave devices", Proc. IEEE 76 (1988) 151-158.

[23] Y. Chen, T. Sakai, T. Chen, S. D. Yoon, C. Vittoria, V. G. Harris, "Screen printed thick self-biased, low-loss, barium hexaferrite films by hot-press sintering", J. Appl. Phys. 100 (2006) 043907-1 -043907-9.

[24] S. D. Yoon, C. Vittoria, "Microwave and magnetic properties of barium hexaferrite films having the c-axis in the film plane by liquid phase epitaxy technique", J. Appl. Phys. 93 (2003) 8597-8599.

[25] M. Sharma, S.C. Kashyap, H.C. Gupta, M.C. Dimri, K. Asokan, "Enhancement of curie temperature of barium hexaferrite by dense electronic excitations", AIP Adv. 4 (2014) 077129-1 – 077129-7.

[26] A. Ataie, I.R. Harris, C.B. Ponton, "Magnetic properties of hydrothermally synthesized strontium hexaferrite as a function of synthesis conditions", J. Mat. Sci. 30 (1995) 1429-1433.

[27] F. Licci, G. Turilli, T. Besagni, “Phase analysis and single domain detection in hexaferrite powders for magnetic recording”, IEEE Trans. Magn. 24 (1988) 593-597.

[28] J.F. Wang, C.B. Ponton, I.R. Harris, “Ultrafine SrM particles with high coercivity by chemical coprecipitation”, J. Magn. Magn. Mater. 242-245 (2002) 1464-1467.

[29] A.J. Kerecman, T.R. Au Coin, W.P. Dattilo, “Ferromagnetic resonance in $Ba_4Zn_2Fe_{36}O_{60}$ (ZnU) and Mn-substituted ZnU single crystals”, J. Appl. Phys. 40 (1969) 1416-1417.

[30] D. Lisjak, M. Drofenik, “Synthesis and characterization of Zn_2U ($Ba_4Zn_2Fe_{36}O_{60}$) hexaferrite powder”, J. Appl. Phys. 93 (2003) 8011-8013.

[31] R.C. Pullar, A.K. Bhattacharya, “The synthesis and characterisation of Co_2X ($Ba_2Co_2Fe_{28}O_{46}$) and Co_2U ($Ba_4Co_2Fe_{36}O_{60}$) ferrite fibres, manufactured from a sol-gel process”, J. Mater. Sci. 36, (2001) 4805-4812.

[32] G. Xiong, Z.H. Mai, “Preparation and magnetic properties of $Ba_2Co_2Fe_{28}O_{46}$ nanocrystals”, J. Appl. Phys. 88 (2000) 519-523.

[33] M. Obol, X. Zuo, C. Vittoria, “Oriented Y-type hexaferrites for ferrite device”, J. Appl. Phys. 91 (2006) 7616-7619.

[34] S.G. Lee, S.J. Kwon, “Saturation magnetizations and curie temperatures of Co-Zn Y-type ferrites”, J. Mag. Magn. Mat. 153 (1996) 279-284.

[35] Z.W. Li, L. Chen, C.K. Ong, “High-frequency magnetic properties of W-type barium-ferrite $BaZn_{2-x}Co_xFe_{16}O_{27}$ composites”, J. Appl. Phys. 94 (2003) 5918-5924.

[36] W.H. von Aulock (Ed.), A.S. Boxer, J.F. Ollom, R.F. Rauchmiller, “Handbook of microwave ferrite materials”, Academic Press, London, 1965.

[37] K.N. Rozanov, Z.W. Li, L.F. Chen, M.Y. Koledintseva, “Microwave permeability of Co_2Z composites”, J. Appl. Phys. 97 (2005) 013905-1 – 013905-7.

[38] J. Smit, H.P.J. Wijn, “Ferrites: physical properties of ferrimagnetic oxides in relation to their technical applications”, Philips Technical Library, Eindhoven, Netherlands, 1959.

[39] J.L. Snoek, “Magnetic and electrical properties of the binary system $MO.Fe_2O_3$”, Physics. 3 (1936) 463-483.

[40] J.L. Snoek, “Non-metallic magnetic materials for high frequencies”, Philips Tech. Rev. 8 (1946) 353-360.

[41] L. Neel, “Magnetic properties of ferrites: ferrimagnetisms and antiferromagnetisome”, Ann. Phys. 3 (1948) 137-198.

[42] P.W. Anderson, “Antiferromagnetism theory of superexchange interaction”, Phys. Rev. 79, (1950) 350-356.

[43] J.J. Went, G.W. Rathenau, E.W. Gorter, and G. W. van Oosterhout, "Ferroxdurc, a class of new permanent magnet materials," Philips Tech. Rev. 13 (1951) 194-208.

[44] G.H. Jonker, H.P.J.Wijin and P.B.Braum, "Ferroxplana, Hexagonal ferromagnetic iron oxide compounds for very high frequency", Philips Tech. Rev. 18 (1957) 145-157.

[45] C.L. Hogan, "The ferromagnetic farady effect of microwave frequency and its applications – the microwave Gyrator", Bell Syst. Tech. J. 31 (1952) 1-31.

[46] H. Kojima, in: E. P. Wohlfarth (ed.), Fundamental properties of hexagonal ferrites with magnetoplumbite structure, Ferromagnetic Materials, North-Holland publishing company, third edition , ch. 5, 1982, pp. 305-391.

[47] V. Adelskold, Ark. Kemi, Mineral. Geol. 12A, (1938)1-9.

[48] E.W. Gorter, "Saturation magnetization and crystal chemistry of ferrimagnetic oxides", Philips Res. Rep. 9 (1954) 295-298.

[49] P.B. Braun, "The crystal structures of a new group of ferromagnetic compound", Philips Res. Rep. 12 **(**1957) 491-497.

[50] J. A. Kohn, D. W. Eckart, C. F. Cook, Jr., "Crystallography of the hexagonal ferrites", Science 172 (1971) 519-525.

[51] X. Obradors, A. Collomb, M. Pernet, D. Samaras, J. C. Joubert, "X-ray analysis of the structural and dynamic properties of $BaFe_{12}O_{19}$ hexagonal ferrite at room temperature", J. Solid State Chem. 56 (1985) 171-181.

[52] S.M. El-Sayed, T.M. Meaz, M.A. Amer, H.A. ElShersaby, "Magnetic behavior and dielectric properties of aluminum substituted M-type barium hexaferrite," Physica B 426 (2013)137–143.

[53] A.M. Alsmadi, I. Bsoul, S.H. Mahmood, G. Alnawashi, K. Proke, K. Siemensmeyer, Klemke, H. Nakotte, "Magnetic study of M-type doped barium hexaferrite nanocrystalline particles", J. Appl. Phys. 114 (2013) 243910-1 - 243910-8.

[54] M.M. Rashad, I.A. Ibrahim, "Improvement of the magnetic properties of barium hexaferrite nano powders using modified co-precipitation method," J. Mag. Magn. Mat. 323 (2011) 2158–2164.

[55] Y. Liu, M.G.B. Drew, Y. Liu, "Preparation and magnetic properties of barium ferrites substituted with manganese, cobalt and tin", J. Mag. Magn. Mat. 323 (2011) 945-953.

[56] T.T.V. Nga, N.P. Duong, T.D. Hien, "Composition and magnetic studies of ultrafine Al-substituted Sr hexaferrite particles prepared by citrate sol–gel method", J. Mag. Magn. Mat. 324 (2012) 1141–1146.

[57] S.E.M. Ghahfarokhi, F. Ranjbar, M.Z. Shoushtari, "A study of the properties of $SrFe_{12-x}Co_xO_{19}$ nanoparticles", J. Mag. Magn. Mat. 349 (2014) 80–87.

[58] J. Wang, F. Zhao, W. Wu, G. Zhao, "Finite-size scaling relation of the curie temperature in barium hexaferrite platelets", J. Appl. Phys. 110 (2011) 123909-1 - 123909-5.

[59] L. Zhao, X. Lv, Y. Wei, C. Ma, L. Zhao, "Hydrothermal synthesis of pure $BaFe_{12}O_{19}$ hexaferrite nanoplatelets under high alkaline system", J. Mag. Magn. Mat. 332 (2013) 44-47.

[60] H. Pfeiffer, R.W. Chantrell, P. Görnert, W. Schüppel, E. Sinn, M. Rösler, "Properties of barium hexaferrite powders for magnetic recording", J. Mag. Magn. Mat. 125(3) (1993) 373-376.

[61] V.N. Dhage, M.L. Mane, A.P. Keche, C.T. Birajdar, K.M. Jadhav, "Structural and magnetic behavior of aluminium doped barium hexaferrite nanoparticles synthesized by solution combustion technique", Physica B 406 (2011) 789-793.

[62] L. Wang, Q. Zhang, "Effect of Fe^{3+}/Ba^{2+} mole ratio on the phase formation and microwave properties of $BaFe_{12}O_{19}$ prepared by citrate–EDTA complexing method", J. Alloys and Compd. 469 (2009) 251-257.

[63] S.R. Janasi, M. Emura, F.J.G. Landgraf, D. Rodrigues, "The effects of synthesis variables on the magnetic properties of coprecipitated barium ferrite powders", J. Magn. Magn. Mater. 238 (2002) 168-172.

[64] A. Mali, A. Ataie, "Influence of Fe/Ba molar ratio on the characteristics of Ba-hexaferrite particles prepared by sol–gel combustion method", J. Alloys Compd. 399 (2005) 245-250.

[65] W.T. Liu, J.-M. Wu, "The effect of the vacuum extraction and the Fe/Ba ratio on the phase formation of barium ferrite thin film synthesized by sol–gel method", Mater. Chem. Phys. 69 (2001) 148-153.

[66] M. Jean, V. Nachbaur, J. Bran, J.M.L. Breton, "Synthesis and characterization of $SrFe_{12}O_{19}$ powder obtained by hydrothermal process", J. Alloys and Compd. 496 (2010) 306-312.

[67] S. Verma, P. Sharma , O.P. Pandey , A. Paesano Jr., A.C. Sun, "Structure and Magnetic Properties of $Ba_{1-x}La_xFe_{12}O_{19}$ Prepared by $Ba_{1-x}La_xFe_2O_4$", IEEE Trans. Magn. 50(1) (2014) 2101004-1 - 2101004 -3.

[68] R. Grössinger, M. Kupferling, J. C. Tellez Blanco, G. Wiesinger, M. Müller, G. Hilscher, M.W. Pieper, J.F. Wang, I.R. Harris, "Rare Earth Substitutions in M-Type Ferrites", IEEE Trans. Magn. 39(5) (2003) 2911-2913.

[69] F. Lotgering, "Magnetic anisotropy and saturation of $LaFe_{12}O_{19}$ and some related compounds", J. Phys. Chem. Solids. 35 (1974) 1633-1639.

[70] M. Küpferling, R. Grössinger, M.W. Pieper, G. Wiesinger, H. Michor, "Structural phase transition and magnetic anisotropy of La-substituted M-type Sr hexaferrite", Phy. Rev. B. 73 (2006)144408-1 – 144408-11.

[71] X. Liu, W. Zhong, S. Yang, Z. Yu, B. Gu, Y. Du, "Influences of La^{3+} substitution on the structure and magnetic properties of M-type strontium ferrites," J. Magn. Magn. Mater. 238 (2002) 207-214.

[72] X. Liu, W. Zhong, S. Yang, Z. Yu, B. Gu, Y. Du, " Structure and magnetic properties of La^{3+}-substituted strontium hexaferrite particles prepared by Sol–Gel method", Phys. stat. sol. (a). 193(2) (2002) 314-319.

[73] D. Seifert, J. Topfer, F. Langenhorst, J. M. Le Breton, H. Chiron, L. Lechevallier, "Synthesis and magnetic properties of La-substituted M-type Sr hexaferrites", J. Magn. Magn. Mater. 321 (2009) 4045-4051.

[74] F. Hu, L.F. Garcia, X.S. Liu, D.R. Zhu, M. Suarez, J.L. Menendez, "A strong magneto-optical activity in rare-earth La^{3+} substituted M-type strontium ferrites", J. Appl. Phys. 109 (2011) 113906-1 -113906-5.

[75] P. Novak, K. Knizek, M. Kupferling, R. Grossinger, M.W. Pieper, "Magnetism of mixed valence (LaSr) hexaferrites", Eur. Phys. J. B 43 (2005) 509–515.

[76] S. Ounnunkad, P. Winotai, S. Phanichphant, "Effect of La doping on structural, magnetic and microstructural properties of $Ba_{1-x}La_xFe_{12}O_{19}$ ceramics prepared by citrate combustion process", J. Electroceram. 16 (2006) 357–361.

[77] S. Ounnunkad, "Improving magnetic properties of barium hexaferrite by La or Pr substitution", Solid State Commun. 138 (2006) 472- 475.

[78] T.T.V. Nga, N.P. Duong, T.D. Hien, "Enhancement of magnetic properties of La-substituted strontium hexaferrite particles prepared by sol-gel route", Commun. Phys. 20 (2) (2010)137-142.

[79] H. Sozeri, I. Kucuk, H. Ozkan, "Improvement in magnetic properties of La substituted $BaFe_{12}O_{19}$ particles prepared with an unusually low Fe/Ba molar ratio", J. Mag. Magn. Mat. 323 (2011) 1799-1804.

[80] M.W. Pieper, M. Kupferling, I.R. Harris, J.F. Wang, "Large polarons in rare-earth doped hexaferrites observed by NMR", J. Mag. Magn. Mat. 272-276 (2004) 2219-2220.

[81] L. Lechevallier, J.M. Le Breton, "Substitution effects in M-type hexaferrite powders investigated by mössbauer spectrometry", J. Mag. Magn. Mat. 290-291 (2005) 1237-1239.

[82] L. Lechevallier, J.M. Le Breton, J.F. Wang, I.R. Harris, "Structural analysis of hydrothermally synthesized $Sr_{1-x}Sm_xFe_{12}O_{19}$ hexagonal ferrites", J. Mag. Magn. Mat. 269 (2004) 192-196.

[83] J. Jalli, Y.K. Hong, S.H. Gee, S. Bae, J. Lee, J.C. Sur, G.S. Abo, A. Lyle, S.I. Lee, H. Lee, T. Mewes, "Magnetic and microwave properties of Sm-doped $SrFe_{12}O_{19}$ single crystals", IEEE Trans. Magn. 44 (11) (2008) 2978- 2981.

[84] W. Lixi, H. Qiang, M. Lei, Z.H. Qitu, "Influence of Sm^{3+} substitution on microwave magnetic performance of barium hexaferrites", J. Rare. Earth. 25 (2007) 216-219.

[85] G. Litsardakis, I. Manolakis, C. Serletis, K.G. Efthimiadis, "Structural and magnetic properties of barium-gadolinium hexaferrites", J. Mag. Magn. Mat. 310 (2007) 884-886.

[86] G. Litsardakis, I. Manolakis, C. Serletis, K.G. Efthimiadis, "Effect of Gd substitution on structural and magnetic properties of strontium hexaferrites", J. Mag. Magn. Mat. 316 (2007) 170-173.

[87] G. Litsardakis, I. Manolakis, C. Serletis, K. G. Efthimiadis, "High coercivity Gd-substituted Ba hexaferrites, prepared by chemical coprecipitation", J. Appl. Phys. 103 (2008) 07E501-1 - 07E501-3.

[88] G. Litsardaki, I. Manolakis, A.C. Stergiou, C. Serletis, K.G. Efthimiadis, "New Dy-substituted Ba hexaferrites with high coercivity", IEEE Trans. Magn. 44(11) (2008) 4222 - 4224.

[89] C.A. Stergiou, I. Manolakis, T.V. Yioultsis, G. Litsardakis, "Dielectric and magnetic properties of new rare-earth substituted Ba- hexaferrites in the 2–18 GHz frequency range", J. Mag. Magn. Mat. 322 (2010) 1532-1535.

[90] C. Ju Li, B. Huang, J. Na Wang, "Effect of aluminum substitution on microstructure and magnetic properties of electrospun $BaFe_{12}O_{19}$ nanofibers", J. Mater. Sci. 48 (2013)1702–1710.

[91] P. Sharma, R.A. Rocha, S.N. Medeiros, B. Hallouche, A. Paesano Jr., "Structural and magnetic studies on mechanosynthesized $BaFe_{12-x}Mn_xO_{19}$", J. Mag. Magn. Mat. 316 (2007) 29–33.

[92] Sh. Sh. Bashkirov, A.B. Liberman, A.A. Valiullin, L.D. Zaripova, S.V. Kokin, "Effect of Mn^{2+} ions on the magnetic microstructure of hexaferrites," Phys. Solid State. 42(1) (2000) 79–83.

[93] T. Tsutaoka, N. Koga, "Magnetic phase transitions in substituted barium ferrites $BaFe_{12-x}(Ti_{0.5}Co_{0.5})_xO_{19}$ (x = 0–5)," J. Mag. Magn. Mat. 325 (2013) 36–41.

[94] J. Qiu, Q. Zhang, M. Gu, H. Shen, "Effect of aluminum substitution on microwave absorption properties of barium hexaferrite", J. Appl. Phys. 98 (2005) 103905-1-103905-5.

[95] D. Mishra, S. Anand, R.K. Panda, R.P. Das, "X-ray diffraction studies on aluminum-substituted barium hexaferrite", Mater Lett. 58 (2004) 1147– 1153.

[96] J.C.F. Gandarilla, S. DmHaz-Castanon, N.S. Almodovar, “Activation volume and coercivity in aluminum-substituted Pb-M hexaferrites”, J. Mag. Magn. Mat. 222 (2000) 271-276.

[97] O. Mohanta, Y.N. Singhbabu, S.K. Giri, D. Dadhich, N.N. Das, R.K. Sahu, “Degradation of congo red pollutants using microwave derived $SrFe_{12}O_{19}$: An efficient magnetic photocatalyst under visible light”, J. Alloys and Compd. 564 (2013) 78-83.

[98] C.Ju Li, B.N. Huang, J.Na Wang, “Effect of aluminum substitution on microstructure and magnetic properties of electrospun $BaFe_{12}O_{19}$ nanofibers”, J. Mater. Sci. 48 (2013)1702-1710.

[99] M. Liu, X. Shen, F.Song, J. Xiang, X. Meng, “Microstructure and magnetic properties of electrospun one-dimensional Al^{3+} substituted $SrFe_{12}O_{19}$ nanofibers”, J Solid State Chem. 184 (2011) 871-876.

[100] P. Wartewig, K. Melzer, M. Krause, R. Tellgren, “Cation distribution and magnetic structure of some substituted barium hexaferrites”, J. Magn. Magn. Mater. 140-144 (1995) 2101-2102.

[101] S. Ounnunkad, P. Winotaib, “Properties of Cr-substituted M-type barium ferrites prepared by nitrate–citrate gel-auto combustion process”, J. Magn. Magn. Mater. 301 (2006) 292–300.

[102] M.V. Bukhtiyarova, A.S. Ivanova, E.M. Slavinskaya, L.M. Plyasova, V.A. Rogov, V.V. Kaichev, A.S. Noskov, “Catalytic combustion of methane on substituted strontium ferrites”, Fuel 90 (2011) 1245–1256.

[103] T.T.V. Nga, T.D. Hien, N.P. Duong, T.D. Hoang, “Structural and magnetic properties of $SrLa_xFe_{12-x}O_{19}$ ($x = 0 - 0.15$) prepared by using a sol-gel method”, J. Korean. Phys. Soc. 52(5) (2008)1474-1477.

[104] C. Doroftei, E. Rezlescu, P. D. Popa, N. Rezlescu, “The influence of the technological factors on strontium hexaferrites with lanthanum substitution prepared by self-combustion method”, J. Optoelectron. Adv. 8(3) (2006) 1023 – 1027.

[105] G.M. Rai, M.A. Iqbal, K.T. Kubra, “Effect of Ho^{3+} substitutions on the structural and magnetic properties of $BaFe_{12}O_{19}$ hexaferrites”, J. Alloys and Compd. 495 (2010) 229 - 233.

[106] A. Thakur, R.R. Singh, P.B. Barman, “Structural and magnetic properties of La^{3+} substituted strontium hexaferrite nanoparticles prepared by citrate precursor method”, J. Magn. Magn. Mater. 326 (2013) 35–40.

[107] Sharad N. Sablea, Kishor G. Rewatkar, Vivek M. Nanoti, “Structural and magnetic behavioral improvisation of nanocalcium hexaferrites,” Mat. Sci. Eng. B. 168 (2010) 156–160.

[108] F. Tabatabaie, M.H. Fathi, A. Saatchi, A. Ghasemi, “Effect of Mn–Co and Co–Ti substituted ions on doped strontium ferrites microwave absorption”, J. Alloys and Compd. 474 (2009) 206–209.

[109] M.J. Iqbal, M.N. Ashiq, “Comparative studies of $SrZr_xMn_xFe_{12-2x}O_{19}$ nanoparticles synthesized by co-precipitation and sol–gel combustion methods,” Scr. Mater. 56 (2007) 145-148.

[110] A.G. Angeles, G.M. Suarez, A. Gruskova, J. Lipka, M. Papanova, J. Slamad, “Effect of (Ni, Zn)Ru mixtures on magnetic properties of barium hexaferrites yielded by high-energy milling,” J. Magn. Magn. Mater. 285 (2005) 450 - 455.

[111] J. Lee, Y.K. Hong,W. Lee, G.S. Abo, J. Park, N. Neveu, W.M. Seong, S.H. Park, W.K. Ahn, “Soft M-type hexaferrite for very high frequency miniature antenna applications”, J. Appl. Phys. 111 (2012) 07A520-1 - 07A520-3.

[112] J Smit, FK Lotgering, U Enz, “Anisotropy properties of hexagonal”, J Appl. Phys. Suppl. 31 (1960) 137S-141S.

[113] O. Kubo, T. Ido, H. Yokoyama, “Properties of Ba ferrite particles for perpendicular magnetic recording media”, IEEE Trans. Magn. Magn. 18 (1982) 1122-1124.

[114] V. Pankov, “Modified aerosol synthesis for nanoscale hexaferrite particles preparation”, Mat. Sci. Eng. A. 224 (1997) 101-106.

[115] S. Thompson, N.J. Shirtcliffe, E.S.O. Keefe, S. Appleton, C.C. Perry, “Synthesis of $SrCo_xTi_xFe_{(12-2x)}O_{19}$ through sol–gel auto-ignition and its characterization”, J. Magn. Magn. Mater. 292 (2005) 100–107.

[116] N. Koga, T. Tsutaoka, “Preparation of substituted barium ferrite $BaFe_{12-x}(Ti_{0.5}Co_{0.5})_xO_{19}$ by citrate precursor method and compositional dependence of their magnetic properties”, J. Magn. Magn. Mater. 313 (2007) 168–175.

[117] I. Bsoul, “Preparation of nanocrystalline $BaFe_{12-2x}Co_xTi_xO_{19}$ by ball milling method and their magnetic properties”, Jordan. J. phys. 2(2) (2009) 95-102.

[118] D. Chen, Y. Liu, Y. Li, W. Zhong, H. Zhang, “ Microstructural and magnetic properties of low temperature sintered CoTi-substituted barium ferrite for LTCC applications”, J. Magn. Magn. Mater. 323 (2011) 2837-2840.

[119] J. Kreisel, H. Vincent, F. Tasset, M. Pate, J.P. Ganne, “An investigation of the magnetic anisotropy change in $BaFe_{12-2x}Ti_xCo_xO_{19}$ single crystals”, J. Magn. Magn. Mater. 224 (2001) 17-29.

[120] Y. Guan, Y. Lin, L.Zou, Q. Miao, M. Zeng, Z. Liu, X. Gao, J. Liu, “The effects of Co-Ti co-doping on the magnetic, electrical and magnetodielectric behaviors of M-type barium hexaferrites”, AIP Adv. 3 (2013) 122115-1 – 122115-6.

[121] J. Lee, Y.K. Hong, W. Lee, G.S. Abo, J. Park, W.M. Seong, W.K. Ahn, “Control of magnetic tangent of hexaferrite for advanced radio frequency antenna applications”, J. Appl. Phys. 113 (2013) 073909-1-073909-6.

[122] Y.J. Kim, S.S Kim, “Magnetic and microwave absorbing properties of Ti and Co substituted M-hexaferrite in K_a band frequencies (26.5-40 GHz)”, J. Electroceram. 24 (2010) 314-318.

[123] C. Dong, X. Wang, P. Zhou, T. Liu, J. Xie, L. Deng, “Microwave magnetic and absorption properties of M-type ferrite $BaCo_xTi_xFe_{12-2x}O_{19}$ in the K_a band”, J. Magn. Magn. Mater. 354 (2014) 340-344.

[124] P. Dorsey, R. Seed, C. Vittoria, C. A. Carosella, D. B. Chrisey, P. Lubitz, J. S. Horwitz, “Pulse laser deposition of epitaxial $BaFe_{12}O_{19}$ thin films”, J. Appl. Phys. 71 (10) (1992) 5107-5110.

[125] P. Shi, S. D. Yoon, X. Zuo, I. Kozulin, S. A. Oliver and C. Vittoria, “Microwave properties of pulsed laser deposited Sc-doped barium hexaferrite films”, J. Appl. Phys. 87(91) (2000) 4981-4983.

[126] S.D. Yoon, C. Vittoria, S.A. Oliver, “Magnetization behavior of scandium-substituted barium hexaferrite films having uniaxial axis in the film plane”, J. Magn. Magn. Mater. 265 (2003) 130–137.

[127] S.A. Oliver, S.D. Yoon, I. Kozulin, M.L. Chen,C. Vittoria, “Growth and characterization of thick oriented barium hexaferrite films on MgO (111) substrates”, Appl. Phys. Lett. 76(24) (2000) 3612-3614.

[128] S.D. Yoon, P. Shi, X. Zuo, S.A. Oliver, “Ferrimagnetic resonance line widths of thick barium hexaferrite films on MgO (111)”, IEEE Trans. Magn. 37(4) (2001) 2383-2385.

[129] S. D. Yoon, C. Vittoria, S. A. Oliver, “Magnetic and microwave magnetic properties of barium hexaferrite permanent magnet films having the c-axis in the film plane”, J. Appl. Phys. 93 (71) (2003) 4023 - 4026.

[130] Z. Chen, A. Yang, S. D. Yoon, K. Ziemer, C. Vittoria, and V. G. Harris, “Growth of Ba-hexaferrite films on single crystal 6-H SiC”, J. Magn. Magn. Mater. **301** (2006) 166-170.

[131] Z. Chen, A. Yang, A. Gieler, V.G. Harris, C. Vittoria, P.R. Ohodnicki, K.Y. Goh, M.E. McHenry, Z. Cai, T.L. Goodrich, K.S. Ziemera, “Epitaxial growth of M-type Ba-hexaferrite films on MgO(111)‖SiC (0001) with low ferromagnetic resonance linewidths”, Appl. Phys. Lett. 91 (2007)182505-1 – 182505-3.

[132] Z. Chen, A.Yang, C. Xie, Q. Yang, C. Vittoria, V.G. Harris, “High-rate reactive ion etching of barium hexaferrite films using optimal CHF_3/SF_6 gas mixtures”, Appl. Phys. Lett. 94 (2009) 112505-1 – 112505-3.

[133] Y.Y. Song, J. Das, P. Krivosik, N. Mo, C.E. Patton, “Electric field tunable 60 GHz ferromagnetic resonance response in barium ferrite-barium strontium titanate multiferroic heterostructures”, Appl. Phys. Lett. 94 (2009) 182505-1 -182505-3.

[134] J.C.F. Gandarilla , S. D. Castanon, F. Leccabue, B.E. Watts, “Magnetic properties of polycrystalline Sr–M and Pb–M hexaferrites thin films grown by pulsed laser deposition on Si/SiO_2 substrates”, J. Alloys and Compd. 369 (2004) 195–197.

[135] R. Atkinson , P. Papakonstantinou, I. W. Salter, R. Gerber, “Optical and magneto-optical properties of Co-Ti-substituted barium hexaferrite single crystals and thin films produced by laser ablation deposition”, J. Magn. Magn. Mater. 138 (1994) 222-231.

[136] O. Heczko, R. Gerber, Z. Simsa, “Structural, magnetic and magneto-optical properties of $SrFe_{12-x}Al_xO_{19}$ hexaferrite thin films prepared by laser ablation deposition”, Thin Solid Films 358 (2000) 206 – 214.

[137] S. Anjum, M.S. Rafique, M.K. Rahman, K. Siraj, A. Usman, S.I. Hussain, S. Naseem, “Investigation of induced parallel magnetic anisotropy at low deposition temperature in Ba-hexaferrites thin films”, J. Magn. Magn. Mater. 324 (2012) 711–716.

[138] A. Lisfi, J.C. Lodder, E.G. Keim, C.M. Williams, “Evidence of stress anisotropy and role of oxygen pressure in growth of pulsed-laser-deposited hexaferrite films”, Appl. Phys. Lett. 82 (16) (2003) 76-78.

[139] S.M. Masoudpanah, S. A. Seyyed Ebrahimi, C. K. Ong, “Microstructure and magnetic properties of La-Co substituted strontium hexaferrite films prepared by pulse laser deposition”, J. Magn. Magn. Mater. 342 (2013) 134 - 138.

[140] S.M. Masoudpanah, S.A.S. Ebrahimi, C.K. Ong, “ Preparation of strontium hexaferrite film by pulse laser deposition with in situ heating and post annealing”, J. Magn. Magn. Mater. 324 (2012) 2894 - 2898.

[141] S.M. Masoudpanah, S.A. Seyyed Ebrahimi, C.K. Ong, “Comparision of the microstructure and magnetic properties of strontium hexaferrite deposited on Al_2O_3 (0001), Si (100)/Pt(111) and Si(100) substrates by pulse laser technique”, J. Mag. Magn. Mat. 350 (2014) 81 - 85.

[142] R. Karim, C. Vittoria, “The engineering of ferrite films at the atomic scale”, J. Magn. Magn. Mater. 167(1-2) (1997) 27 - 33.

[143] A.L. Geiler, Y. He, S.D. Yoon, A. Yang, Y. Chen, V. G. Harris, C. Vittoria, “Epitaxial growth of $PbFe_{12}O_{19}$ thin films by alternating target laser ablation deposition of Fe_2O_3 and PbO”, J.Appl. Phys. 101 (2007) 09M510-1 – 09M510-3.

[144] A.L. Geiler, S.D. Yoon, Y. Chen, A. Yang, C. N. Chinnasamy, M. Geiler, V. G. Harris, C. Vittoria, “Alternating target laser ablation deposition of high quality barium hexaferrite thin films from barium monoferrite and hematite targets”, J. Appl. Phys. 103 (2008)07B914-1 – 07B914-3.

[145] M. Mohebbi, K. Ebnabbasi, C. Vittoria, "In-situ deposition of C-axis orientaed barium ferrite films for microwave applications", IEEE Trans. Magn. 49(7) (2013) 4207-4209.

[146] H. Hegde, P. Samarasekara, F.J. Cadieu, "Nonepitaxial sputter synthesis of aligned strontium hexaferrite, SrO.6(Fe_2O_3), films", J. Appl. Phys. 75 (10) (1994) 6640 - 6642.

[147] S. H. Gee, Y. K. Hong, D. W. Erickson, T. Tanaka, and M. H. Park, " Ex situ annealing method for c-axis oriented barium ferrite thick films", J. Appl. Phys. 93(10) (2003) 7507 – 7509.

[148] S. Capraro, M. Le Berre, J.P. Chatelon, H. Joisten, E. Mery, B. Bayard, J.J. Rousseau, D. Barbier, "Properties of barium ferrite sputtered films", Sens. Actuators.113 (2004) 382 – 386.

[149] S. Capraro, J.P. Chatelon, M. Le Berre, H. Joisten, T. Rouiller, B. Bayard, D. Barbier, J.J. Rousseau, "Barium ferrite thick films for microwave applications", J. Magn. Magn. Mater. 272–276 (2004) 1805 –1806.

[150] A.S. Dehlinger, M. Le Berre, B. Canut, J.P.Chatelon, D.Albertini, S.Perrot, D. Givord, J.J.Rousseau, "Microstructural and magnetic properties of thick ($\geq$ 10 μm) magnetron sputtered barium ferrite films", J. Magn. Magn. Mater. 322 (2010) 3293–3297.

[151] K.K. Mallick, P. Atanasov, R.J. Green, "Magnetic properties of cobalt substituted M-type barium hexaferrite prepared by co-precipitation", J. Magn. Magn. Mater. 312 (2007) 418-429.

[152] H. Xu, W. Zhang, B. Peng, W. Zhang, "Properties of barium hexaferrite thin films dependent on sputtering pressure," Appl. Surf. Sci. 257 (2011) 2689 – 2693.

[153] Z. L. Zhuang, M. Rao, R.M. White, "Barium ferrite thin film media with perpendicular c-axis orientation and small grain size", J Appl. Phys. 87(9) (2000) 6370-6372.

[154] A. Morisako, M.Matsuioto, M. Nao, "Influences of sputtering gas pressure on microtexture and crystallographic characteristics of Ba-ferrite thin films for high density recording media" , IEEE Trans. Magn MAG.33 (1) (1987) 56-58.

[155] A. Morisako, M.Matsuioto, M. Nao, "The effect of oxygen gas pressure on Ba-ferrite sputtered films for perpendicular magneticrecording media", IEEE Trans. Magn. 24 (6) (1988) 3024-3026.

[156] Z. Xu, Z. Lan, K. Sun, R. Guo, Z.Yu, X. Jiang, "Properties of Ba-hexaferrite thin films with different thickness", Appl. Surf. Sci. 271 (2013) 362 – 368.

[157] E. Lacroix, P. Gerard, G. Marest, M. Dupuy, "Substrate effects on the crystalline orientation of barium hexaferrite films", J. Appl. Phys. 69 (8) (1991) 4770 – 4772.

[158] X. Sui, M.H. Keyder, “Magnetic easy axis randomly in-plane oriented barium hexaferrite thin film media”, Appl. Phys. Lett. 63(11) (1993) 1582 – 1584.

[159] M. Gomi, J. Cho and M. Abe, “Microstructure and magneto-optical properties of Pr–Ni substituted Ba hexaferrite films prepared by sputtering”, J. Appl. Phys. 82 (10) (1997) 5126 – 5131.

[160] F. Ohmi, A. Watada, I. Miyamoto And Y. Kaneko, “The preparation of Co-Ti substituted Ba-ferrite films”, Appl. Surf. Sci. 33-34 (1988) 646-653.

[161] L. Zhang, X.D. Su, Y. Chen, Q.F. Li and V.G. Harris, “Radio-frequency magnetron sputter-deposited barium hexaferrite films on Pt-coated Si substrates suitable for microwave applications”, Scr. Mater. 63 (2010) 492–495.

[162] A. Kaewrawang, G. Ishida, X. Liu, A. Morisako, “Epitaxial growth of SrM(00) film on Au(111)”, IEEE Trans. Magn. 44(11) (2008) 2899 – 2902.

[163] S. Salemizadeh, S.A. Seyyed Ebrahimi, S.M. Masoudpanah, “The effect of amorphous Al_2O_3 underlayer on the microstructure and magnetic properties of $BaFe_{12}O_{19}$ thin films”, J. Magn. Magn. Mater. 343 (2013) 82 - 85.

[164] R. Hajndl, J. Sanders, H. Srikanth, N.J. Dudney, “Growth and characterization of BSTO/hexaferrite composite thin films”, J. Appl. Phys. 93 (10) (2003) 7999 – 8001.

[165] S. Srinath, N. A. Frey, R. Heindl, H. Srikantha, K. R. Coffey, N. J. Dudney, “Growth and characterization of sputtered BSTO/BaM multilayers”, J. Appl. Phys. 97 (2005) 10J115-1 – 10J115-3.

[166] G. Srinivasan, I. V. Zavislyak, and A. S. Tatarenko, “Millimeter-wave magnetoelectric effects in bilayers of barium hexaferriteand lead zirconate titanate”, Appl. Phys. Lett. 89 (2006)152508-1 – 152508-3.

[167] A.B. Ustinov, A.S. Tatarenko, G. Srinivasan, A. M. Balbashov, “Al substituted Ba-hexaferrite single-crystal films for millimeter-wave devices”, J. Appl. Phys. 105 (2009) 023908-1 – 023908-4.

[168] M. Popov, I. Zavislyak, A. Ustinov and G. Srinivasan, “Sub-terahertz magnetic and dielectric excitations in hexagonal ferrites,” IEEE Trans. Magn. 47(2), (2011) 289-294.

[169] S.G. Pavlova, A.M. Balbashov, L.N Rybina, “Single crystal growth from the melt and magnetic properties of hexaferrites-aluminates”, J. Cryst. Growth. 351 (2012) 161-164.

[170] R.C. Linares, “Epitaxial growth of narrow linewidth yttrium iron garnet film”, J. Cryst. Growth. 3-4 (1968) 443 - 446.

[171] S.G. Wang, S. D. Yoon, and C. Vittoria, “Microwave and magnetic properties of double-sided hexaferrite films on (111) magnesium oxide substrates”, J. Appl. Phys. 92 (11) (2002) 6728 - 6732.

[172] S.D. Yoon, C. Vittoria, “Microwave and magnetic properties of barium hexaferrite films having the c-axis in the film plane by liquid phase epitaxy technique”, J. Appl. Phys. 93(10) (2003) 8597 – 8599.

[173] S. D. Yoon and C. Vittoria, “Thick M-type barium hexaferrite films grown on garnet substrates”, J. Appl. Phys. 96(4) (2004) 2131– 2135.

[174] S.D. Yoon, C. Vittoria**, “**Preparation of thick M-type barium hexaferrite films on double side of substrates by liquid-phase epitaxy deposition technique”, J. Magn. Magn. Mater. 272–276 (2004) 1833–1834.

[175] M.S. Yuan, H.L. Glass. I.R. Adkins, “Epitaxial barium hexaferrite on sapphire by sputter deposition”, Appl. Phys. Lett. 53 (4) (1988) 340 – 341.

[176] M. Verite, M. Valetas, A. Bessaudou, F. Cosset, J.C. Vareille, “Properties of barium hexaferrite thick films deposited by electron beam evaporation”, J. Eur. Ceram. Soc. 25 (2005) 1689-1695.

[177] I. Wane, A. Bessaudou, F. Cosset, A. Celerier, C. Girault, J.L. Decossas, J.C. Vareille, “Thick barium hexaferrite (Ba-M) flms prepared by electron-beam evaporation for microwave application”, J. Magn. Magn. Mater. 211 (2000) 309-313.

[178] S. Salemizadeh and S. A. Seyyed Ebrahimi, “magnetic properties of nanocrystalline barium hexaferrite thin films prepared by sol-gel method”, IEEE Trans. Magn. 45(6) (2009) 2538 – 2540.

[179] A. Ghasemi, V. Sepelak, “Correlation between site preference and magnetic properties of substituted strontium ferrite thin films”, J. Magn. Magn. Mater. 323 (2011) 1727–1733.

[180] S.M. Masoudpanah, S.A. Seyyed Ebrahimi, “Synthesis and characterization of nanostructure strontium hexaferrite thin films by the sol-gel method”, J. Magn. Magn. Mater. 324 (2012) 2239 – 2244.

[181] S.M. Masoudpanah, S.A. Seyyed Ebrahimi, “Effect of citric acid content on the structural and magnetic properties of $SrFe_{12}O_{19}$ thin films”, Thin Solid Films. 520 (2011) 199 – 203.

[182] S.M. Masoudpanah, S. A. Seyyed Ebrahimi,“Effect of pH value on the structural and magnetic properties of nano crystalline strontium hexaferrite thin films”, J. Magn. Magn. Mater. 323 (2011) 2643–2647.

[183] Ali Ghasemi, “ Development of uniaxial magnetocrystalline anisotropy in $SrFe_{12-x}(DyGd)_xO_{19}$ thin film synthesized by incorporation of high coercivity nanoparticles in sol-gel method”, J. Magn. Magn. Mater. 361 (2014) 112 – 117.

[184] J. Bursik, Z. Simsa, M. Cernansky, “Magneto-optical characteristics of Co, Ti-substituted barium hexaferrite films deposited by the dip-coating method”, J. Sol-Gel Sci. Technol. 8 (1997) 947-951.

[185] D.V. Ruikar, P.B. Kashid, V.R. Patil, Vijaya Puri, “Synthesis, characterization and microwave properties of strontium hexaferrite thin films prepared by chemical bath deposition”, Appl. Surf. Sci. 265 (2013) 475– 479.

[186] Z. Cai, T L Goodrich, B Sun, Z Chen, V G Harris and K S Ziemer, “ Epitaxial growth of barium hexaferrite film on wide bandgap semiconductor 6H–SiC by molecular beam epitaxy,” J. Phys. D: Appl. Phys. 43 (2010) 095002-1 – 095002-9.

[187] V. K. Lazarov, P. J. Hasnip, Z. Cai, K. Yoshida, K. S. Ziemer, “ Growth and interface phase stability of barium hexaferrite films on SiC (0001),” J. Appl. Phys. 109 (2011) 07E520-1 – 07E520-3.

[188] D. Lisjak, K. Bobzin, K. Richardt, M. Bégard , G. Bolelli, L. Lusvarghi, A. Hujanen, P. Lintunen, M. Pasquale, E. Olivetti, M. Drofenik, T. Schläfer, “Preparation of barium hexaferrite coatings using atmospheric plasma spraying,” J. Eur. Ceram. Soc. 29 (2009) 2333–2341.

[189] S. Meng, Z. Yue, L. Li, “Effect of ethylene glycol on the orientation and magnetic properties of barium ferrite derived by chemical solution deposition,” J. Magn. Magn. Mater. 354 (2014) 290 - 294.

[190] Z.C. Yuan, A.J. Williams, T.C. Shields, S. Blackburn, C.B. Ponton, J.S. Abell, I.R. Harris, “The production of Sr hexaferrite thick films by screen printing,” J. Magn. Magn. Mater. 247 (2002) 257–269.

[191] Y. Chen, T. Sakai, T. Chen, S.D. Yoon, A.L. Geiler, C. Vittoria, V.G. Harris, “Oriented barium hexaferrite thick films with narrow ferromagnetic resonance linewidth,” Appl. Phys. Lett. 88 (2006) 062516-1 – 062516-3.

[192] Y. Chen, I.C. Smith, A.L. Geiler, C. Vittoria, V. Zagorodnii, Z. Celinski, V.G. Harris, “Microstructural, magnetic and microwave properties of large area $BaFe_{12}O_{19}$ thick films (> 100 μm) deposited on /a-SiO_2/Si and /a-Al_2O_3/Si substrates”, IEEE Trans. Magn. 44(12) (2008) 4571-4577.

[193] Y. Chen, I. Smith, A.L. Geiler, C. Vittoria, V. Zagorodnii, Z. Celinski, V.G. Harris, “Realization of hexagonal barium ferrite thick films on Si substrates using a screen printing technique,” J. Phys. D: Appl. Phys. 41 (2008) 095006-1 – 095006-6.

[194] C.N. Chinnasamy, T. Sakai, S. Sivasubramanian, A.F. Yang, C. Vittoria, V.G. Harris, “Magnetic and microwave properties of basal-plane oriented $BaFe_{11}In_1O_{19}$ ferrite thick films processed by screen printing”, J.Appl. Phys. 103 (2008) 07F710-1 – 07F710-3.

[195] H.M. Rietveld, “Line profiles of neutron powder-diffraction peaks for structure refinement”, Acta Cryst. 22 (1967) 151-152.

[196] H.M. Rietveld, “A profile refinement method for nuclear and magnetic structures”, J.Appl. Cryst. 2 (1969) 65-71.

[197] A.L. Patterson, “The Scherrer formula for x-ray particle size determination”, Phys. Rev. 56 (1939) 978-982.

[198] L.D. Hanke, “Handbook of analytical methods for materials, materials evaluation and engineering”, Inc. Plymouth (2001).

[199] J.J. Bozzola, L.D. Russell, Electron Microscopy, 2nd Edition. Jones & Bartlett Publishers (1998).

[200] T. Gibb, “Principles of Mössbauer Spectroscopy”, Chapman and Hall Ltd, London New York 1976.

[201] K. Haneda, H. Kojima, “Effect of milling on the intrinsic coercivity of barium ferrite powders,” J. Am. Ceram. Soc. 1974 (57)(2) 68-71.

[202] P. Sharma, R.A. Rocha, S.N. Medeiros, A. Paesano Jr, B. Hallouche, “Structural, mössbauer and magnetic studies on Mn-substituted barium hexaferrites prepared by high energy ball milling”, Hyperfine Interact. 175 (1-3) (2007) 77-84.

[203] R. Grossinger, “A critical examination of law of approach to saturation”, Phys. Stat. Sol. (a). 66 (1981) 665-674.

[204] L. Neel, “La loi d'approche en a: H et une nouvelle théorie de la dureté magnétique”, J. Phys. Radium, 9 (1948) 184-192.

[205] P. Sharma, A. Verma , R.K. Sidhu , O.P. Pandey, “Effect of processing parameters on the magnetic properties of strontium ferrite sintered magnets using Taguchi orthogonal array design”, J. Magn. Magn. Mater. 307 (2006) 157-164.

[206] H. Mitsuda, S. Mori, and C. Okazaki, “The crystal structure of barium monoferrite, $BaFe_2O_4$”, Acta Cryst., B27 (1971) 1263–1269.

[207] S. Sorlateap and W. Keawwattana, “Preparation and magnetic properties of La substituted barium ferrites synthesized by the oxide one pot synthesis (OOPS) process”, Adv. Mater. Res. 634 (2013) 2250 - 2253.

[208] C. Sudakar, G.N. Subbanna, T.R.N. Kutty, “Hexaferrite Fe-Co nanocomposite particles and their electrical and magnetic properties at high frequencies”, J. Appl. Phys. 94 (2003) 6030-6033.

[209] T.A. Vanderah, W. WongNg, B.H. Toby, V.M. Browning, R.D. Shull, R.G. Geyer, R.S. Roth, “characterization of ternary compounds in the BaO:Fe_2O_3:TiO_2 System: $Ba_6Fe_{45}Ti_{17}O_{106}$ and $BaFe_{11}Ti_3O_{23}$”, J. Solid State Chem. 143 (1999) 182-197.

[210] Z.W. Li, C.K. Ong, Z. Yang, F.L. Wei, X.Z. Zhou, J.H. Zhao, A.H. Morrish, Site preference and magnetic properties for a perpendicular recording material: $BaFe_{12-x}Zn_{x/2}Zr_{x/2}O_{19}$ nanoparticles, Phys. Rev. B, 62(10) (2000) 6530-6537.

[211] A. Gruskova, J. Lipka, M. Papanova, D. Kevicka, A. Gonzalez, G. Mendoza, I. Toth, J. Slama, Mössbauer Study of Microstructure and Magnetic Properties (Co, Ni)–Zr Substituted Ba Ferrite Particles, Hyperfine Interact. 156/157 (2004) 187-194.